Evaluation of Emission Quantification Technologies

Second Interim Report

March 31st, 2023

Prepared for:

Petroleum Technology Alliance Canada

and Clean Resources Innovation Network

Prepared by:

Professor Kyle J. Daun, PhD., P. Eng., FASME
Professor Christiane Lemieux, PhD
Professor Audrey Béliveau, PhD
Daniel Blackmore
Michael Nagorski
Paule Lapeyre
Augustine Wigle

University of Waterloo

Kevin Fritz

Arolytics, Inc.

Kirk Osadetz

CMC Research Institutes

EXECUTIVE SUMMARY

In September 2021 the University of Waterloo, Arolytics, Inc., and Carbon Management Canada commenced a 3-year study focused on assessing the potential of existing and emerging technologies for measuring methane emissions from upstream oil and gas sources, and developing uncertainties for these estimates. This second interim report summarizes progress up to January 2023, with a focus on the second field campaign, held at Carbon Management Canada's Field Research Station between September 25-October 1 2022.

The second field trial examined the performance of four technologies operated by five providers: two quantitative optical gas imaging (QOGI) systems; a truck-based tunable diode laser-absorption spectroscopy (TDLAS) system; and airborne near infrared (NIR) and long-wavelength infrared (LWIR) hyperspectral (HS) imaging systems. These technologies were used to quantify controlled emissions from: a 1.7 m stack, a 3.4 m stack, a 4.8 m stack, a 13 m unlit flare, from the top of a 2.7 m storage tank, and from the side of a shed. Emission rates ranged from 0.25 kg/hr to 80 kg/hr.

On average, the FLIR QOGI system provided the most accurate estimates under all conditions. The QOGI technologies (FLIR GFx320/QL320 and OPGAL EyeCGas/EyeCSite) had similar performance and with airborne NIR measurements, and were generally more accurate compared to the truck-based TDLAS system. The accuracy of these systems was highest for the stack and unlit flare releases, and considerably lower for releases from the storage tank and shed. This was attributed to the complex aerodynamics surrounding the structure, and, in the case of the QOGI systems, distance, obstructed lines-of-sight, and reflectance from the metallic surfaces.

The performance of the QOGI technologies depended strongly on the distance between the release and the cameras, the ambient wind, the release rate, and the temperature difference between the gas and the background. The FLIR QOGI system outperformed the OPGAL system for releases from the stack and unlit flare, while the OPGAL system was more accurate for the tank and shed releases. It is unclear whether this is due to the different algorithms used by the systems, or the different level of experience of the operators.

The airborne NIR system performed similarly to the QOGI systems, while the LWIR HS systems had a much lower accuracy compared to the other technologies due to operational problems and issues with the emissions quantification algorithm. The NIR HS system performed considerably better in the second field campaign compared to the first field campaign, likely due to the clearer sky condition. Both the LWIR and NIR HS systems require wind speed as an input, and are therefore susceptible to errors in the local wind conditions.

The remainder of the project, which ends in December 2023, will focus on: developing an improved quantification technique for the LWIR HS imaging system; understanding the impact of wind variability on the truck-based TDLAS system; evaluating the potential of incorporating the quantification systems into an emissions management plan through Monte Carlo simulations; and development of a Bayesian framework for estimating the uncertainty of emissions estimates.

1.0 INTRODUCTION

1.1 Purpose and scope

As part of its strategy to address climate change, the Government of Canada has pledged to reduce methane emissions from the oil and gas sector by 40-45% below 2012 levels by 2025 [1, 2], with a further goal of reducing methane emissions by 70% by 2030 [3]. To meet these goals, and to fulfill their obligations under emerging provincial emission regulations, Canada's oil and gas producers need tools that can quantify methane emissions. Regulators need methane quantification tools to assess compliance of industry to these regulations. Climate modelers need the data from these tools to understand how emissions from Canada's oil and gas industry contribute to climate change, information that provincial governments and the Federal government will use to inform policy needed to fulfil Canada's international treaty obligations and to avoid the worst outcomes of climate change.

A diverse suite of candidate methane emission quantification tools is available to Canada's oil and gas industry. There is unlikely to be a "one-size-fits-all" solution: techniques designed to measure localized, persistent fugitive leaks from valves or gaskets may not be suitable for diffuse and intermittent emissions vented from storage tanks, surface casing vents, and CHOPS (cold heavy oil production with sand) wells. Persistent emissions may be identified reliably using periodic surveys, while highly variable or intermittent emissions may require continuous monitoring. Recent advancements in optoelectronic hardware that include mid-wavelength infrared (MWIR) cameras, tunable diode laser absorption spectroscopy (TDLAS) in a range of configurations, and hyperspectral imaging from ground-based, aerial, and orbital platforms have augmented and disrupted the field of traditional approaches based on extractive sampling (e.g., the Bacharach HI FLOW® sampler) although their accuracy, precision, and best practices under various measurement scenarios are still being refined.

Choosing the "right tool for the job" depends, to a large extent, on the uncertainty associated with the methane emission estimates. This is particularly the case in a regulatory context. For example: How certain is it that an operator is complying with emissions? Is it practical to impose a limit on emissions that cannot be measured with reasonable accuracy? What is the most cost-effective technology to deploy for a given measurement scenario? To make these decisions, operators and regulators need to understand the uncertainty with which emissions may be quantified. Climate modelers and policy makers also need to understand the uncertainties attached to reported emission inventories in order to draft effective regulations that safeguard the environment without unduly penalizing oil and gas producers.

With these goals in mind, the Petroleum Technology Alliance Canada (PTAC) and Clean Resources Innovation Network (CRIN) engaged the University of Waterloo (UW), Arolytics, Inc. (Arolytics), and Carbon Management Canada, Inc. (CMC) to undertake a three-year research program entitled "Evaluation of Emission Quantification Technologies". The program is funded by the Alberta Upstream Petroleum Research Fund (AUPRF) through PTAC, the Government of Canada's Strategic Innovation Fund through CRIN, and the Natural Sciences and Engineering Research Council (NSERC) via the Alliance program.

The UW/Arolytics/CMC team brings together the diverse and complementary range of expertise needed to fulfill these objectives. The UW team is led by Professor Kyle Daun from the Department of Mechanical and Mechatronics Engineering, an expert in optical gas imaging, laser-based diagnostics, remote sensing, and uncertainty quantification. Daun is joined by Professors

Christiane Lemieux and Audrey Béliveau from the Department of Statistics and Actuarial Science. Lemieux's research interests focus on Monte Carlo simulations, while Béliveau studies Bayesian statistics and uncertainty quantification. Arolytics's participation is coordinated by Kevin Fritz, an expert in methane emissions quantification and FEMPs; Fritz also has extensive experience in methane emissions field measurements. Finally, CMC's participation is managed by Kirk Osadetz, a geoscientist and expert in methane emissions from Canada's oil and gas industry. Osadetz is CMC's Programs Development Manager and also manages CMC's Field Research Station, where candidate quantification technologies will be evaluated under industry-relevant conditions.

Research activities are organized into four project phases:

Phase 1: Quantification tool review interim summary table

Phase 2: Recommendation of viable quantification tools

Phase 3: Field campaign design and execution

Phase 4: Data analysis and summary

These research activities are guided with input and oversight from PTAC, CRIN, and members of the Industrial Steering Committee (ISC), a subcommittee of PTAC's Air Research Planning Committee (ARPC).

1.2 Phase 1: Quantification tool review interim summary table

Research commenced in September 2021 with Phase 1. The outcome of this phase, which was completed in January 2022, was a comprehensive survey of 23 candidate emission quantification technologies, along with an assessment of their capabilities, their technological readiness level, and their applicability to measuring emissions at the component, facility, and site level. These technologies are summarized in Appendix A.

In general, each technology derives an emission measurement, Q (e.g., kg/hr) by combining a methane concentration measurement with an advection/transport model. In this regard methane emission quantification technologies may be organized according to the nature of the data they collect, which, to a large extent, determines their suitability for various emission scenarios and how uncertainty estimates may be derived. This is shown schematically in Appendix A.

Some technologies are based on point-concentration measurements, like short-path TDLAS, which provide a local concentration of methane, c (e.g., kg/m^3). These measurements are combined with a plume transport model (e.g., the Gaussian plume model [4, 5] or backwards Lagrangian stochastic model [6]) that incorporates local anemometry measurements to obtain an emission rate estimate. Other techniques are based on open-path measurements over long distances, like dual comb frequency spectroscopy [7], in which case the outcome is a column density, σ, integrated along the optical path (ppm·m or kg/m^2); this data may also be combined with a wind speed measurement to obtain an emission rate estimate.

A third category of imaging technology generates a 2D map of column densities; an example MWIR quantitative optical gas imaging (QOGI). In some cases the emission rates are inferred by combining the column density map with a wind measurement, while, for sufficiently high frame rates, a 2D intensity-weighted velocity field may be inferred by feature tracking between successive images. Finally, a fourth class of technology is used to measure emissions from confined flows (e.g., ducts) using gauges. The summary table and diagrams are in Appendix A of this report.

Based on this analysis, a subset of these technologies were identified for further analysis during subsequent project phases: QOGI; truck-based TDLAS; drone-based TDLAS; and aerial near-wavelength infrared (NIR) and long-wavelength infrared (LWIR) hyperspectral imaging.

A brief description of each technique is provided below:

1.2.1 Quantitative Optical Gas Imaging (QOGI) using MWIR broadband cameras

This technique is based on imaging the thermal radiation emitted by a hydrocarbon plume that is hotter than its background (white plume) or the background thermal radiation that is absorbed by a plume colder than its background (black plume). The spectral intensity from the scene enters the camera aperture and is imaged through a broadband filter and onto a focal plane array (FPA). The broadband "cold filter" and FPA are located behind a "cold shield" and maintained at cryogenic temperatures. This is done to enhance the thermoelectric conversion efficiency of the sensor and avoid blackbody radiation from the sensor, camera chassis, and the filter, which would otherwise contaminate the signal and preclude quantitative interpretation of the image.

The cold filter defines the measurement spectrum; a typical choice is 3.2-3.4 μm (FLIR GFx320), which is aligned with a primary vibrational-rotational absorption band corresponding to the C-H stretching mode for hydrocarbons (~3.34 μm, Fig. 1). The brightness of each pixel corresponds to the spectral intensity incident on the pixel, integrated over this wavelength band.

The column density of gas along each line-of-sight, σ (kg/m^2), is then inferred from the pixel intensity by inverting a spectroscopic model. This requires knowledge of: (1) the plume composition (usually taken to be methane); and, in the case of white plumes, (2) the plume and ambient temperatures. In the case of white plumes, the plume temperature is usually taken to be that of the ambient air temperature, following the assumption that gas emerging from a leak will quickly reach thermal equilibrium with the surrounding air. In the case of gases other than methane, a conversion chart may be applied to correct the column densities.

The MWIR measurement spectrum is not the optimal choice based solely on the sensitivity of the pixel intensity to methane column density. Hydrocarbons have a secondary vibrational-rotational band at ~7.6 μm (LWIR) which is far more intense than the 3.34 μm feature because matter at ambient temperatures emits more thermal radiation at wavelengths closer to 10 μm. However, while broadband LWIR cameras may be used to visualize methane, quantitative analysis is precluded by significant emission features from ambient H_2O, as seen in Figure 1.

The 2D column density map is then combined with an advection model to obtain an overall mass flux according to

$$Q = \int_0^{\Theta} \sigma(\theta)\left[\mathbf{u}(\theta)\cdot\mathbf{n}(\theta)\right]d\theta \tag{1}$$

where $\sigma(\theta)$ is the column density at a position θ over the control surface, **u** is the 2D projected velocity, and **n** is the 2D normal vector. The advection model is inferred from the apparent motion of the plume in successive images. Unlike the spectroscopic model, the advection model is a proprietary and largely "black box" aspect of commercial QOGI software. The advection calculation may be affected by artifacts like "pooling" and background motion due to, e.g. moving clouds or vegetation.

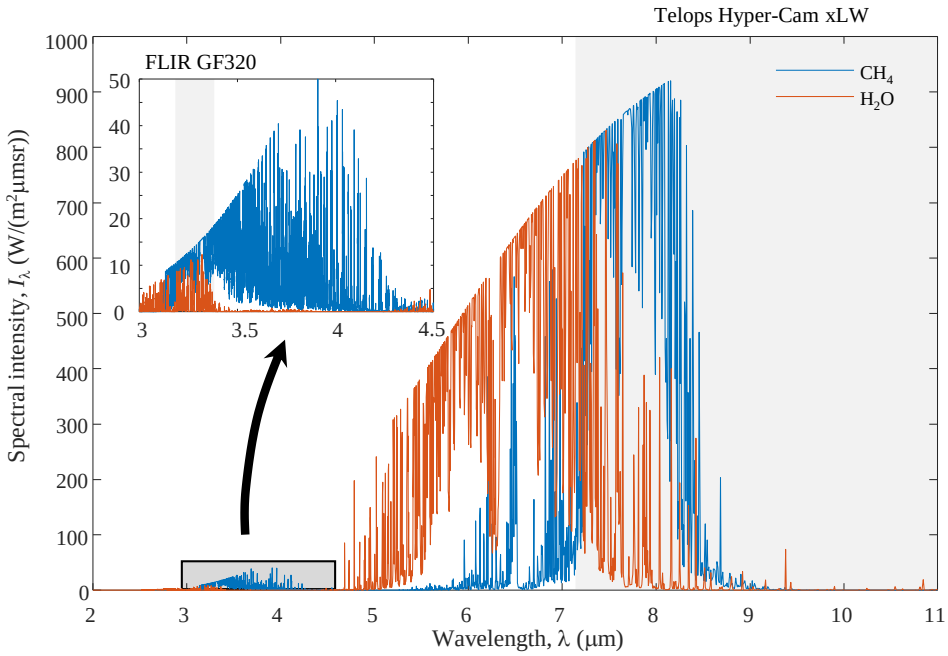

Figure 1: Emission spectrum for methane and water vapor at 300 K (a "white plume"). (CH4: L = 20 cm, χ = 1, H2O: L = 200 cm, χ =0.1.) Broadband QOGI measurements are constrained to the MWIR because of the water lines over the LWIR.

1.2.2 Truck and drone-based TDLAS

Tunable-diode laser absorption spectroscopy is a low-cost and reliable way to measure the concentration of a particular gas, e.g., methane. A distinguishing feature of tunable-diode lasers is that they may be "tuned" across a narrow range of wavelengths by adjusting the supply current; in the case of gas sensing, the wavelengths capture one or more spectral lines corresponding to defined transitions between quantized vibrational-rotational states that act like a "fingerprint" for the species of interest (Figure 2). In the case of a homogeneous gas over a path length L, the gas concentration may be inferred from the Beer-Lambert Law,

$$I_{\eta L} = I_{\eta o} \exp\left(-\kappa_{\eta} L\right) \tag{2}$$

where η is the wavenumber (cm^{-1}, the inverse of wavelength), $I_{\eta 0}$ and $I_{\eta L}$ are the incident and transmitted laser intensity, and κ_{η} is the spectral absorption coefficient, which is proportional to the number density (molecules/m^3) of the species of interest. Inverting Eq. (2) results in a column density, e.g. ppm·m or kg/m^2, which is proportional to the number of molecules along the path length.

This approach is called *direct absorption spectroscopy* (DAS) and is the simplest implementation of TDLAS. In *wavelength modulated spectroscopy* (WMS), the wavelength is tuned rapidly over a single line by harmonically varying the supply current, and the absorption coefficient/column density is then inferred from the AC and DC components of the transmitted signal; WMS provides superior signal-to-noise ratio (and hence a lower detection threshold) compared to DAS and is therefore the most common approach for methane detection.

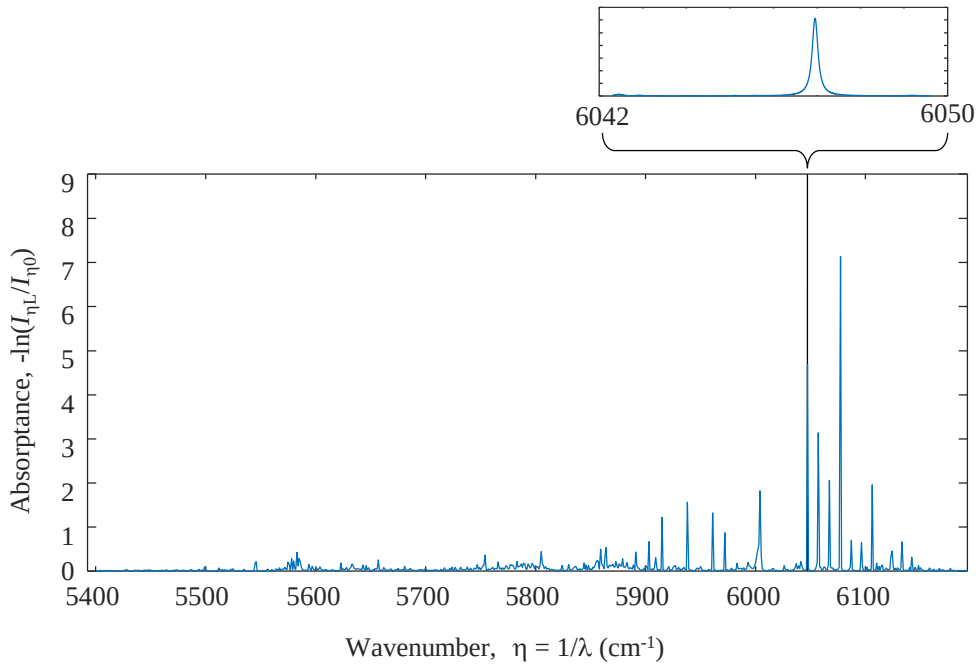

Figure 2:Near-Infrared (NIR) absorption spectrum for CH4 used for TDLAS. Boreal Laser's GasFinder 3 instrument uses wavelength-modulated spectroscopy to infer the concentration based on an absorption line at 1654 nm (6046 cm-1). This part of the spectrum is also the basis for the GHGSat instrument (1630-1655nm) based on absorbed sunlight.

TDLAS may deployed in a wide range of configurations to detect methane. For example, Bridger Photonics' Gas Mapping LiDAR system consists of a TDLAS laser operating in WMS mode mounted on a movable gimbal on an aircraft that overflies the methane plume [8]. The ground-reflected portion of the laser is detected by a sensor onboard the aircraft. The ground reflectivity and column density may be inferred from the backscattered signal. Column densities obtained at different view angles are then tomographically-reconstructed to form a 3D concentration map of the plume. Finally, the concentration profile is combined with an advection model based on modeled (e.g., Meteoblue) or locally measured wind speeds to find mass flow rates. In this configuration, the laser path is defined by the laser, the reflected light, and the receiver. This system's main drawback is that it only works if enough laser light is reflected from the ground. Consequently, the Bridger system does not perform well on wet or snow-covered surfaces, which absorb most incident radiation.

Alternatively, the TDLAS sensor may be configured to measure the gas concentration over an enclosed path. In this approach, the volume is often terminated with a mirror to extend the path length and increase the instrument's sensitivity. In this configuration, the TDLAS instrument provides a time-resolved point concentration measurement (e.g., ppm, kg/m^3). A set of concentration measurements made by moving the sensor through the plume is then combined with an advection model to obtain a mass flow rate.

Two common approaches for traversing the sensor through the plume are: truck-based TDLAS and airborne TDLAS (e.g., drone-mounted.) In the case of the drone mounted TDLAS sensor deployed in the first field campaign, the drone flies a descending helical path around the methane source; the helical path defines a control surface, *A*, which may then be combined with a wind

measurement to determine the total release rate. In one approach, called the *cylindrical flux plane* approach [9], the emission rate is estimated from

$$Q = \int_A c(\mathbf{r})\mathbf{u}(\mathbf{r})\cdot\mathbf{n}(\mathbf{r})\,dA \tag{3}$$

where **r** is the position vector, **u**(**r**) and c(**r**) are the wind velocity vector and concentration at **r**, and **n**(**r**) is the unit normal vector. Alternatively, the emission rate may be found from an inverse Gaussian plume model, which is discussed below. The wind velocity may be found from anemometry (e.g., mounted on the drone) or based on the power required for the drone to maintain its position in a cross-wind. This technique, along with other approaches for inferring methane release rates from drone measurements, are summarized in Ref. [9].

In the case of a truck-mounted TDLAS system, concentration measurements are made at various plume transects. Inferring the emission source that caused these concentrations amounts to solving an ill-posed inverse problem, since an infinite set of candidate sources could account for the observed concentration measurements. Accordingly, it is necessary to impose additional information that connects the source to the concentration measurements; the simplest approach is to assume a Gaussian plume model [4], which assumes that the time-averaged concentration field from a steady release is given by

$$c(\mathbf{r}) = \frac{Q}{2\pi u\,\sigma_x\sigma_y}\left\{\exp\left[-\frac{(z-h)^2}{2\sigma_z^2}\right]+\exp\left[-\frac{(z+h)^2}{2\sigma_z^2}\right]\right\}\exp\left(-\frac{y^2}{2\sigma_z^2}\right) \tag{4}$$

where **r** = (x, y, z) is the position vector, u is the wind speed, h is the effective release height, and σ_y and σ_z are coefficients related to atmospheric conditions. In Eq. (4) the x-axis is aligned in the downwind direction. Equation (4) is rearranged to express Q in terms of the concentration distribution, which are approximated by the finite set of truck measurements, {c}. Other choices for inverting the concentration measurements are available, including the backwards Lagrangian stochastic approach [6].

The main drawback of both the drone-mounted and truck-mounted TDLAS systems is that they assume that the release and wind are time-invariant, while both may change with time. The previous report showed the emission rates derived from the drone-based measurements were particularly susceptible to the errors introduced by this approximation.

1.2.3 Aerial NIR and LWIR hyperspectral imaging

As noted in Sec. 1.2.1., a key limitation of broadband QOGI cameras is that the detected spectral intensity is integrated over the measurement spectrum. Consequently, the camera can only be used to measure pure mixtures (or mixtures of known composition) and, in the case of "white plumes" the plume temperature must be specified. These limitations may be overcome through multuispectral (MS) or hyperspectral (HS) imaging.

MS cameras generate a set of images of the same scene, either using plenoptics/microlenses or dichroic lenses; the split images pass through filters, and are then imaged onto a segmented FPA. Conceptually, this is equivalent to multiple simultaneous broadband cameras viewing the same scene, each containing a distinct cold filter. Typical MS cameras generate on the order of ~10 broadband images; the ONERA SIMAGAZ camera, for example, generates four images [10]. The filters may be chosen to align with vibrational-rotational bands of species-of-interest.

In contrast, HS cameras generate "data cubes" containing hundreds or thousands of images, each at a distinct wavelength. In many cases, this is done through interferometry; this type of HS camera is called an imaging Fourier transform spectrometer (IFTS). In this approach, the image entering the camera aperture is split, e.g., using a beamsplitter. The split images then travel slightly different distances and are then recombined; due to the different distances travelled the resulting images are brighter or darker than the original image due to wave interference effects. Many images are collected for each optical path difference, and the resulting interferogram may be inverse Fourier-transformed to produce the data cube.

Two types of IFTSs are analyzed in the second field trial, each of which works over a distinct measurement spectrum and according to a different measurement principle. GHGSat has adopted their orbital package [11] into an airborne system; it consists of a Fabry-Perot IFTS that operates between 1630-1655 nm, over the NIR spectrum. Thermal emission from the gas and ground is negligible over this wavelength range; instead, the camera images sunlight transmitted through the atmosphere, reflected from the ground, and transmitted back to the camera. The methane column density is inferred from the attenuation of the transmitted light via a multilayer spectroscopic model, and then combined with an advection model to find the emission rate.

There are several schemes that may be used to convert the column density map into an emission rate. In the *integrated mass enhancement* approach the emission rate is approximated by [11, 12]

$$Q = \frac{u_{\text{eff}}}{L_{\text{eff}}} \int_A \sigma(x, y)\, dA \approx \frac{u_{\text{eff}}}{L_{\text{eff}}} \sum_{i=1}^{N} \sigma_i \Delta A_i \tag{5}$$

where u_{eff} is the wind speed and L_{eff} is a characteristic plume length, taken to be the square root of the plume area, found using a Boolean plume mask that distinguishes plume pixels from background pixels. A second approach, called the *cross-sectional method*, infers Q by measuring the mass flux across M column transects at various distances downwind from the source and parallel to the wind:

$$Q \approx \frac{u_{\text{eff}}}{M} \sum_{j=1}^{M} \int \sigma(x_j, y)\, dy \tag{6}$$

where x and y are oriented in the downwind and crosswind directions, respectively.

Telops and LiDAR Systems, Incorporated (LSI) also use a downwards looking IFTS (Telops Hyper-Cam xLW Airborne Mini), but one that operates at much longer wavelengths (7.4-12.5 μm). Instead of relying on transmitted sunlight, the camera exploits the thermal contrast between the gas and the background to infer column densities. As already noted, thermal emission over the LWIR spectrum is significantly greater compared to the MWIR spectrum used by broadband cameras; the spectral resolution of the IFTS makes it possible to disentangle contributions of methane and H_2O, which cannot be done using broadband cameras.

In contrast to the Bridger airborne GFL system, which uses a laser to interrogate the plume, the GHGSat and Telops systems are entirely passive; they can also image much larger areas compared to the Bridger system, but generally have lower detection thresholds. The GHGSat system is sensitive to ground reflectance and cloud cover, which affects the incident and reflected sunlight. The sensitivity of the Telops system depends on the thermal contrast between the plume and the background surface.

A key drawback of HS cameras in general is the time needed to generate each interferogram, typically on the order of minutes. Also, in the case of gas flows, temporal changes in intensity fluctuation caused by the moving gas become convolved with intensity changes caused by wave interference (interferometry), leading to scene change artifacts [13].

1.3 Phase 2: Analysis of candidate emissions quantification technologies

This project phase has two components: Phase 2a, led by Arolytics; and Phase 2b, led by UW.

1.3.1 Phase 2a: Recommendation of the most viable quantification tools

Arolytics personnel used Arolytics' proprietary AroFEMP simulation code to predict the performance of three technologies identified in Phase 1 (two of which were evaluated during the field campaign) as if they were incorporated into an alternative FEMP (alt-FEMP) program. This procedure considered various scenarios in which operators would use candidate technologies to detect and quantify methane emissions, and then action repairs over a calendar year based on the outcome of these surveys. The overall benefit of a given technology, in terms of the reduction in emissions (e.g., kg/year), were evaluated through a Monte Carlo simulation. Emission scenarios were sampled randomly from probability densities that represent operational conditions, and emissions were detected and quantified with probabilities derived from manufacturer-specified characteristics of the quantification technologies or previous field trials identified in Phase 1. Repeating this procedure multiple times amounted to an integration over the probability densities, with the outcome of the expected reduction in emissions.

In preparation for this project phase, Augustine Wigle, a UW PhD student under the supervision of Lemieux and Béliveau, spent a four-month internship with Arolytics to help them verify their code and improve its performance (Wigle was sponsored by a Mitacs Business Strategy Internship and paid outside of the project budget). The next step in Phase 2a was to derive probabilities for representative emissions probability profiles. This was done using emissions data from the Fugitive Emission Management Program Effectiveness Assessment Study (FEMP-EA), a collection of fully-randomized, QOGI-based bottom-up emission measurements from approximately 200 oil and gas producing sites in the Red Deer region [14].

The four technologies that were modelled are: airborne light detecting and ranging (LiDAR) (Bridger Photonics), airborne NIR hyperspectral imaging (GHGSat), truck mounted TDLAS (Boreal Laser), and QOGI using the FLIR GF320/QL320 system. The QOGI system was modelled as conducting the default FEMP required by the Alberta Energy Regulator's (AER) Directive 060 Section 8.10 [15]. If the total fugitive emissions of an alt-FEMP were equal to or less than the fugitive emissions produced by the default FEMP, then the alt-FEMP was deemed equivalent and the alternative technology feasible for deployment in an alt-FEMP. The results of the modelling are presented in Section 4.0.

1.3.2 Phase 2b: Laboratory trials and development of digital twin systems

In parallel, the UW team is conducting laboratory-scale analysis and numerical simulations to further investigate the capabilities of the most promising technologies identified in Phase 1. Specifically, Phase 2b activities have focused on developing and quantifying the performance of spectroscopic and optical flow models for QOGI, and the derivation of an inverse Gaussian plume model (IGM) for interpreting truck based TDLAS measurements.

Research into QOGI technology was led by Michael Nagorski, a MASc candidate under Daun. Laboratory measurements were carried out using a FLIR GFx320 camera and QL320 tablet

system, as well as a four-channel Telops multispectral (MS) channel provided by CMC. Nagorski developed an "in-house" version of the QL320 tablet based in Matlab® and validated its performance through simulated measurements generated using a CFD Large Eddy Simulation of a methane plume, as well as plumes generated with a heated vent apparatus. The simulated measurements were used to validate the spectroscopic model used to infer the species column densities, and the optical flow algorithm used to obtain the velocity field [17, 18].

In the heated vent experiments, infrared images captured using the GFx320 camera were interpreted using the QL320 tablet and UW's in-house code. In most cases, UW's code matched or exceeded the performance of the QL320 tablet with regards to the overall mass flow rate when using a bulk velocity estimated from the images, but the framerate of the GFx320 was too low for the in-house optical flow algorithm to provide robust velocity fields. A subsequent meeting with Providence Photonics, the originator of the QL320 system, held in late 2022 provided further insights into the proprietary aspects of this technology [19]. While the exact numerical methodology was not disclosed, it is believed that the algorithm is built upon one of the optical flow algorithms offered by the open-source computer vision library OpenCV [20], which are fundamentally similar to those tested in-house.

These lab-scale experiments highlighted measurement conditions that would be problematic for conducting QOGI emission estimates, especially emissive "white" plumes of uncertain temperatures. As noted in Sec. 1.2.1, since the GFx320 camera has a single measurement spectrum, simultaneously inferring the methane column density (ppm·m) and temperature amounts to solving one equation with two unknowns. Consequently, it is necessary to assume a plume temperature when calculating emission rates in these scenarios; in cases where the plume temperature is uncertain, the corresponding emission rates may be highly inaccurate.

While the Telops camera could visualize gas plumes at a high frame rate, quantitative emission estimates were not possible due to thermal emission from the uncooled filters. Further details of both the GFx320/QL320 and Telops test results were provided in the previous interim report [21].

Inverse Gaussian plume modelling (IGM) research is led by MASc student Daniel Blackmore with assistance from Dr. Paule Lapeyre, a postdoctoral fellow, both under Daun's supervision. The IGM (Figure 3 [4, 5];) was validated using concentrations from a CFD-Large Eddy Simulation of a methane plume, following Caulton, et al. [4]; these simulations were also used to evaluate how various factors (e.g., plume height, measurement location, wind speed) affect quantification uncertainty using this technique.

Both the QOGI and IGM measurement models have been deployed to interpret field measurements carried out in Phase 3. The IGM is also the basis for initial Bayesian uncertainty quantification analysis carried out under Phase 4.

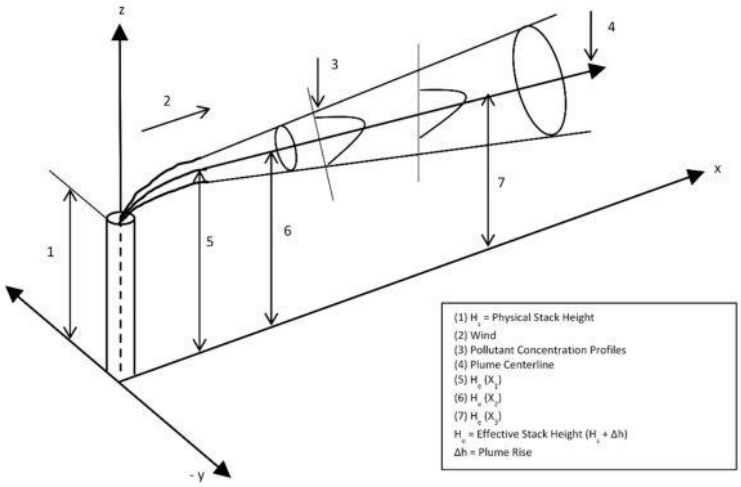

Figure 3: Schematic of an inverse Gaussian plume model (IGM) calculation [5].

1.4 Phase 3: Field campaign design and execution

The project plan called for two field campaigns, both of which to be executed at the CMC Field Research Station (FRS) near Brooks, Alberta. The rationale for having two field campaigns was: (1) technologies could be evaluated at different times of year, in order to isolate the influence of environmental factors (e.g., ambient temperature, snow cover, etc.); (2) some key technologies that may not be available for the first field campaign may become available for the second campaign; and (3) lessons learned from the first campaign may be incorporated into the planning of the second campaign.

Ultimately, due to scheduling limitations, the field campaigns were conducted under similar environmental conditions, but did allow for some providers who were unavailable in the first trial to participate in the second campaign. Moreover, some technologies (QOGI, airborne NIR HS imaging) were evaluated at both campaigns, which provided important insights into the consistency of these technologies.

1.4.1 Summary of first field campaign

The first campaign was conducted during April 20th-26th, 2022. Participants included AGAT Technologies (GF320/QL320), GHGSat (airborne NIR HS imaging), Boreal Laser (truck-mounted TDLAS), and the Southern Alberta Institute of Technology (SAIT, GF320/QL320 and drone-mounted TDLAS). Each operator participated on a subset of the field trial days, with some overlap. Telops/LSI had intended to contribute their airborne LWIR HS system, but were unable to participate due to aircraft issues.

Releases were conducted from a range of industrially relevant scenarios, including a 1.42 m tall stack, a 3.18 m tall stack, a 13 m tall unlit flare, and from the top of a 2.79 m tall storage tank. The release heights were chosen to explore how plume interactions with the ground as well as wind speed, which increases with release height, impacted emission quantification. The tank release was used to assess how aerodynamic/structure interactions and reflection from a metallic surface (which are more pronounced in the MWIR spectrum compared to the visible spectrum) may affect QOGI estimates made with the GF320/QL320 system. The different release heights also provided some indication as to how the distance between the release and the camera aperture may affect QOGI estimates.

Releases were made from a natural gas trailer; an assay showed the natural gas consisted of 94.2% methane, 3.4% ethane, 1.1% propane, and 1.3% minor components, predominantly N_2 and O_2 in roughly relative atmospheric abundances. The gas was released through a regulator valve and flowed through a heat exchanger/conditioner that heated the cold gas (due to the Joule-Thomson effect) to ambient temperature. The conditioned gas then passed through a mass flow controller and discharged to the atmosphere in a manner that depended on the release scenario.

Release rates ranged from 9.25 kg/hr (5.81 standard litres per minute, SLPM) to 50 kg/hr (1164 SLPM); this range was chosen to represent key industrial scenarios, as well as the United States Environmental Protection Agency's (US EPA's) 10 kg/hr detection threshold for candidate methane detection technologies under the Clean Air Act [22]. Most releases lasted 10-15 minutes (with longer releases for airborne measurements), and there was an interval of at least 5 minutes per release to ensure that residual methane from the previous release was cleared by the wind prior to commencing a new release. Emission rates were chosen quasi-randomly to disguise the emission rates from the providers and to avoid unintentional correlations between release rate and wind speed. The combination of release rate and release scenario resulted in a total of 383 measurement events, with a number of "null releases" and duplications.

Technology providers were responsible for conducting measurements, analyzing data, and providing their best estimates for each release, with two exceptions: (1) the SAIT GFx320/QL320 system was operated by Nagorski (UW); (2) Boreal Laser carried out their own backwards Lagrangian stochastic (BLS) analysis of their TDLAS data, but they also provided their raw data to Blackmore (UW), who conducted an independent IGM analysis on the same data. In all cases the provider/analyst was not aware of the true release rate until after they computed their estimates. Providers/analysts were requested to provide their estimates within 3 weeks of the field measurement. This constraint was satisfied except in the case of Boreal Laser, since key personnel were unavailable immediately following the field campaign.

Details of the first field campaign are provided in the previous interim report [21], and a summary of the performance to the technologies is included in Appendix B. Key findings include:

Truck-mounted TDLAS (Boreal): This technique provided the most accurate and unbiased estimated and appeared least-susceptible to environmental factors. Both the IGM and BLS models provided estimates of similar quality. Estimates of stack emissions were more accurate than emissions from the top of the storage tank.

Drone-mounted TDLAS (SAIT): Only 15 measurements were attempted by the SAIT team, and a majority of these were considered "missed detections" due instrument failure or unfavorable measurement conditions (e.g., unsteady wind.) The release estimates obtained from the drone were the least accurate of those from the first field trial. The SAIT team remarked that the short duration of the measurement events differed from the procedures they normally follow, which involved making a larger number of measurements per release.

QOGI (AGAT, UW): QOGI estimates of stack releases were more accurate than those made from on top of the storage tank; this was attributed mainly to the increased measurement distance in the latter scenario. In general, QOGI estimate accuracy dropped for higher wind speeds and flow rates, likely due to limitations in the camera framerate and the advection algorithm. While no head-to-head comparison was possible, emissions estimated by the UW operator using the GFx320/QL320 system from SAIT were more accurate than those found by AGAT, despite the considerable

experience of the AGAT operator. We speculated that this is because the SAIT QL320 tablet was newer than the one used by AGAT, and may incorporate improvements to the advection model.

Airborne NIR HS imaging (GHGSat): Measurements were conducted under conditions that the operator reported as suboptimal due to partial cloud cover. Overall, the provider mostly underestimated the true emission rates. There was no apparent correlation between wind speed and estimate accuracy; rather, cloud cover appeared to be the main factor that limited estimate accuracy. The provider reported that cloud cover can affect the estimate by attenuating the incident sunlight used to measure the methane, and by casting a "mottled" pattern on the ground that confounds plume identification. In contrast to the other providers, GHGSat provided uncertainty estimates for their emission rates, although these underestimated the true error in the estimates.

2.0 EXECUTION OF THE SECOND FIELD CAMPAIGN

This report focuses on the second field campaign of the project, carried out between September 25th and October 1st 2022.

2.1 Location and equipment

Measurements took place at the CMC FRS near Brooks AB, the site of the first field campaign in April 2022 (Figure 4). This equipment includes various stacks for releasing methane, storage tanks, valves, a rented gas trailer, meteorological sensors, and safety equipment. Operations are coordinated from an ATCO trailer, while most releases (except for storage tanks and shed) took place in an open field approximately 100 m north of the trailer. The location of the assets used for the field campaign is shown in Figure 5.

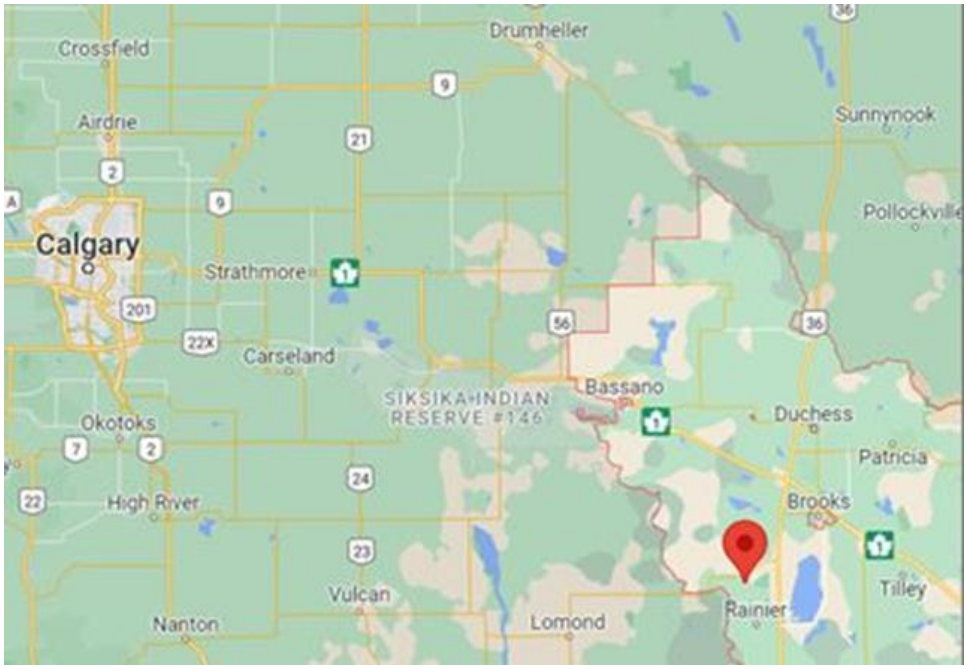

Figure 4: Field trial location

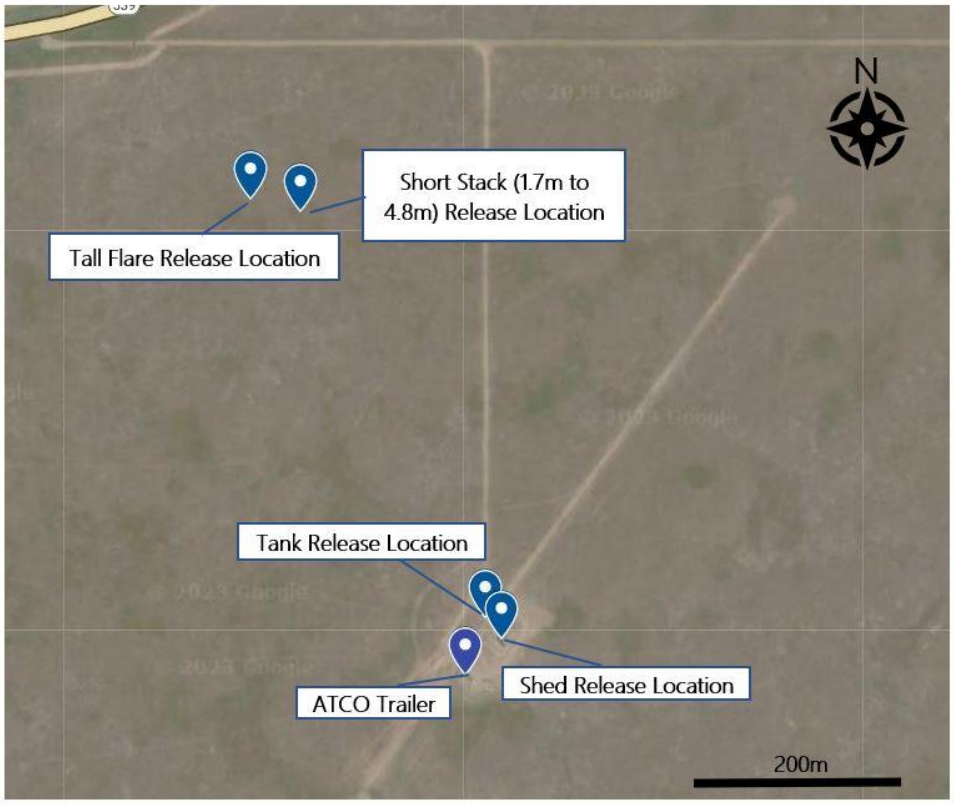

Figure 5: Trailer and release locations

Meteorological sensors include a Davis WeatherLink Pro + weather station affixed to the ATCO trailer that contains a cup-and-ball anemometer for wind speed; it also provides temperature, humidity, and solar irradiation data. Other meteorological data comes from a portable 81000-L, RM Young UVW 3D ultrasonic anemometer with a CR3000 measurement and control datalogger set up next to the release locations, and a second 3D ultrasonic anemometer from the University of Colorado located next to the FRS ATCO trailer. A third set of wind data comes from an ultrasonic anemometer operated by Boreal laser during their measurements. Additional weather information is obtained from Meteoblue [23].

Emissions were released following a procedure identical to the one used in the first field campaign. Natural gas (94.2% methane by volume) was released from pressurized tanks via a regulator valve. The temperature of the expanding gas dropped due to the Joule-Thomson effect, which was returned to that of the ambient air by following the gas through a heat exchanger. The natural gas then flowed through an Alicat Model MCR-2000SLPM -D-PAR mass flow controller (calibrated on July 31 2022), before finally being vented out of the stack, tank, or shed, depending on the release type being investigated. The setup is shown in Figure 6. The flow rate was inspected and logged digitally during the releases, revealing very little variation in the flow rate. An example flow rate log is shown in Appendix C.

Figure 6: Controlled release setup

2.2 Emission quantification technologies and providers

The second field campaign focused on four technologies operated by five providers: QOGI (two providers), truck-based TDLAS, airborne LWIR HS imaging, and airborne NIR HS imaging. Photos of these systems are shown in Figure 7.

Figure 7: Participating technologies in September 2022 field trials. From left to right, top to bottom: Airborne NIR HS Imaging; FLIR GF320 QOGI; OpGal QOGI; Airborne LWIR HS Imaging; Truck-based TDLAS

2.2.1 Quantitative Optical Gas Imaging (QOGI)

QOGI measurements were conducted by two participants, each deploying a different system: personnel from Montrose Environmental Ltd (Montrose) used an OPGAL EyeCGas camera and EyeCSite tablet, while UW personnel (Nagorski) operated the FLIR GFx320 camera and QL320 tablet. Both systems employ a mid-wavelength infrared (MWIR) camera with a cryogenically cooled detector and bandpass filter that images the wavelengths of hydrocarbon emission and

absorption. The technical specifications of these cameras are very similar, and the detection spectra (shown in Figure 1) are identical. The most relevant technical specifications of each camera are summarized in Table 1.

Table 1: Summary of OGI camera technical specifications

	FLIR GFx320 [24]	**OPGAL EyeCGas** [25]
Spectral Range	3.2 to 3.4 µm (filter)	3.0 to 4.4 µm (detector) 3.2 to 3.4 µm (filter)
Spatial Resolution	320x240	320x240
Optics	f/1.5; 24° with 23 mm lens	f/1.1; 18° with 30 mm lens
Frame Rate	15 Hz	Unknown
Sensitivity/NETD	<10 mK @ 30°C	<10 mK @ 25°C

The tablets that pair with each of these OGI cameras contain proprietary QOGI algorithms that are able to estimate the column densities and apparent velocities on a pixel-by-pixel level, then output an overall flow rate estimate. The software version of the FLIR QL320 was 1.4.1 and the software version of the OPGAL EyeCSite was 1.0.24.

2.2.2 Aerial providers

Releases were also quantified through two downward-looking airborne HS imaging systems. GHGSat deployed their NIR HS imaging system from a Piper Navajo operating at approximately 200 m AGL and 240 km/hr. LSI Inc and Telops deployed their Hyper-Cam xLW airborne mini system from a helicopter operating at approximately 170 m and 50 km/hr. Both GHGSat and Telops constructed their own 2D column density maps from hyperspectral data cubes and used this data to derive their own emission estimates. GHGSat also provided uncertainty estimates.

2.2.3 Truck-borne TDLAS

Boreal Laser operated their Gasfinder3-VB system, which features a NIR tunable diode laser (see Sec. 1.2.2) shone across a perforated measurement chamber approximately 1.3 m in length. The laser is modulated across the 1654 nm methane absorption line, and concentration is inferred through the Beer-Lambert law, Eq. (2), via wavelength-modulated spectroscopy. Instantaneous concentration measurements made as the truck traverses through the plume are combined with GPS data from an onboard sensor, as well as wind speed and wind direction from a nearby ground-based ultrasonic anemometer. This data was analyzed by the technology provider using Wind-Trax [6], a backwards Lagrangian stochastic (BLS) dispersion code. Raw data (concentration, wind, and GPS coordinates) was also provided to UW to conduct independent inverse Gaussian modelling (IGM) analysis on the same dataset, which will be performed at a later date. A summary of the technology's relevant technical specifications can be seen in Table 2, while a typical plume transect for the truck is shown in Figure 8.

Table 2: Relevant technical specifications for the Gasfinder-3 system [26]

Specification Name	Specification Value/Description
Minimum Detection Limit (MDL)	0.66 ppm
Sensitivity	0.16 ppm
Spectral Range	Modulation about 1654 nm absorption line
Sampling rate	1 sample per second

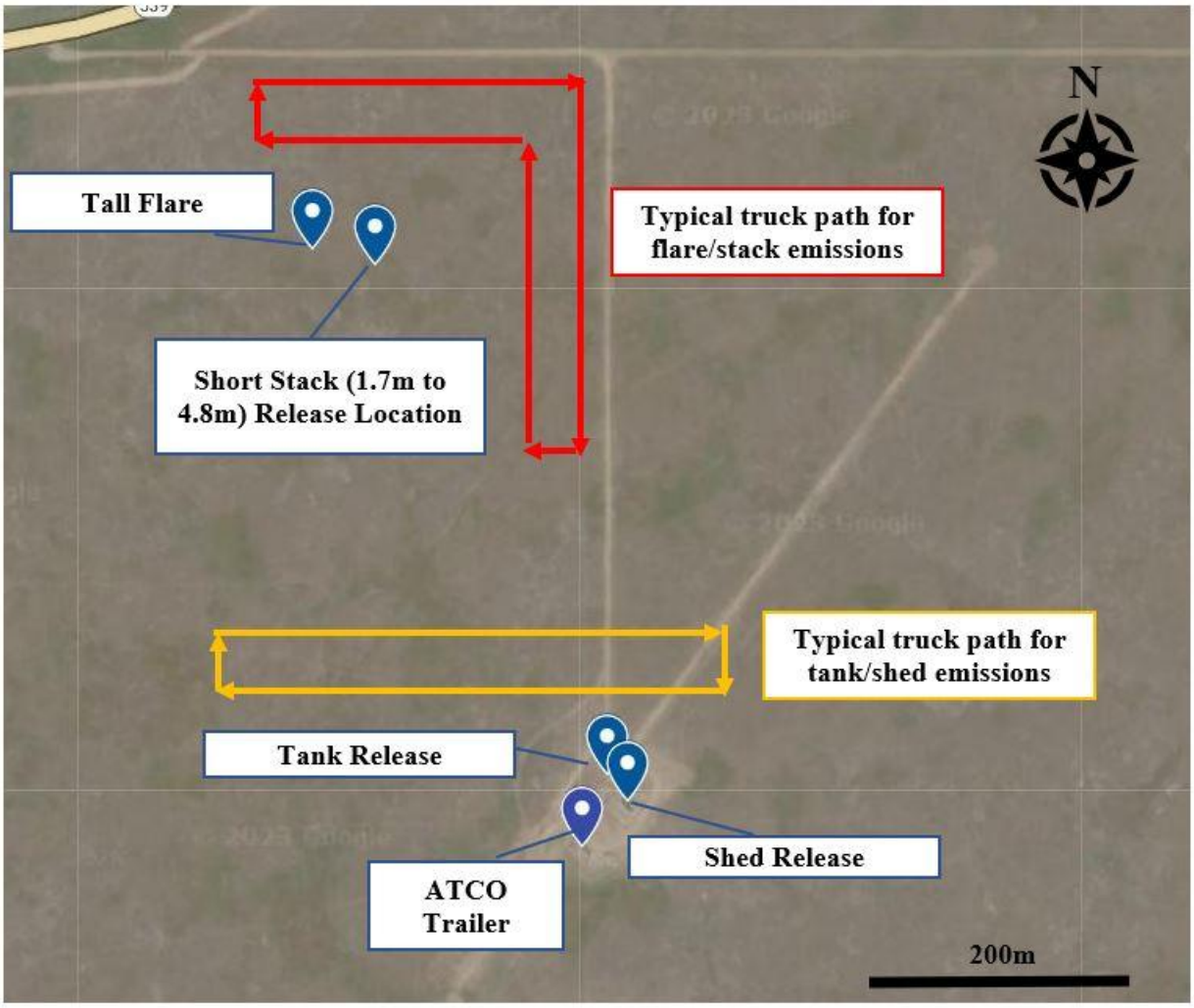

Figure 8: Typical truck paths for truck-based TDLAS technology

2.3 Meteorological conditions

As mentioned previously, there were four independent sources of meteorological data (wind speed, wind direction, temperature) for this field campaign. Figure 9 and Figure 10 summarize daily average windspeed and temperatures, which are generally consistent between the sources.

Generally, the Meteoblue data stands out from the other sources, which is to be expected since it is considered the least accurate and is developed from a meteorological model.

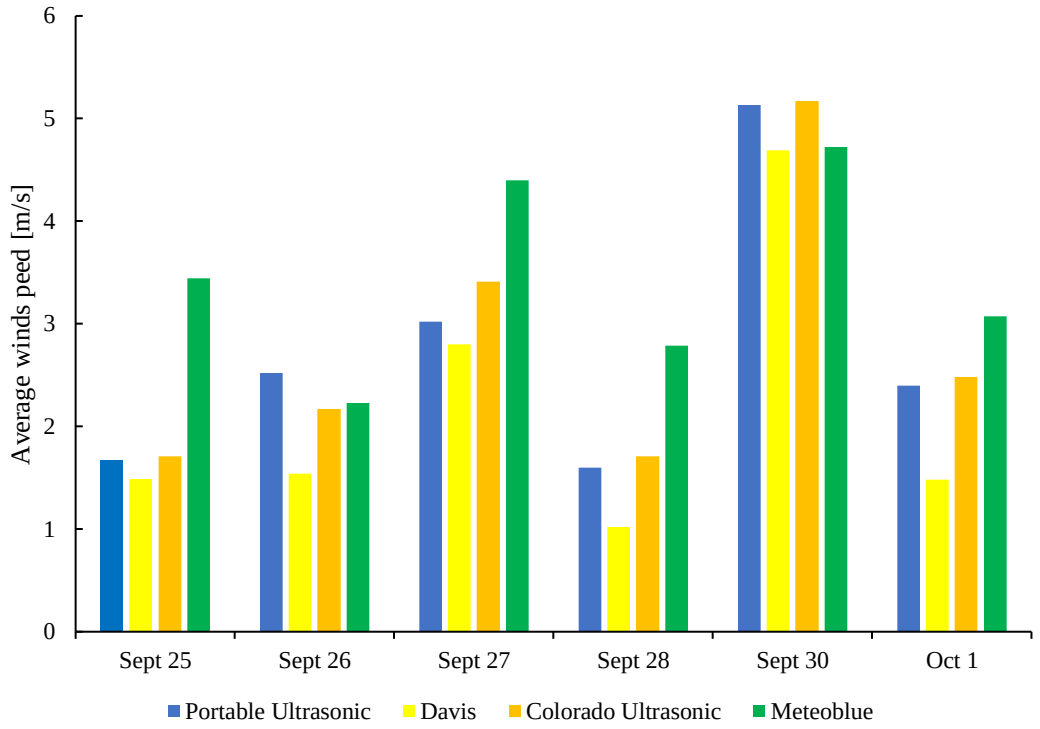

Figure 9: Daily average windspeeds provided by each source of meteorological data.

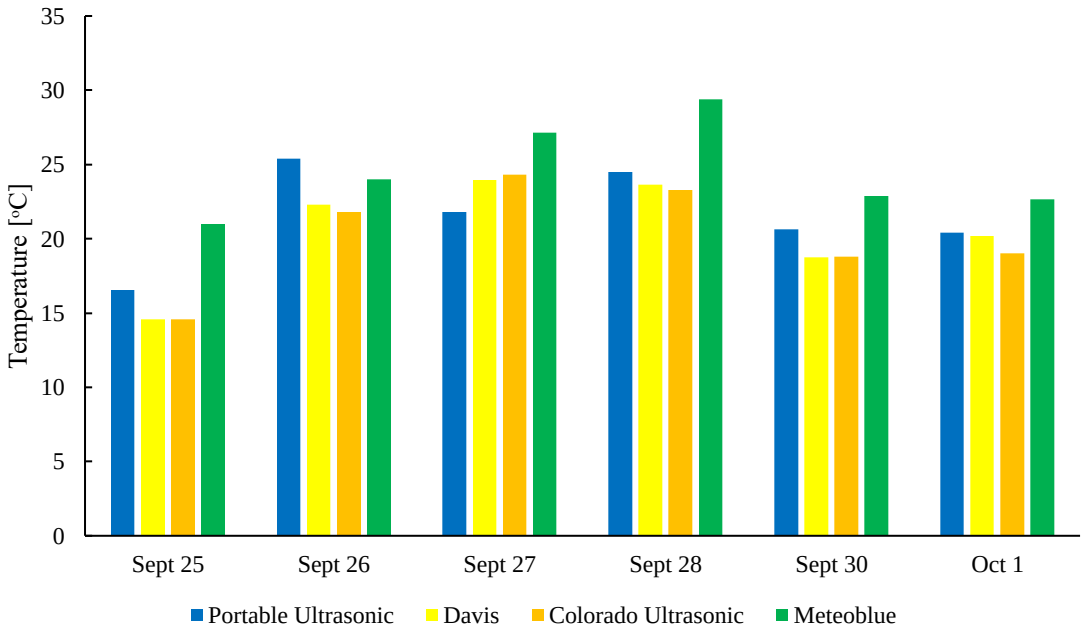

Figure 10: Daily average temperatures provided by each source of meteorological data.

While average wind speed and temperature provides a convenient summary of overall conditions on a given day, the performance of the emission technologies depends on the instantaneous meteorological conditions as summarized in Table 3. Accordingly, time-resolved measurements are crucial when interpreting the performance of the technologies and when developing uncertainty estimates (see Sec. 4). Figure 11 and Figure 12 show near instantaneous wind speed and wind direction over a one-hour window on September 27th, which is representative of data collected throughout the field campaign. Data from the various instruments are generally in agreement, albeit with a little more offset between the sources being present in the wind direction data. Discrepancies may be attributed to the fact that the portable ultrasonic anemometer was located 10-20 m away from the release location, while the Davis weather station and fixed ultrasonic anemometer was located near the ATCO trailer, which was located about 250 m away from the stack release locations as shown in Figure 5.

Table 3: Summary of meteorological effects on technology performance

Technology	**Sensitivity to meteorological conditions**
QOGI	• Wind: QOGI advection model, wake aerodynamics, column density for spectroscopic model • Air and background temperature (thermal contrast)
Truck-based TDLAS	• Wind: consistency of wind during measurement (applicability of Gaussian plume assumption) • Wind: plume dispersion/concentration
Airborne NIR HS imaging	• Wind: plume dispersion/column density • Cloud cover (incident sunlight and plume detection)
Airborne LWIR HS imaging	• Wind: plume dispersion/column density • Ground and air temperature (thermal contrast)

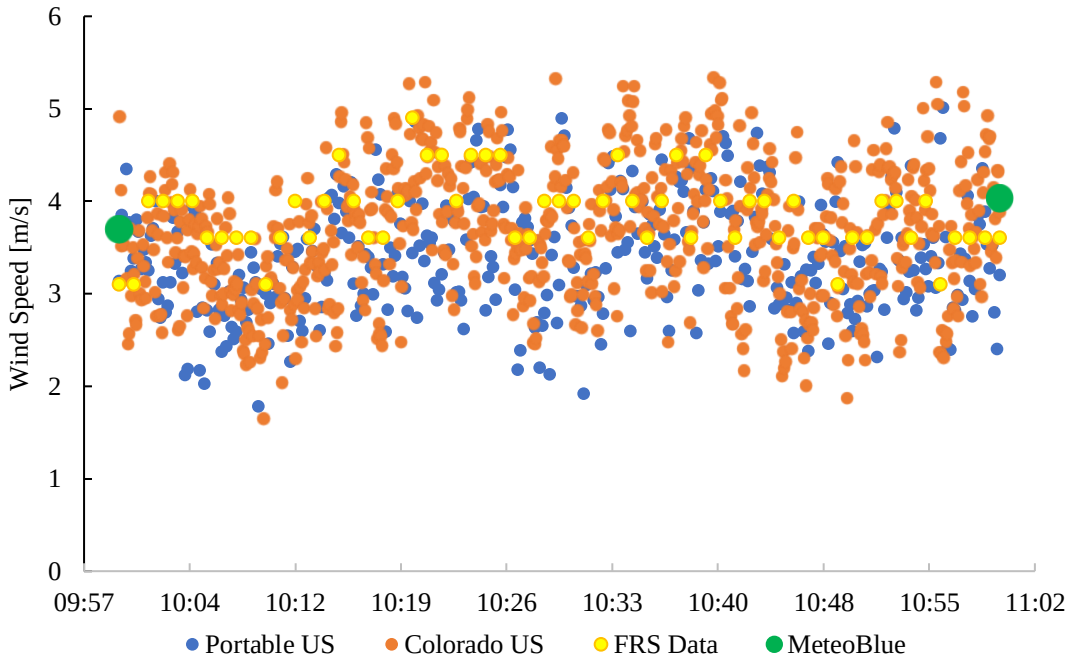

Figure 11: Instantaneous windspeed measurements on September 27th. (All times MST.)

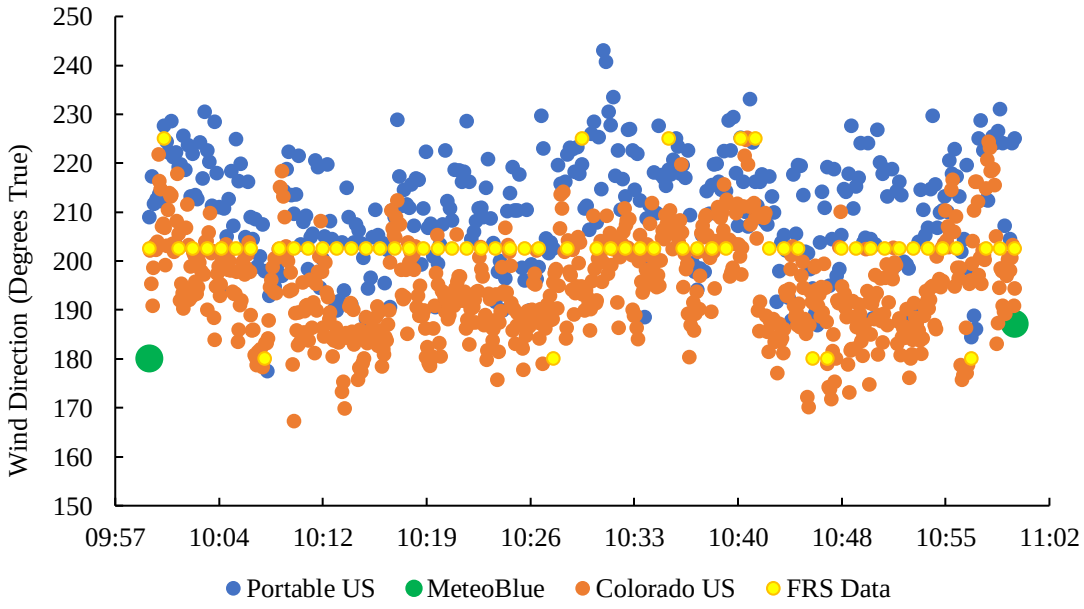

Figure 12: Instantaneous wind direction measurements on September 27th. (All times MST.)

Finally, Figures 5 and 6 compare the wind speed and wind direction data from the field campaign was compared to historical data for the region from 2017-2021. Windspeeds during the field campaign are typical of historical conditions. In contrast, the temperatures were clearly significantly hotter than historical averages, with the average temperature throughout the week being approximately 7°C hotter than the average for the previous 5 years.

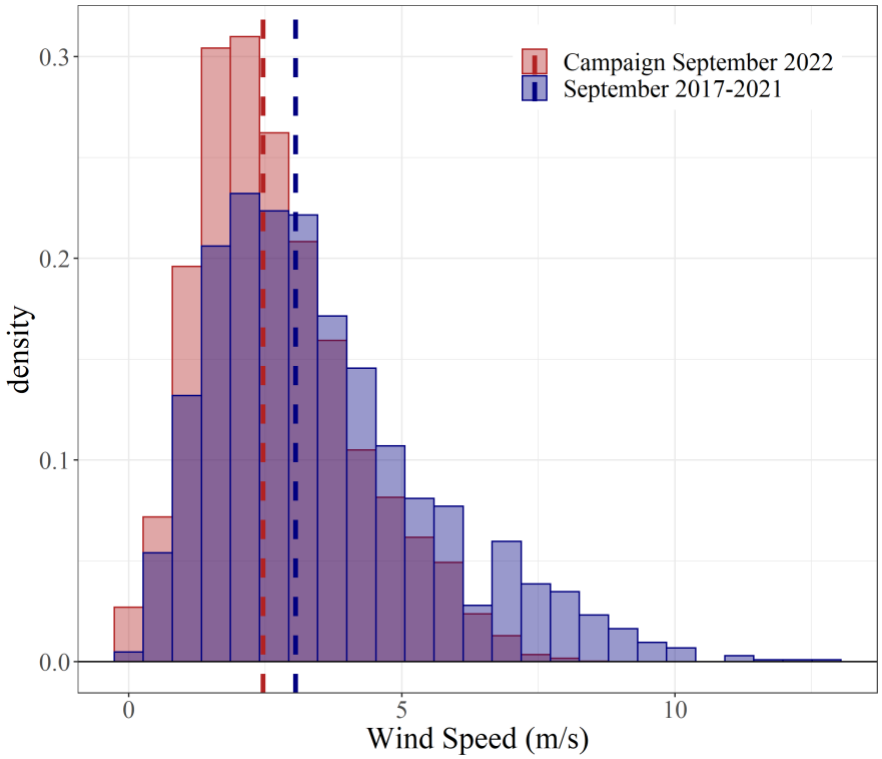

Figure 13: Comparison of windspeed from the field campaign to historical data.

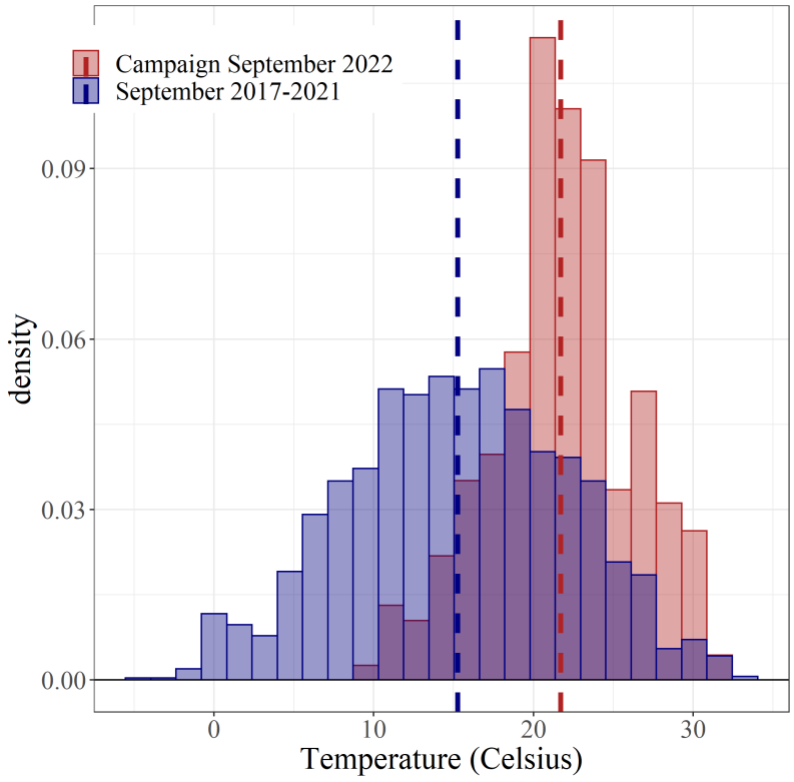

Figure 14: Comparison of temperature from the field campaign to historical data

The background methane concentration was monitored throughout the tests using a Picarro cavity ring-down spectrometer (CRDS) located at the ATCO trailer. This is important in view of the number of potential methane sources in the vicinity, including a large feedlot located 40 km northwest of the FRS as well as several wells. The average background methane concentration was between 2 and 2.5 ppm, which is a typical of the global average. On certain days, there were small spikes in the methane concentration, less than 1 ppm in magnitude. These spikes could have resulted from upstream oil and gas operations, or perhaps from the field tests themselves. Figure 15 shows the most stable day of background measurement (September 27th), while Figure 16 shows the most unstable day (September 28th) of background measurement and the most significant concentration spike.

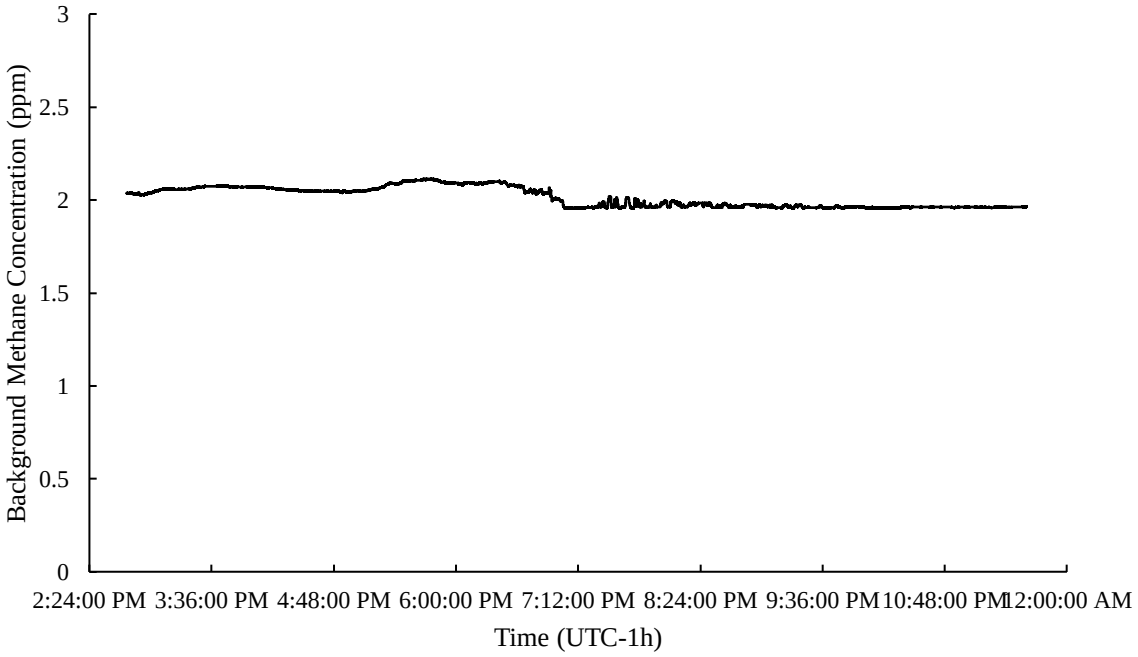

Figure 15: Background methane concentration for September 27th

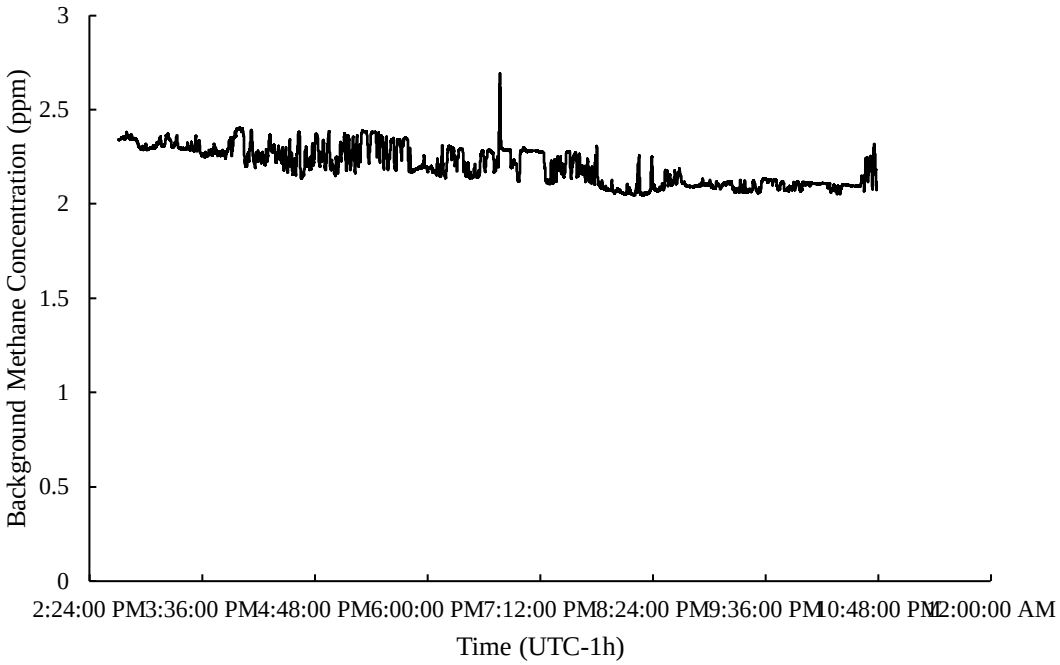

Figure 16: Background methane concentration for September 28th

For the purposes of the analysis presented in this report, anemometry data was taken from the portable ultrasonic 3D anemometer, unless otherwise noted. This was because this anemometer was closest to the release location and had the highest temporal resolution with respect to the measurements of the available sources. Data from the 3D anemometer was lost on two occasions: September 26th between 9:31 AM and 11:21 AM; and September 27th between 3:20 PM and 4:06 PM. For these time frames, meteorological data was taken from the Davis weather station at the FRS, as this was the next closest source of meteorological data, and wind data from these two sources were generally consistent.

For the purposes of following figures of this report, wind was categorized into low, medium, and high categories. The categories were chosen by arranging the observed wind speeds during the field trial from lowest to highest and then dividing the data into thirds. The low category was the bottom third, which was made up of speeds below 1.89 m/s. The medium category was the middle third which ranged from speeds of 1.89 m/s to 3.13 m/s. The high category was composed of speeds greater than 3.13 m/s.

2.4 Design of the field campaign

The timeline of the technology availability throughout the week of September 25th to October 1st is shown in Table 4. The original testing plan had aerial LWIR HS imaging scheduled on September 29th, but this had to be postponed to September 30th due to issues installing the instrumentation within the aircraft.

Table 4: Technology availability timeline.

Date	Technology (providers)	Release scenarios
Sep 25	• Airborne NIR HS imaging (GHGSat)	13 m unlit flare; 1.7 m stack
Sep 26	• QOGI (UW, Montrose) • Truck-based TDLAS (Boreal)	13 m unlit flare; 1.7 m stack; 4.8 m stack
Sep 27	• QOGI (UW, Montrose) • Truck-based TDLAS (Boreal)	Storage tank; 1.7 m stack
Sep 28	• QOGI (UW, Montrose) • Truck-based TDLAS (Boreal)	1.7 m stack; 3.4 m stack; 4.8 m stack; Shed
Sep 29	• No measurements	No scenarios
Sep 30	• QOGI (UW) • Airborne LWIR HS imaging (Telops/LSI)	13 m unlit flare; 1.7 m stack
Oct 1	• Airborne LWIR HS imaging (Telops/LSI)	13 m unlit flare; 1.7 m stack; Tank

The field tests were designed to explore the interaction between each technology and potential factors:

Release rates: Releases ranged from 0.25 kg/hr to 80 kg/hr. The minimum release rates for each technology were chosen based on the corresponding minimum detection threshold (MDL). For QOGI, truck-based TDLAS, and airborne LWIR HS imaging, a minimum non-zero release of 0.25 kg/hr was chosen, while the minimum non-zero release of the airborne NIR HS system was 5 kg/hr based on conversations with the provider.

Release rates were quasi-randomized to avoid any consistent trend in release rate; this was done to both disguise the release rate from the provider and also avoid any unintentional covariance between release rate and wind speed. An example release schedule is shown in Figure 17. Full information on the releases can be found in Appendix D.

Release scenarios: Four different release types were used to investigate how different release configurations affect quantification accuracy. These included: a short, modular vent stack that could be adjusted to a release height of 1.7 m, 3.4 m, and 4.8 m above ground; a 13 m tall unlit flare stack; a 2.79 m tall storage tank; and a storage shed. The storage shed release was done through a perforation in the wall on the leeward side of the shed, approximately 1.5 m above the ground.

The majority of releases were performed using the short stack and the unlit flare stack. Release height is known to affect the quantification accuracy of airborne NIR HS imaging due to the manner in which the plume interacts with the ground. It may also impact the performance of the truck-mounted TDLAS system via Eq. (4) (e.g., if the measurement path is beneath the plume.) Release height also impacts ambient wind, which generally increases with height above ground. Finally, releases from the storage tank and shed were conducted to examine how aerodynamic interactions with the structure (e.g., turbulent wakes) and reflection from the metallic surfaces may impact the performance of QOGI systems.

Environmental factors: As summarized in While average wind speed and temperature provides a convenient summary of overall conditions on a given day, the performance of the emission technologies depends on the instantaneous meteorological conditions as summarized in Table 3.

Accordingly, time-resolved measurements are crucial when interpreting the performance of the technologies and when developing uncertainty estimates (see Sec. 4). Figure 11 and Figure 12 show near instantaneous wind speed and wind direction over a one-hour window on September 27th, which is representative of data collected throughout the field campaign. Data from the various instruments are generally in agreement, albeit with a little more offset between the sources being present in the wind direction data. Discrepancies may be attributed to the fact that the portable ultrasonic anemometer was located 10-20 m away from the release location, while the Davis weather station and fixed ultrasonic anemometer was located near the ATCO trailer, which was located about 250 m away from the stack release locations as shown in Figure 5.

Table 3, all of the quantification technologies are sensitive to instantaneous meteorological conditions. Accordingly, the release schedule was planned to account for diurnal variations in wind speed, ground temperature, and air temperature by conducting identical releases (rate and source type) for each technology in the mornings and afternoons. Figure 17 shows an example of the release schedule as it related to windspeed and temperature measurements from the portable ultrasonic anemometer for September 28th. This allows for better isolation of windspeed effects and release rate effects when investigating how these factors affect the error associated with the technologies.

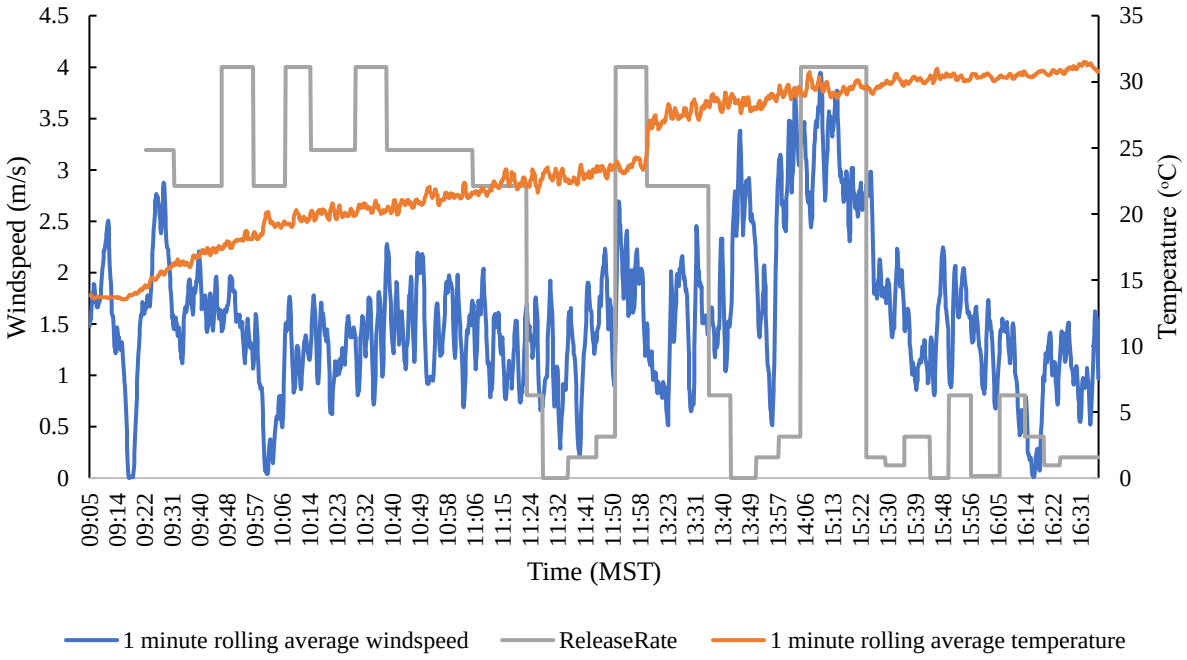

Figure 17: Release rates (normalized to scale of graph) for September 28th as they relate to windspeed and temperature.

The impact of ground and air temperature is particularly important for airborne LWIR HS imaging, which relies on the thermal contrast between the plume and the background. Ground temperature was measured using a handheld infrared thermometer.

Measurement distance: Measurement distance is known to impact the quantification accuracy of QOGI systems [16, 27, 28]. Accordingly, measurements on the stack releases were conducted at

distances of 2.5 m, 5 m, 10 m, and 15 m from the base of the 1.7 m stack. These distances were marked with flags inserted in the ground as shown in Figure 18.

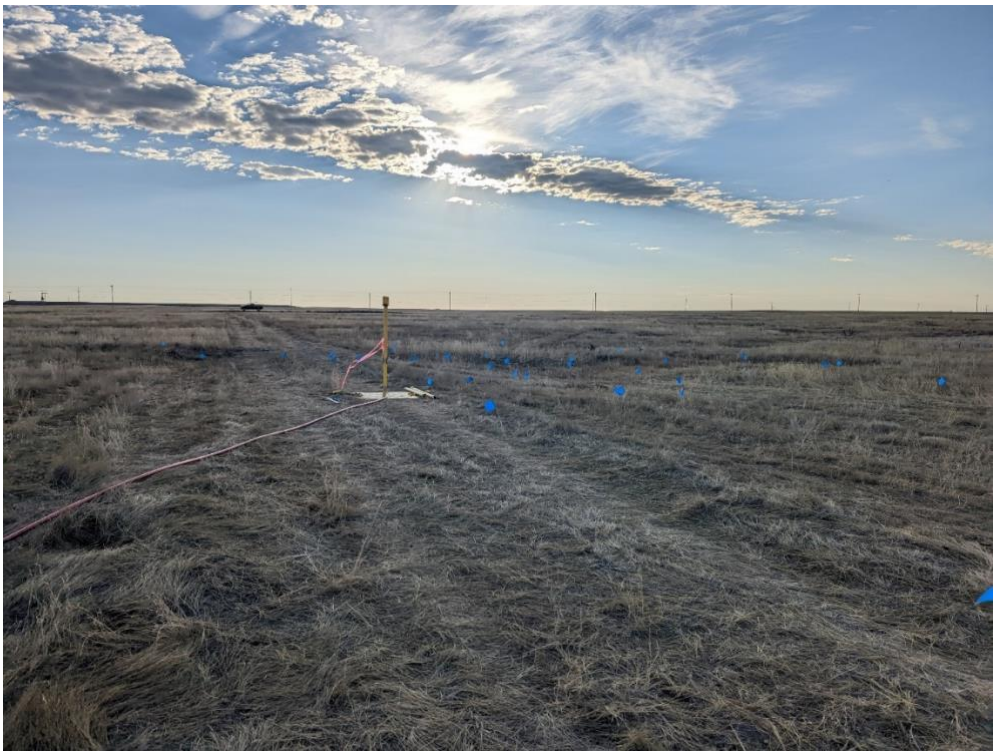

Figure 18: Procedure for measuring distance for QOGI on the 1.7 m stack.

3.0 PRELIMINARY RESULTS FROM THE SECOND FIELD CAMPAIGN

3.1 Assessment of accuracy and treatment of outliers

The error associated with the *k*th measurement is defined as

$$\varepsilon_k = \frac{Q_k^{\text{meas}} - Q_k^{\text{true}}}{Q_k^{\text{true}}} \tag{7}$$

where Q_k^{meas} is the estimated emission rate and Q_k^{true} is the true emission rate, taken to be the value specified on the mass flow controller. The performance of a given technology is summarized by the average absolute error over *N* measurements

$$\varepsilon_{\text{ave}} = \frac{1}{N}\sum_{k=1}^{N}\left|\varepsilon_k\right| \tag{8}$$

as well as the bias,

$$\beta = \frac{1}{N}\sum_{k=1}^{N}\varepsilon_k \tag{9}$$

A positive bias indicates that the technology, on average, overestimates the true emission rate, and a negative bias indicates that the technology, on average, underestimates the true rate.

For the purposes of this report, data points that differ significantly from the majority of the data are identified as potential outliers. Outliers occur for a variety of reasons, including environmental factors or momentary equipment failures. To the extent possible, the origins of the outliers will be identified and discussed. We avoid discarding points that appear as outliers without strong justification, because occasional extreme observations may reflect the true variability of the data and discarding these points would lead to underestimating the uncertainty. In some cases, the results may be presented with and without these data points for context. A similar procedure for outliers will be taken at the modelling stage, where an effort will be made to understand the root cause of the outlier, and the analysis may proceed without the outlying point if appropriate, otherwise results will be provided both with and without the outlier.

3.2 Ground-based MWIR QOGI

This section combines the results of the two QOGI technologies in the second field trial: the FLIR QL320/GFx320 system, operated by UW personnel (Nagorski); and the OPGAL EyeCSite and EyeCGas system, operated by Montrose personnel. This section summarizes the results from the two technologies, and then provides a technical commentary based on lab-scale/modeling carried out under Task 2b (Sec. 1.3.2). This commentary is based primarily on observations with the GFx320/QL320 system, but should also apply to the OPGAL EyeCSite since both systems operate according to similar principles.

3.2.1 Summary of results

Figure 19 summarizes the performance of the FLIR QL320. The average absolute error for the QL320 was 59.43% across 116 measurements. The overall bias over all release rates was +8.62%. Figure 19 shows that the technology had a positive bias at low emission rates (< 10 kg/hr) and skewed towards a negative bias at higher emission rates.

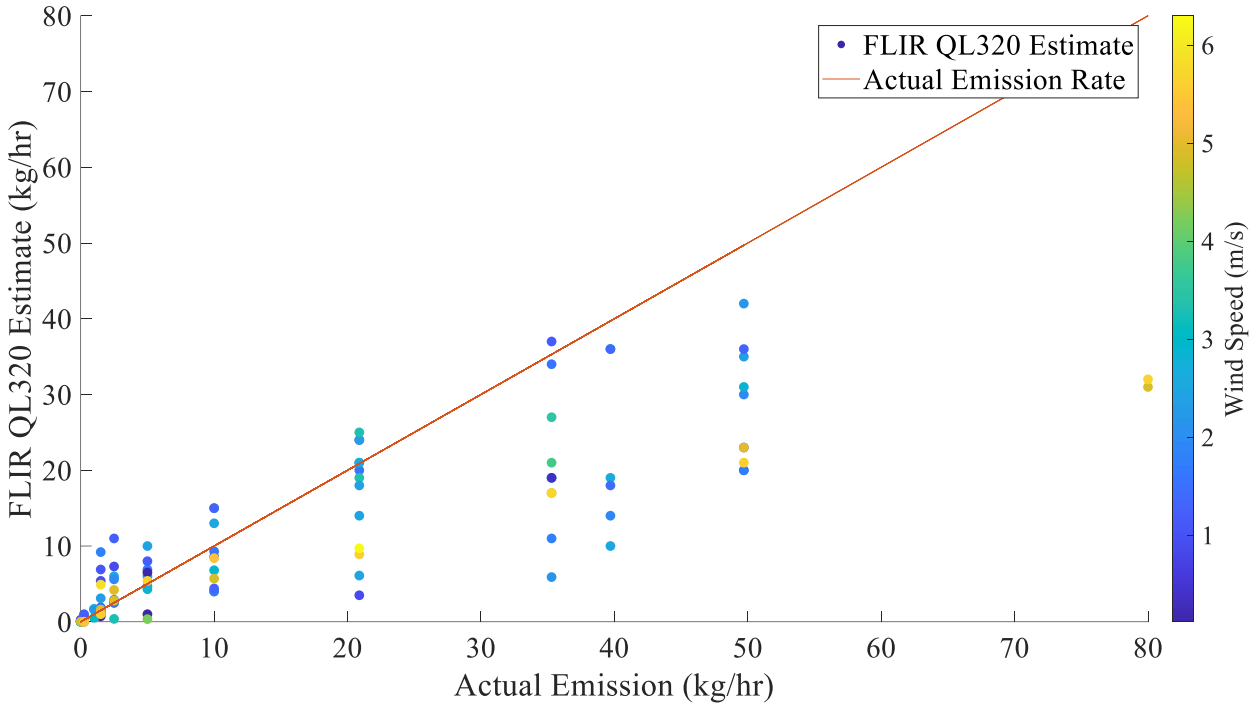

Figure 19: FLIR QL320 emission estimates summary

Figure 20 shows that the OPGAL QOGI estimates tended to underestimate the true emission rate, with an average bias of -42.72%. The average absolute error for the technology was 67.77% across 81 measurements. There were an additional 17 datapoints from the start of September 26th that had to be excluded from the analysis, as the operator forgot to timestamp the measurements.

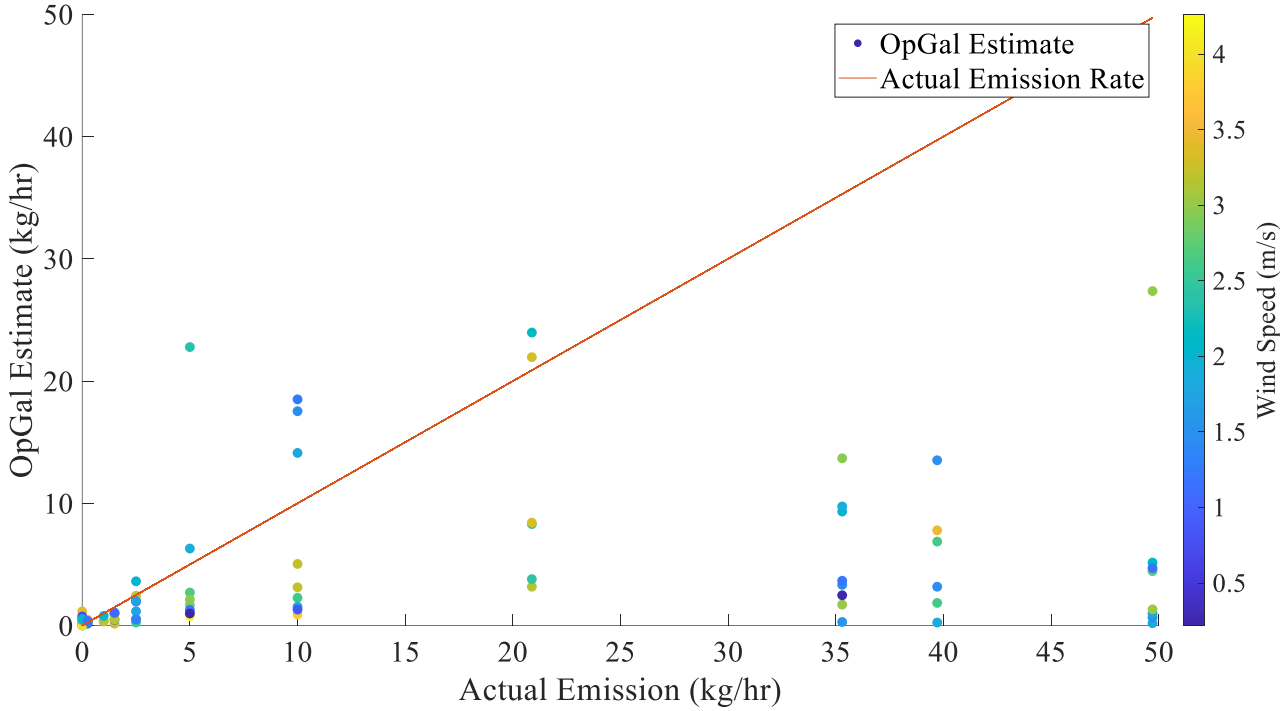

Figure 20: OPGAL EyeCSite emission estimates summary

3.2.2 Effect of wind speed

The impact of wind speed on QOGI detection limits has been discussed in literature [16, 27, 28] and is understood to lower the detection threshold for otherwise identical conditions, although, to the best of our knowledge, no study has focused exclusively on how wind affects the accuracy or uncertainty of QOGI emission estimates. Zimmerle et al. note that a specific wind speed cut-off ranging from 4.5 to 16 m/s is often used by QOGI operators as a formal or informal guideline, above which emission estimates become unreliable [16].

Wind could impact the accuracy of the QOGI estimate through both the velocity and spectroscopic sub-models. Higher wind speeds cause the plume to move faster and disperse to a greater extent, which may lower the column densities. Separately, high winds may generate turbulent features that move faster than can be resolved by the camera. Lower wind speeds have the opposite effect, and under extremely calm wind conditions the plume may stagnate and pool.

Figure 21 shows no immediately obvious trends between wind speed and QOGI accuracy. The bias of the OPGAL measurements skew more positively at higher wind speeds than at lower wind speeds, however it is still negative overall across almost every different emission type. In contrast the FLIR error tended to skew more negatively at higher windspeeds. Overall, however, there was no consistent increase or decrease in the magnitude of the overall error with respect to changes in wind speed.

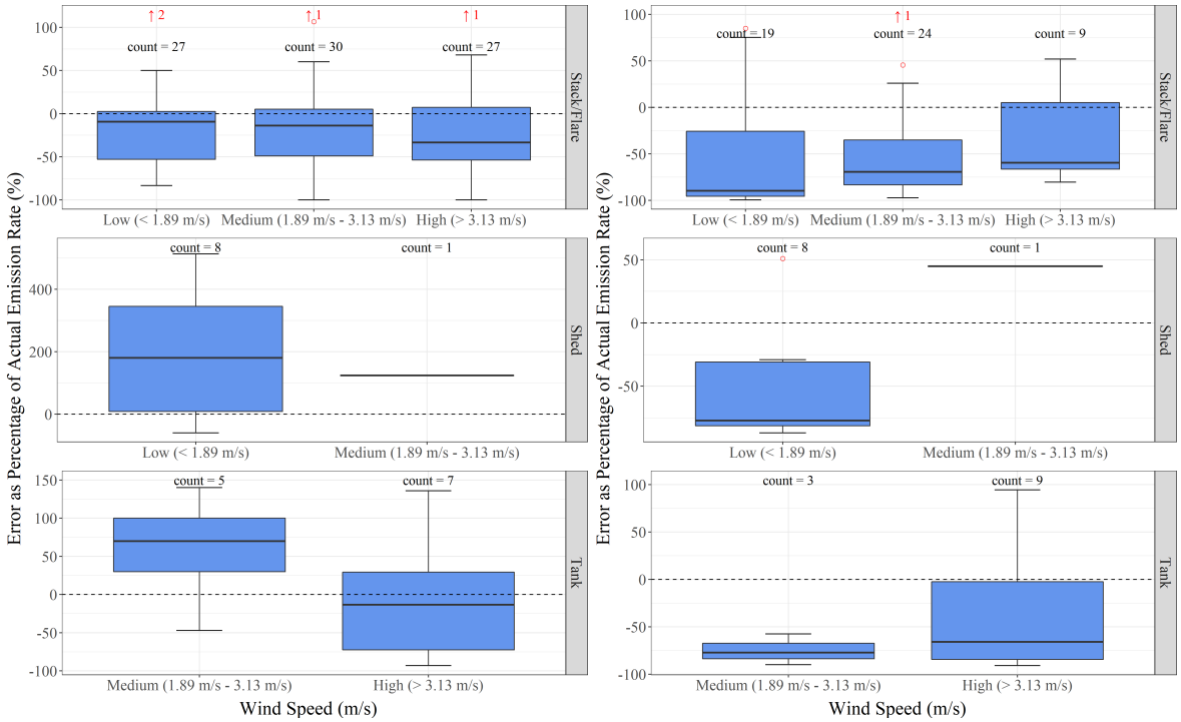

Figure 21: Effect of wind speed on QOGI percentage error; (left) FLIR QL320 (right) OPGAL EyeCSite.

Figure 22 illustrates how high wind speeds impacts the QL320 estimates of a single release rate over the course of 2 minutes. Each individual measurement by the QL320 requires about 5 seconds and this example consists of 10 individual measurements. The impact of wind speed on QOGI is most apparent through video files (included as supplemental information), but can also be seen in a plot of instantaneous flow rate estimates and wind speeds sampled at 0.25 s intervals (4 Hz). The release was from a 4.8 m tall stack at a measurement distance of 5.4 m and flow rate of 20.9 kg/hr, which, as we will show, is far larger than the minimum detection limit (MDL) for the FLIR GFx320 at this distance with clear sky background. During the first minute of the measurement, the wind speed ranged between 1-3 m/s and the QL320 estimates ranged from 12 to 16 kg/hr (–43% to –23% error). When the wind speed suddenly increased to between 2 and 5 m/s the QL320 estimates dropped significantly, ranging from 7 to 9.8 kg/hr (–53% to –66% error). All other variables are assumed to be constant over this period, so this variation may be attributed solely to variation in wind speed.

The increase in error with wind speed could be due to the limited framerate of the GFx320 camera or a reduction in accuracy of the velocimetry algorithm at these higher wind speeds. Based on the measurement distance, field-of-view, and frame rate of the GFx320, and a discussion with Providence Photonics [19], these wind speeds fall within the measurement envelope of the system. The data output of the QL320 does not separate the column density and velocity estimates so it is not possible to discern the change in each quantity when the wind speed changed, but, considering our knowledge of the QOGI sub-models and release rate, this example seems to indicate a reduction in accuracy of the velocimetry algorithm at higher wind speeds.

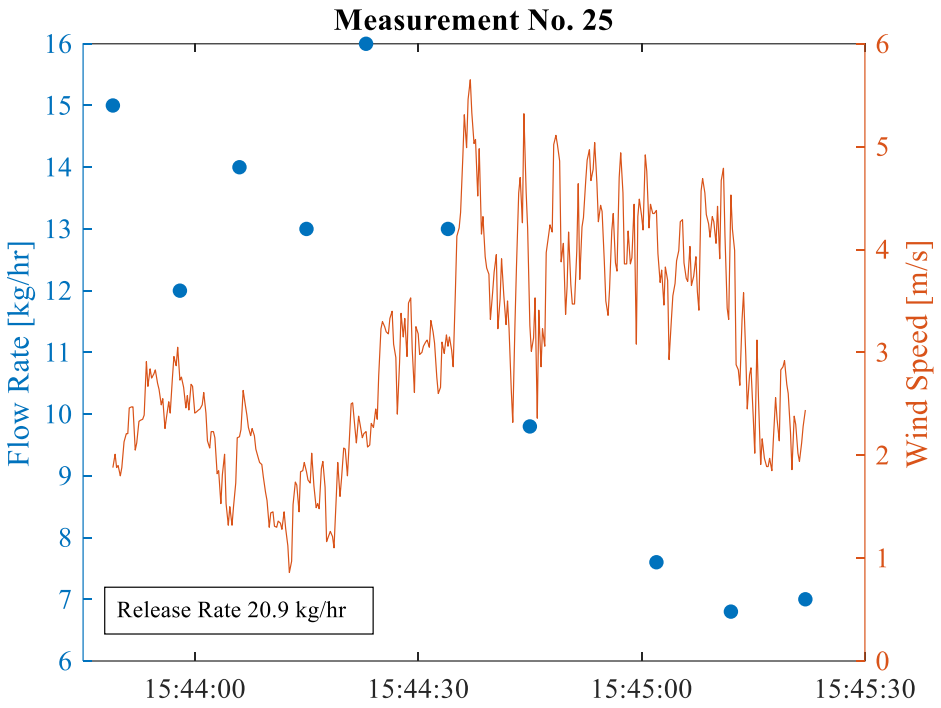

Figure 22: QL320 measurement #25 flow rate estimates and 1/4-second wind speed data. Flow rate estimates are much closer to the actual release rate when the wind was in the range of 1-3 m/s, but when the wind speed increased to 2-5 m/s the flow rate estimates decreased significantly.

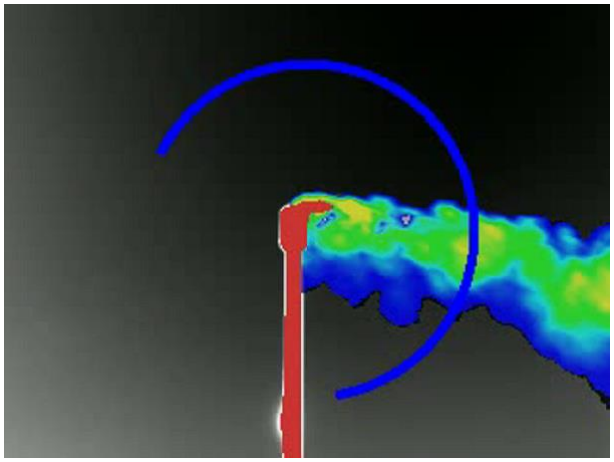

Figure 23: QL320 measurement #25, snapshot showing plume detection overlay and blue circular control line.

However, the observation that higher wind speeds lead to lower QOGI estimates is not consistent across all measurements. Figure 24 shows an example with the same measurement distance and release height but a release rate of 2.5 kg/hr. The wind speed during this 2-minute period fluctuated rapidly but, when inspecting each of the measurement videos, the wind speed was noticeably higher during the 4th, 5th, and 6th recordings, which corresponded to higher QOGI estimates. This

is the opposite wind speed-flow rate estimate relationship that was observed in measurement #25. The MDL of the GFx320 will be discussed in Section 3.2.5, but at this release rate, distance, and temperature contrast, it is not believed that column density error would be responsible for this observation and instead this is likely another effect of wind speed on the velocimetry algorithm.

Measurement #31 also exemplifies a key observation in the 2018 report by the Saskatchewan Research Council, which stated that averaging multiple QOGI measurements improves accuracy by reducing variance [29]. While most of the measurements in this 2-minute window were about 32% to 42% higher or lower than the actual release rate of 2.5 kg/hr, the average was 2.7 kg/hr and the final estimate by the operator was 2.5 kg/hr.

However, it must be noted that averaging multiple measurements to reduce variance only addresses unbiased random error or aleatoric uncertainty and ignores any bias or epistemic uncertainty in the estimate. In other words, if there is a bias present due to any limitation of the QOGI algorithms or techniques, then more measurements will not improve this other aspect of error or uncertainty. This approach also works only if the environmental conditions remain stationary during the measurement duration.

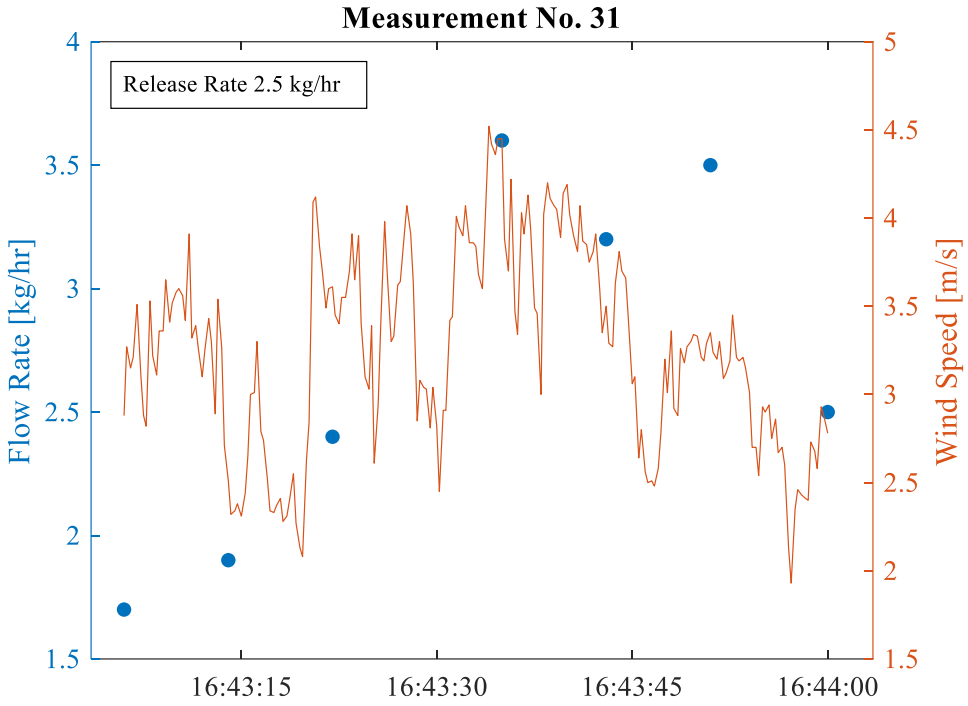

Figure 24: QL320 measurement #31 flow rate estimates and 1/4-second wind speed data. Flow rate estimates are lower when the wind speed was lower and vice-versa, but this correlation is less obvious and opposite to that which was observed in measurement #25.

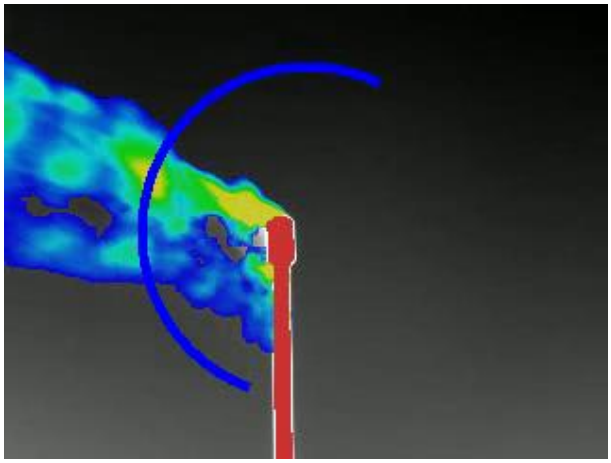

Figure 25: QL320 measurement #31, snapshot showing plume detection overlay and blue circular control line. The plume is noticeably less dense than measurement #25 due to the lower release rate.

Very low wind speeds may cause the plume to disperse very slowly and may even stagnate in the same location; this scenario can also degrade the accuracy of QOGI estimates. As long as there is still some plume advection, it should be possible to infer a velocity and obtain a QOGI estimate but a stationary plume would be problematic.

This scenario is exemplified in Figure 26. The wind became very calm over a number of measurements, causing the instantaneous QOGI estimates to increase significantly; up to three times greater than the actual release rate, whereas the estimates were about 16% to 44% lower than the release rate when the wind was about 1 m/s. Note that missing wind speed data is due to the wind speed being lower than the 0.5 m/s lower limit of the portable ultrasonic anemometer.

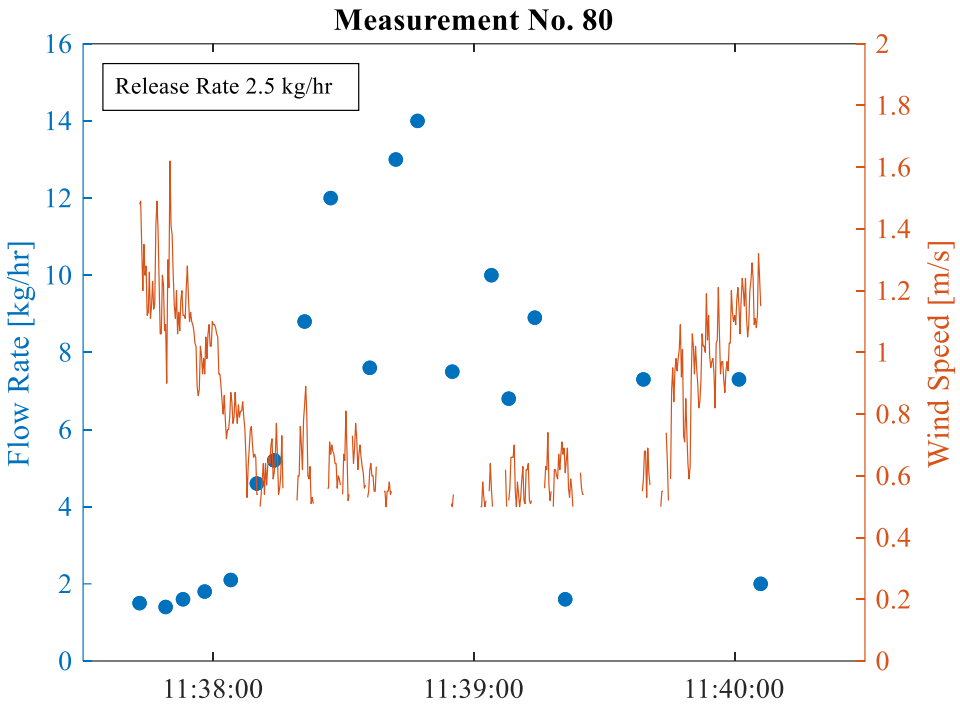

Figure 26: QL320 measurement #80 flow rate estimates and 1/4-second wind speed data. Flow rate estimates became significantly higher when the wind becomes very calm but were otherwise fairly accurate when the wind speed was around 1 m/s. The lower limit of the portable ultrasonic anemometer was 0.5 m/s, so wind speeds were recorded as 0 m/s during these calm conditions.

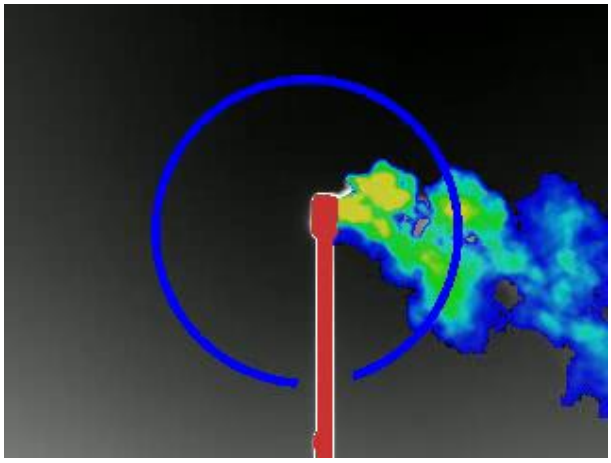

Figure 27: QL320 measurement #80, snapshot showing plume detection overlay and blue circular control line when the wind was very calm. The plume disperses very slowly and is on the verge of stagnating or pooling near the stack exit.

Figure 27 shows a snapshot of the plume when the wind was at its calmest; it is evident from the video that the plume is still moving, albeit slowly. Therefore, the large estimates cannot be attributed to plume pooling, and are likely due to another error in the velocimetry algorithm at very low wind speeds.

These are some of the most apparent effects of wind speed on QOGI measurement in the context of the QOGI sub-models. Unfortunately, these observations did not always apply when comparing measurements under the same test parameters and wind conditions. Understanding the functional impact of wind on QOGI-derived emission accuracy is impaired by the fact that the velocity sub-model is semi-empirical and confidential to the instrument manufacturer. Therefore, while it is hypothesized that the wind speed has a strong effect on the velocimetry algorithm in the QL320, this cannot be confirmed without separate velocity and column density estimates. The statistical analysis of this data will be better able to objectively evaluate the effect of wind speed.

3.2.3 Effect of flow rate

Figure 28 shows the error of the emissions estimates obtained from the FLIR and OPGAL systems with respect to flow rate. The OPGAL system generally performed better at the lower emission rates, with error consistently increasing linearly with increasing flow rate. Further analysis will focus on identifying a coefficient or function that can quantify this error increase. For the FLIR measurements, the effect of emission rate on accuracy is less clear, and different challenges emerge at high and low flow rates. It is unclear why the FLIR and OPGAL systems perform so differently depending on flow rate.

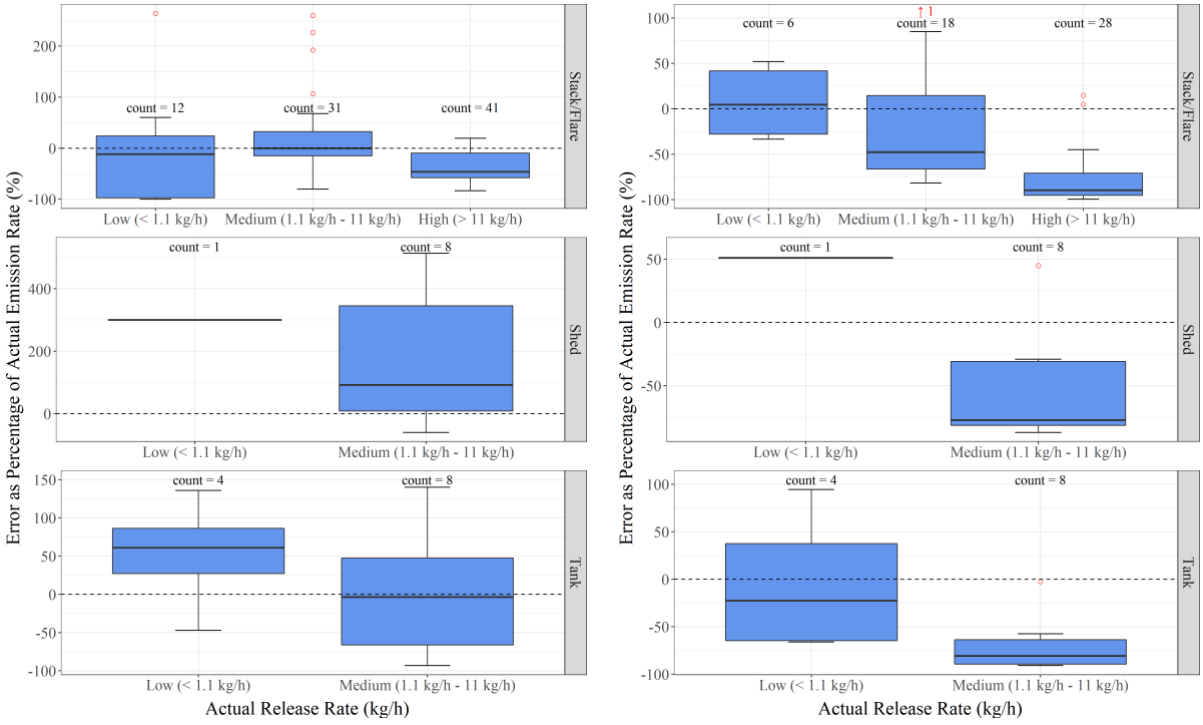

Figure 28: Effect of release rate on QOGI percentage error; (left) FLIR QL320 (right) OPGAL EyeCSite.

High flow rate challenges

Three problems may arise with the QOGI estimates using the QL320 when quantifying high flow rates:

1. Contrary to our initial hypothesis in the first interim report, we now believe that column densities are *not* determined by inverting an analytical RTE model explicitly, but rather via calibration (e.g. matching pixel intensity to a measurement made with a known column

density). This means there may be an upper limit to the column densities estimated by the algorithm, corresponding to the maximum column density included in the calibration. This upper limit may be exceeded depending on the flow rate, distance, and wind speed and will result in an underestimation of the actual flow rate since the actual column density exceeds the estimated column density. This hypothesis is supported by the available patents , literature , and a FLIR white paper but cannot be confirmed by the data output of the QL320. There is also a physical limit to the maximum column density that can be inferred as the plume concentration and thickness increases because the plume will become "optically thick," effectively making the pixel intensity insensitive to the true column density. The calibration of the QL320 may extend to this physical limit, or stop earlier as the sensitivity to changes in column density decreases.

2. High flow rates originating from small orifices result in highly concentrated and turbulent plumes which may inhibit the motion tracking done by the velocimetry algorithms in QOGI. In other words, we observed instances in which the plume was so dense and turbulent that the turbulent structures in the plume evolved faster than could be resolved by the limited camera framerate. When this occurs, the velocimetry algorithm cannot reliably infer the velocities of gas-containing pixels and the estimated flow rate is likely to be lower than the actual flow rate. Again, it is difficult to confirm this hypothesis because the algorithm and output of the velocimetry sub-model is unknown.
3. Exclusive to the QL320, the plume detection algorithm becomes unreliable when imaging high flow rates as portions of the plume are consistently not identified. When these non-detected gas-containing pixels cross the blue control line, they are not included in the flow rate estimate which will lead to systematic underestimation in the overall emission rate.

Measurement #24 exemplifies these issues. The release rate was 49.7 kg/hr from the 4.8 m tall stack and the measurement distance was 5.4 m. The highest flow rate obtained from QOGI during this measurement was 43 kg/hr and the final estimate made by the operator was 35 kg/hr, representing errors of -13% and -30% respectively. The FLIR white paper on QOGI says that the QL320 has been calibrated up to 300 SLPM (12.7 kg/hr) , but the measurement distance is not specified, which should be an important factor in the quantification. Figure 29 shows a snapshot of one of the recordings with the plume detection overlay present, and it can be seen that portions of the plume are consistently excluded by the detection algorithm. It is unclear why the plume detection fails in these high flow rate scenarios.

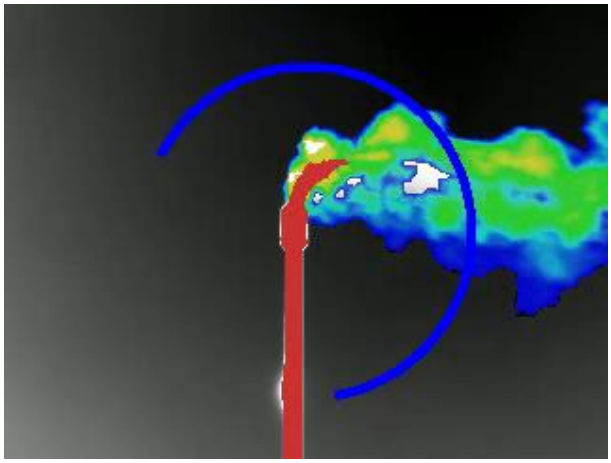

Figure 29: QL320 measurement #24, sample image showing that the plume detection algorithm does not identify some of the densest parts of the plume which would lead to underestimation of the flow rate.

Figure 30 shows a snapshot from the same recording but without the plume detection overlay so that the plume can be seen in its unmodified form. In this case the plume is very dense throughout and there is less contrast or brightness gradient within the plume compared to if the plume was sparse with sky background pixels intermixed. This can make velocimetry less accurate because feature tracking requires a brightness contrast between neighboring pixels.

Figure 30: QL320 measurement #24, sample image showing the raw capture of the release without any overlays. The plume is relatively dense throughout which reduces the contrast within the plume and may make velocimetry less accurate.

Low flow rates and minimum detection limits (MDLs)

Zeng and Morris produced a theoretical equation for the MDL (in kg/hr) of an OGI measurement based on the radiative intensity difference versus noise on a pixel level as a function of the gas species, temperature of the gas, apparent temperature of the background, camera, lens, distance, and dispersion conditions :

$$\mathrm{MDL} = C \cdot \alpha \left[\left| \Delta T \right| \right]^{\beta} \cdot d^2 \cdot w \cdot \frac{P}{T} \cdot \frac{MW}{R} \tag{10}$$

where C is a constant specific to a camera and lens, α and β are constants specific to a gas and camera, T is the ambient temperature (which is used to approximate the gas temperature), ΔT is the temperature difference between the gas and background, d is the measurement distance, w is a variable that is influenced by the dispersion conditions (i.e. wind and gas exit velocity), P is the ambient pressure, MW is the molecular weight of the gas species, and R is the ideal gas constant . Table 5 summarizes these parameters as they pertain to the test conditions of the second field trial.

Table 5: Parameters for theoretical calculation of QOGI minimum detection limits .

FLIR GFx320 with 23mm lens	$C = 6.17 \times 10^{-5}$
Methane emissive plume	$\alpha = 18010$ $\beta = -1.530$
Typical dispersion conditions	$w = 35\,\mathrm{m^3/L\text{-}hr}$
Ambient pressure	$P = 1\,\mathrm{atm}$
Molecular weight of methane	$MW = 16.04\,\mathrm{g/mol}$
Ideal gas constant	$R = 0.08206\,\mathrm{atm\text{-}L/gmol\text{-}K}$

Note that the variable w for the dispersion conditions is based on empirical observations by Zeng and Morris and the authors state that further work needs to be done to substantiate its value. Nonetheless, substituting these parameters into Eq. (10) yields:

$$\mathrm{MDL} = 7.602 \frac{\left(\left| \Delta T \right| \right)^{-1.530}}{T} \cdot d^2 \ \text{(kg/hr)} \tag{11}$$

Equation (11) can be used to calculate the theoretical minimum detection limit for each measurement given the ambient temperature, apparent background temperature, and distance. While this study was not designed to evaluate QOGI detection limits, it is useful to identify measurements that may lie below the MDL and would therefore be difficult to quantify. Furthermore, measurements near the MDL can be identified and considered more carefully to better understand the effect on quantification accuracy.

For measurement distances less than 10 m, the theoretical MDL was always considerably lower than the lowest release rate (0.25 kg/hr). Therefore, this study draws no conclusions regarding the validity of the theoretical MDL equation for measurements closer than 10 m.

For measurement distances of 10 m and 15 m, Eq. (11) shows that detection of the 0.25 kg/hr releases should not be possible. However, in some instances, gas was still detectable using the "high-sensitivity mode" which highlights relative changes in pixel intensities between frames, making small gas plumes more apparent. For releases of 1.5 kg/hr at 10 m and 15 m, the accuracy of the QOGI estimates sometimes deteriorated as the release rate approached the MDL. More testing near these theoretical MDLs should be done to better understand the effect on QOGI accuracy.

3.2.4 Effect of distance

The effect of distance on QOGI estimates overlaps with the effect of flow rate. Increasing measurement distance increases the MDL since it decreases the intensity incident on the detector

in proportion to $1/d^2$ per Eq. (10). Distance also influences the velocimetry sub-model. Larger measurement distance increases the footprint of the frame and spatial size of pixels, assuming the optics are fixed. With more of the plume in frame at a larger measurement distance, this can provide more information for the velocimetry algorithm, unless the measurement distance becomes so large such that the spatial resolution is insufficient to resolve details in the plume which will adversely affect the velocimetry algorithm.

Figure 31 shows the effect of measurement distance on the accuracy of the QOGI estimates for the FLIR QL320 and OPGAL EyeCSite. One commonality between the two systems is that measurements at 2.5 m tend to have the highest percentage errors. During the field trials both operators reported that 2.5 m seemed too close to obtain a reliable estimate, particularly at higher release rates. At such a short measurement distance, a plume may comprise a significant portion of the frame and make it difficult to: 1) contain the entire plume within the quantification control line as seen in Figure 32, and 2) estimate the bulk velocity of the plume with the velocimetry algorithm because the plume advects so rapidly relative to the scene footprint and frame rate. Measurement #49 with the QL320 clearly shows these challenges. The plume fills a significant portion of the blue control line and frame, and when reviewing the video frame-by-frame it is very difficult for the eye to track the turbulent features of the plume (see supplemental information). The result is that the QL320 estimate was only 6.1 kg/hr while the release rate was 20.9 kg/hr which is an error of -71%. It is unlikely that this amount of error is due to the column densities and challenges with high flow rates discussed in Section 3.2.3 because this flow rate was estimated accurately at larger measurement distances. Ultimately, however, the hypothesis that the velocimetry becomes inaccurate at such close measurement distances and large flow rates cannot be verified because the column densities and velocities are not given separately.

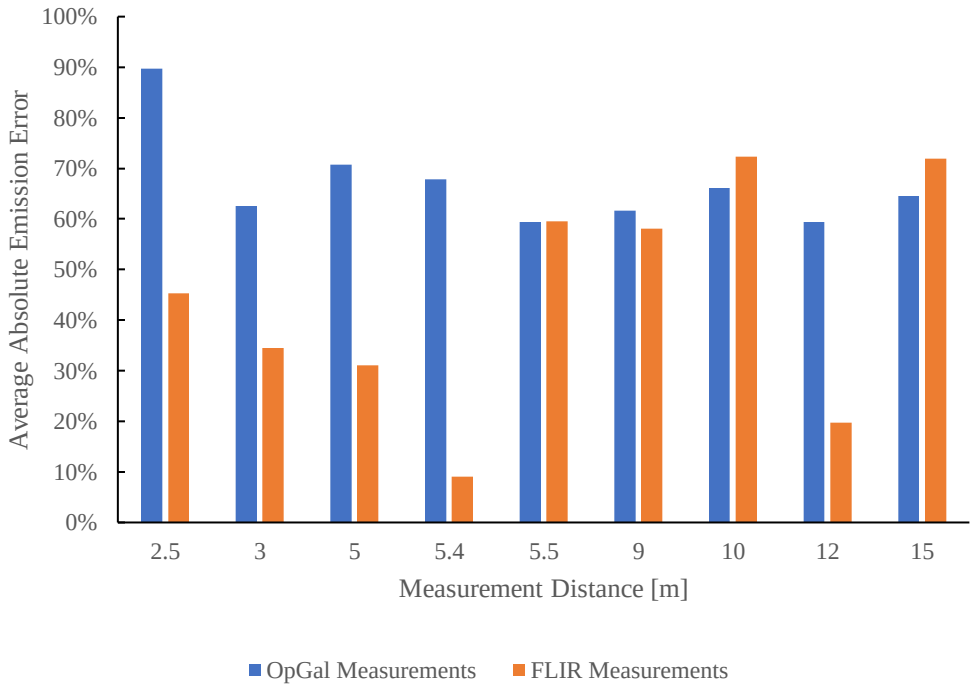

Figure 31: QOGI measurement error with respect to measurement distance

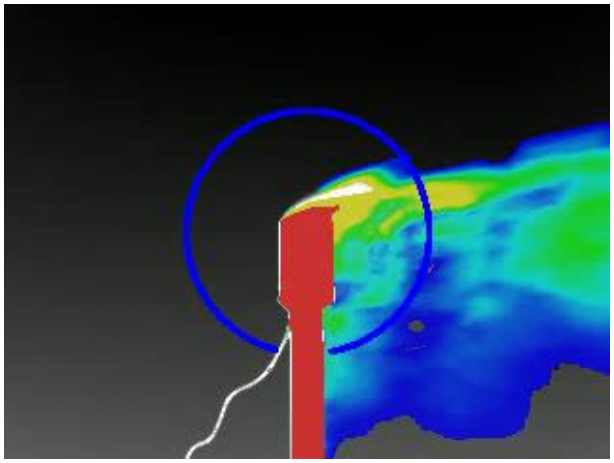

Figure 32: QL320 measurement #49 showing a 20.9 kg/hr release rate at 2.5 m measurement distance. The measurement distance is too close to measure this large flow rate. The QL320 estimate was 6.1 kg/hr which is an error of -71%.

For the QL320 at lower flow rates, a close measurement distance of 2.5 m seems to be less problematic. Figure 33 shows a snapshot from the QL320 of a 1.5 kg/hr release at 2.5 m measurement distance. The plume is much more contained within the blue circular control line compared to the larger release rate shown in Figure 32. The final estimate for this measurement was 1.6 kg/hr which is an error of +7%.

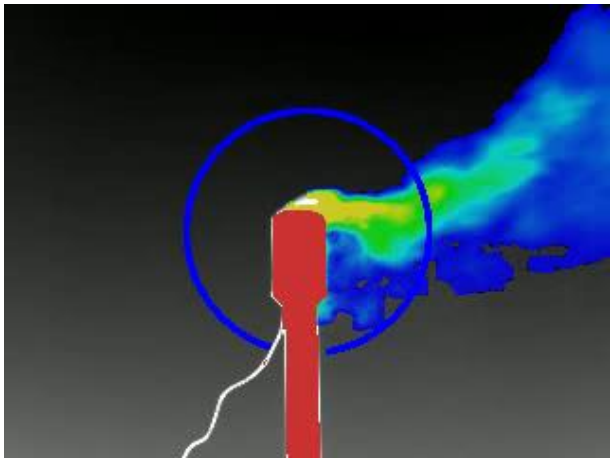

Figure 33: QL320 measurement #53 snapshot showing a 1.5 kg/hr release at 2.5 m measurement distance. The plume is much more contained in the blue circular control line compared to measurement #49 in Figure 32. The final estimate was 1.6 kg/hr (+7%).

A close measurement distance seems to have affected the OPGAL EyeCSite measurements more than the FLIR QL320. It is unclear why this may be the case because our experience with the EyeCSite is limited to observing the Montrose operator perform measurements. It may be that the control line selection in the EyeCSite user interface is less suited to closer measurement distances.

3.2.5 Effect of release height and line-of-sight angle

Releases were made from a 1.7 m, 3.4 m, and 4.8 m tall stack and from a 13 m tall unlit flare. The release height affects the dispersion conditions of the plume due to the location of the release within the atmospheric boundary layer. Higher release heights will experience higher wind speeds

than lower release heights, so the discussion from Section 3.2.2 on the effect of wind speed applies here.

Release height also impacts measurement distance. Higher release heights prevent the QOGI operator from getting closer to the source unless scaffolding or some other elevated platform is used. A longer measurement distance reduces the MDL as discussed in Section 3.2.4, and a statistical analysis on the effect of measurement distance to QOGI accuracy is ongoing.

Finally, release height limits the line-of-sight angle of the measurement when using a sky background. With a higher release height, a QOGI operator is able to move under the source and use a more vertical line-of-sight angle, whereas lower release heights require the operator to use a more horizontal line-of-sight angle. This affects the background temperature contrast since the apparent temperature of the sky near the horizon is greater than the sky directly upwards due to differences in the pathlength of atmospheric emission. This effect on temperature contrast affects the MDL as discussed in Section 3.2.4.

Examples of the effect of release height and line-of-sight angle on QOGI are shown in Figure 34. Both measurements involved similar flow rates (2.5 kg/hr and 1.5 kg/hr, respectively) and measurement distances (12 m and 10 m, respectively), but one is from an unlit flare, while the other is from a 1.7 m tall stack. The measurement of the unlit flare at a higher release height enabled a vertical line-of-sight angle, resulting in a higher background temperature contrast of 12.1°C and more accurate estimate with only +12% error. In contrast, the measurement of the 1.7 m tall stack at a similar distance required a more horizontal line-of-sight angle, resulting in a lower background temperature contrast of 5.5°C and less accurate estimate with +260% error. It should be noted that the exit diameter of the unlit flare is much larger than that of the stack, which produces different dispersion conditions, and the wind speeds and ambient temperature are different for these measurements.

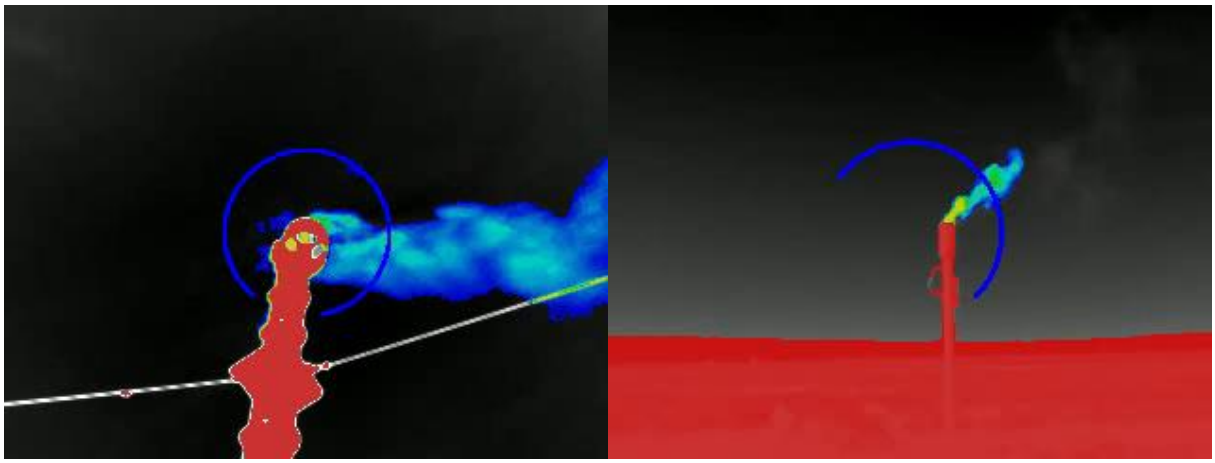

Figure 34: QL320 measurements showing effect of release height and line-of-sight angle. (Left) measurement #118 of an unlit flare release at 12 m vertical measurement distance. The QOGI estimate was 2.8 kg/hr while the actual release rate was 2.5 kg/hr (+12% error). The thermal contrast between gas and background was 12.1°C. (Right) measurement #9 of a 1.7 m tall stack release at 10 m measurement distance. The QOGI estimate was 5.4 kg/hr while the actual release rate was 1.5 kg/hr (+260% error). The thermal contrast between gas and background was 5.5°C. There is a clear temperature gradient in the sky background.

3.2.6 Effect of cloud cover

When performing QOGI using a sky background, the impact of clouds may impair the accuracy of emission estimates or render the measurement infeasible altogether. Clouds increase the apparent temperature of the background compared to a clear sky and introduce non-uniformity in the background. QOGI is still possible against a cloudy background provided there is sufficient temperature contrast between the clouds and gas plume. Previous studies by Concawe [33] and the Saskatchewan Research Council [29] recommended a ΔT of at least 5°C and 10°C, respectively. These recommendations appear to be conservative as QOGI can still perform relatively well with a ΔT of about 3°C, as demonstrated in Figure 35.

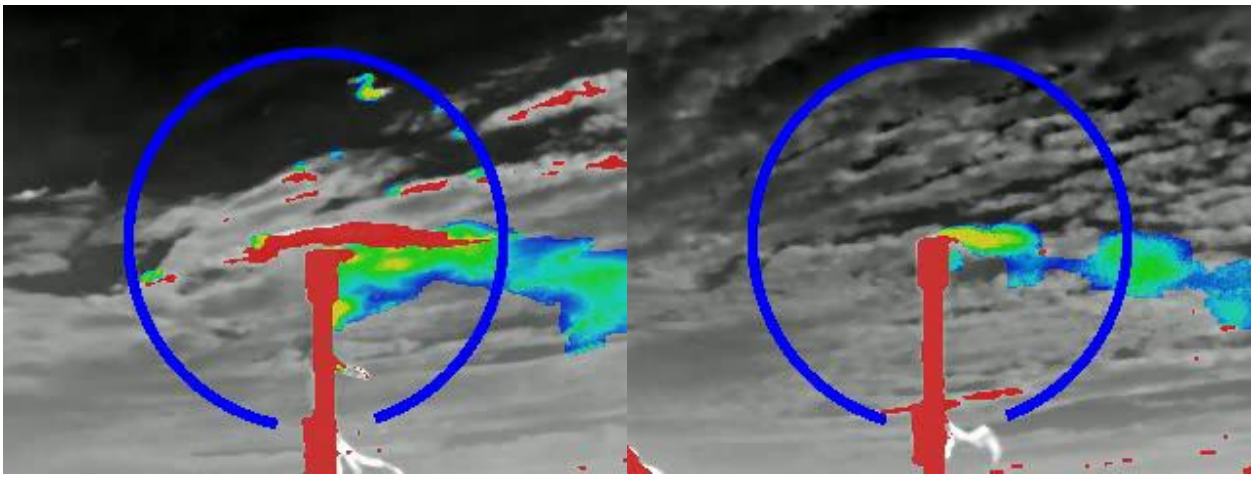

Figure 35: QL320 measurement snapshots showing (left) relatively uniform cloud coverage behind plume (right) relatively non-uniform cloud coverage behind plume. The left image was from measurement #109 at a release rate of 10 kg/hr and the QL320 estimate was 8.4 kg/hr, while the right image was from measurement #113 at a release rate of 2.5 kg/hr and the QL320 estimate was 4.2 kg/hr. The temperature difference between ambient temperature gas and cloud background was only 3.3°C to 4.1°C.

Since cloud coverage cannot be controlled systematically, it was not possible to conclusively isolate the effect of cloud coverage on QOGI performance. This example demonstrates that QOGI with a cloudy background is still possible, with some caveats. It is also notable that uniform cloud coverage is preferable to non-uniform cloud coverage, for several reasons. First, background temperature is taken as the average of the radiometric or apparent temperature of the pixels along the blue control line, excluding any gas-containing pixels. Any non-uniformity along this blue line will influence the average and potentially make the background temperature unrepresentative of the true background temperature behind the plume. Second, background non-uniformity directly behind the plume will augment the intensities of the gas-containing pixels. These two effects will introduce error in the estimated column densities and therefore the flow rate estimates.

Figure 36 serves to demonstrate that cloudy backgrounds can make QOGI unfeasible due to the decrease in temperature contrast between background and gas. The same release rate was used during both measurements, but the presence of clouds in the background on the left reduced the temperature contrast and made visualization, and therefore quantification, impossible when the same release rate was quantified accurately against a clear sky.

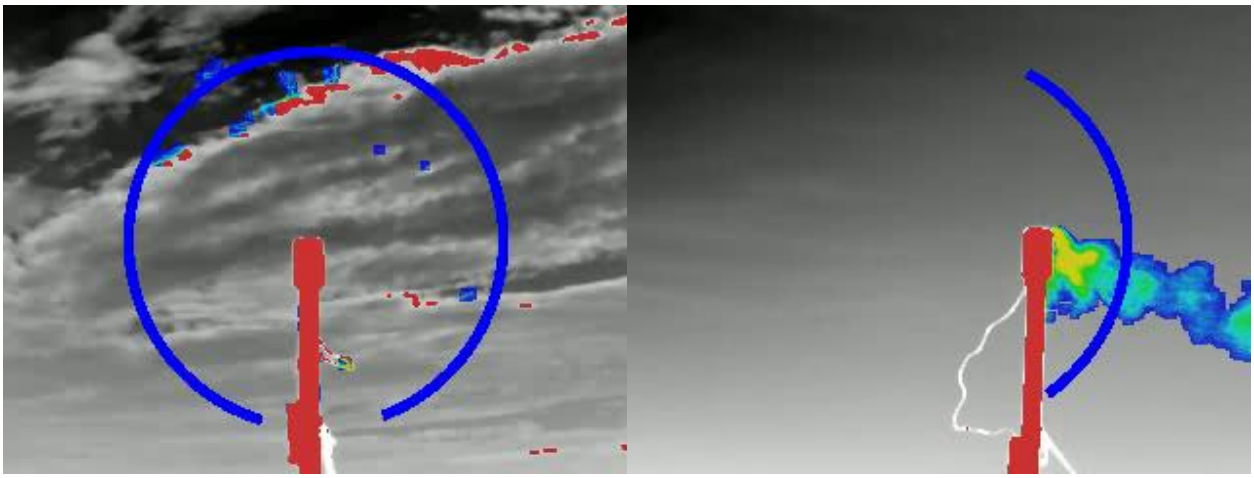

Figure 36: QL320 measurement snapshots showing 0.25 kg/hr release rates at 5 m against (left) cloudy background (right) clear sky background. The left image was from measurement #110 where the QL320 estimate was 0 kg/hr, while the right image was from measurement #59 where the QL320 estimate was 0.23 kg/hr. The temperature difference between gas and background was about 9°C with the clear sky but only 4.4°C with the cloudy background. The ambient temperature was 30°C during the clear sky measurement and 19°C during the cloudy sky measurement.

Cloud coverage may also interfere with the velocimetry algorithms used in QOGI if the clouds are noticeably moving during the measurement. When cloud cover was present during the second field trial, they were relatively stationary over the measurement duration, so this effect is not expected to have introduced any error.

3.2.7 Low ambient temperature conditions

As highlighted in Eq. (10), there must be sufficient temperature contrast between the gas plume and background to make a QOGI measurement. An interesting situation was encountered during the field trial in the morning of September 28th, when, from 9 AM to 10:30 AM, the ambient temperature increased rapidly from 14°C to 19°C. During this time, QOGI measurements were difficult to carry out against the clear sky background because the apparent temperature of the sky was very near the ambient temperature gas, likely due to the longer atmospheric pathlengths involved with near horizontal measurements. While the gas plume was still visible, as seen in Figure 37, large sections of the plume were not detected by the QL320 plume detection algorithm and therefore not quantified. This led to estimates in the range of 50% to 75% lower than the actual release rate. This result is somewhat counterintuitive because typically a clear sky background is ideal for QOGI as the apparent background temperature will be much lower than the ambient air.

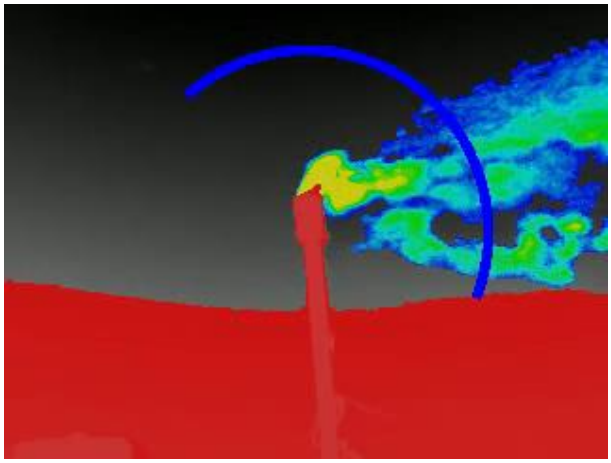

Figure 37: QL320 measurement #68 showing QOGI challenges when the gas temperature is near the background temperature. A significant portion of the plume is not detected and not quantified.

3.2.8 Operator experience and bias

Operator experience is known to have a significant impact on QOGI detection probabilities [16]. This study included only two QOGI operators, each using different devices, so it is impossible to isolate the impact of operator experience on QOGI accuracy. Both operators were trained in QOGI, but the Montrose operator was using the OpGal EyeCSite system for the first time and experienced some difficulties on the first day of measurements. It was discovered near the end of the day on September 26th that the Montrose operator was not properly "NUC-ing" (non-uniformity correction) the camera. This could have introduced some unknown error in their QOGI estimates from that day. A comparison of the performance of the QOGI technologies at each release scenario can be seen in Table 6. These results are based only on releases for which both QOGI technologies provided an estimate; data from September 30th for the FLIR camera, as well as some data from September 26th are omitted.

Table 6: QOGI Performance comparison

Scenario	Number of measurements	FLIR Abs. Error, ε_{ave}	OpGal Abs. Error, ε_{ave}	FLIR Bias, β	OpGal Bias, β
1.7m-4.8m Stack	51	39%	71%	-9%	-42%
13m Flare	5	20%	59%	+0%	-53%
Tank	14	59%	62%	+17%	-44%
Shed	10	205%	62%	+180%	-39%

Throughout testing, the Montrose and UW QOGI operators conducted their measurements in close proximity but were intentionally blinded to each other's estimates. There was some consultation at times when the test conditions were difficult, such as during cloud cover and far measurement

distances, but this was only to provide feedback on the design of the study and maximize the usefulness of the data collected.

The UW QOGI operator, Michael Nagorski, has contributed comments specific to his perception of operator experience and bias:

1. One technique that was used was masking the blue control line and moving it closer to the release point in order to quantify lower release rates, as seen in Figure 38 (right). It may be intuitive for some operators to always center the leak source in the blue control circle, but in this scenario the gas plume may become undetectable by the time it reaches the blue control line. By masking and moving the control line closer to the source, quantification can be more accurate. This is an example of how operator experience may improve QOGI accuracy.
2. Heuristically-adjusted settings in the QL320 user interface can introduce subjectivity to the estimates, particularly since these settings are poorly-defined. For example, the use of "expert mode," which continuously estimates the flow rate and indicates when the instantaneous flow rate is within a certain percentage of the time-averaged flow rate, can affect QOGI accuracy and depends on the operator's experience and/or preference. Another example is the behavior of the blue control line, which typically resizes itself according to the measurement distance but has a large transition in size around 11 m. The position and size of the blue control line is critical to a QOGI estimate and being able to manipulate it effectively is likely one of the biggest factors in operator experience, alongside the operator's choice of measurement distance and background, which were mostly controlled in this study. Lastly, the wind speed setting which the operator must specify in the QL320 is ambiguous. It is not clear what this setting changes; selecting different wind speed ranges under the same environmental conditions sometimes changes the estimate but other times has no effect. Overall, the QL320 is very user-friendly but the ambiguity of certain features introduces uncertainty and subjectivity into the estimate.
3. After reviewing all the QL320 estimates against the actual release rates, one scenario in particular seems to have introduced a positive bias into some of the UW-derived emission rates. Due to the aerodynamics surrounding the stack, the plume would often be drawn into the low-pressure wake region, leading to challenging dispersion conditions for QOGI, as seen in Figure The UW QOGI operator noticed this behavior and believed that a portion of the plume could be missed by the QL320 at close measurement distances (2.5 m) as the blue control line seemed too close to the source. Therefore, he was biased towards the higher instantaneous estimates when providing his final estimate. The actual release rate was 1 kg/hr and his final estimate was 1.6 kg/hr (+60% error) whereas most instantaneous estimates were between 0.9 and 1.1 kg/hr.

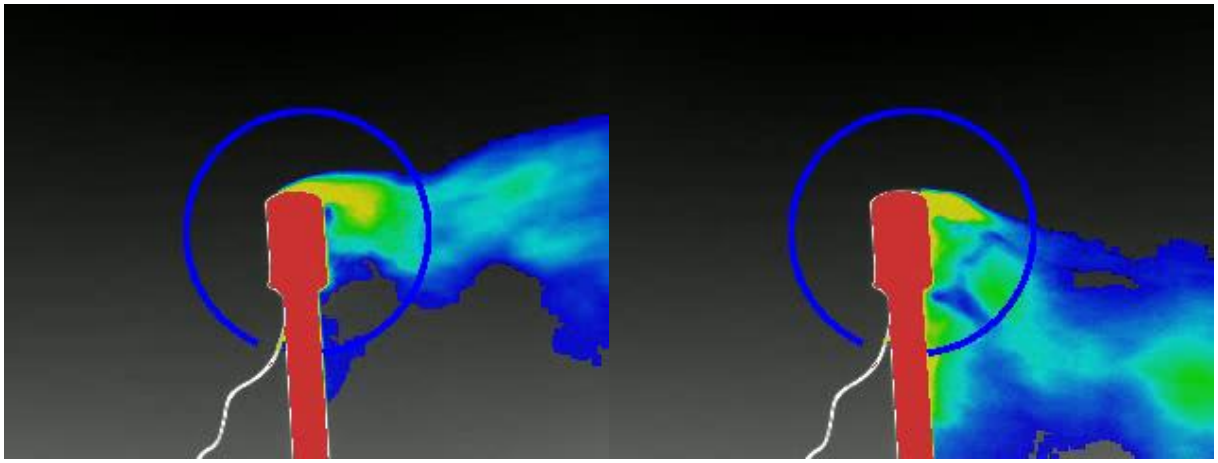

Figure 38: QL320 measurement #4, snapshots showing (left) ideal plume dispersion (right) significant downwash of the plume into the wake of the stack

3.2.9 Effect of emission type on error

As has been seen throughout Section 3.2 of this report, the effect of emission type (stack, flare, shed, and tank) was not consistent between each of the technologies. For the OPGAL measurements, different emission types did not have a very pronounced impact on the overall accuracy. The error associated with short stack measurements was highest at 71%, while average estimate errors for the flare, tank, and shed were all between 59% and 62%. Furthermore, the bias of the OPGAL measurements was not significantly impacted by emission type, with all associated biases being between -39% and -53%.

In contrast, the emission type had a more profound impact on the error of the FLIR measurements, particularly with shed measurements. The error was smallest for the short stack at 43%, with the flare and tank measurements having average absolute errors of 54% and 59% respectively. And finally, the shed measurements having an average absolute error of 205%. In addition, the bias of the tank and shed measurements skewed very positively, whereas the bias was negative for the short stack and flare measurements.

FLIR tank and shed measurements

It is difficult to draw definitive conclusions and recommendations about QOGI measurements of shed and tank releases because the results were inconsistent and the estimates were often very inaccurate compared to the stack releases.

In general, releases from the side of the shed led to pooling around the source as the plume was shielded from the wind. In some cases, the gas would exit the side of the shed in a steady plume, as seen in Figure 39 (left), but most of the time it would pool and meander which made QOGI very inaccurate, as seen in Figure 39 (right). The former estimate was 1.1 kg/hr (–27%) while the latter estimate was 9.2 kg/hr (+513%); the actual release rate was 1.5 kg/hr. Also notice in Figure 39 (right) that the plume detection algorithm identifies the reflection of the plume on the aluminum paneling of the shed. It is unclear whether this could affect the QOGI estimate due to the proprietary nature of the algorithm. The accuracy of QOGI-derived estimates in these situations could very likely be improved by waiting for the perfect conditions so that the plume disperses in an ideal manner. Zimmerle et al. observed that longer survey times increased detection probabilities by 1.3 to 2.4 times, depending on the operator's level of experience [16], which is particularly germane to challenging measurement scenarios such as these.

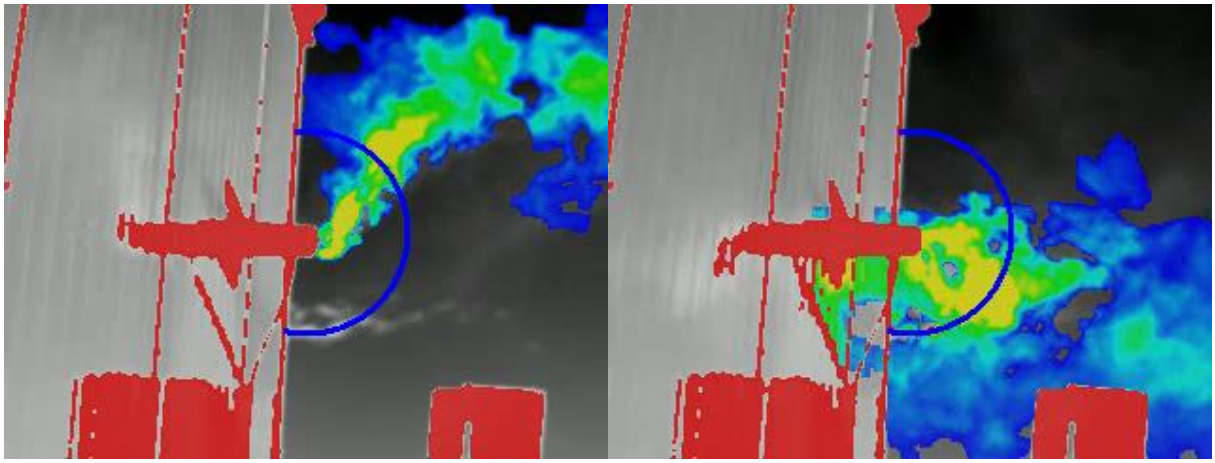

Figure 39: QL320 measurement #90, snapshots showing (left) steady plume being formed which is ideal for QOGI and (right) gas pooling which makes QOGI very inaccurate. The (left) estimate was 1.1 kg/hr while the (right) estimate was 9.2 kg/hr. The actual release rate was 1.5 kg/hr.

The main challenge with quantifying the tank releases was that the size of the tank and location of the release limited the operator's positioning, while equipment on the top of the tank further obstructed the line-of-sight between the operator and the release. Two release configurations were tested: in the first scenario the hose was pointed upwind, while in the second the hose was pointed downwind. The measurement distance was 9 m. Releasing into the wind was generally more challenging as quantification had to be done either closer to the source where the column densities are greater but part of the plume is obstructed by the pipe, or further from the source where there are no obstructions but the column densities are lower due to plume dispersion. Figure 40 shows QOGI images for these two cases; the corresponding estimates were 4.3 kg/hr (–57%) and 0.6 kg/hr (–94%), respectively, while the actual release rate was 10 kg/hr.

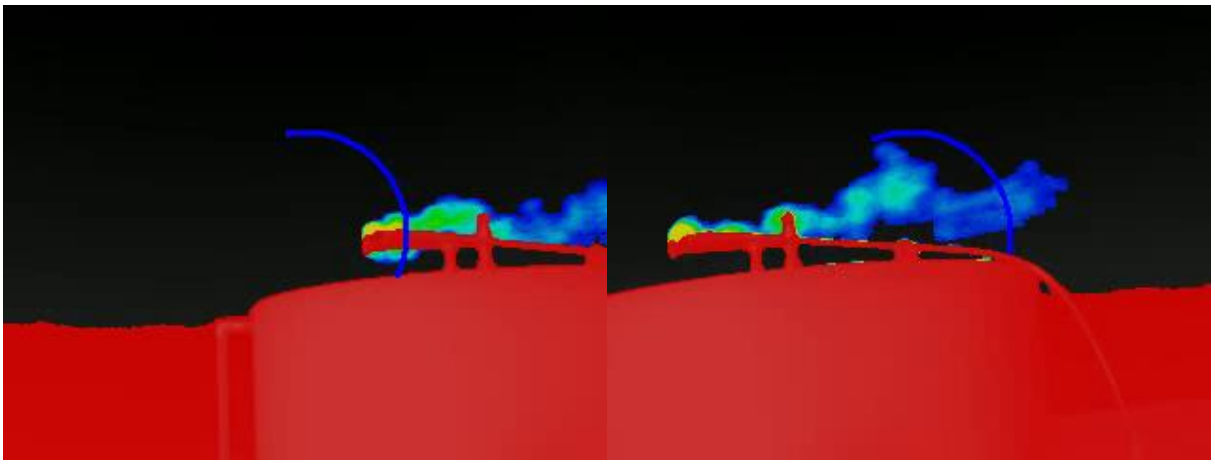

Figure 40: QL320 measurement #36 which was an upwind tank release. Snapshots showing (left) quantification close to the source with obstruction, and (right) quantification further from the source without obstruction. The estimates were 4.3 kg/hr and 0.6 kg/hr, respectively, while the actual release rate was 10 kg/hr.

The estimates from downwind releases were slightly more accurate. However, another challenge with the tank is that slight changes in wind direction, or complicated aerodynamics over the top of the tank, can make some measurements very inaccurate as the tank walls obstruct the plume, as seen in Figure 41 (right). The estimates were 1.6 kg/hr (+7%) and 0.57 kg/hr (–62%), respectively, while the actual release rate was 1.5 kg/hr. Frequently repositioning the camera in these situations would be cumbersome, so it is recommended that more QOGI measurements be made to mitigate this potential error.

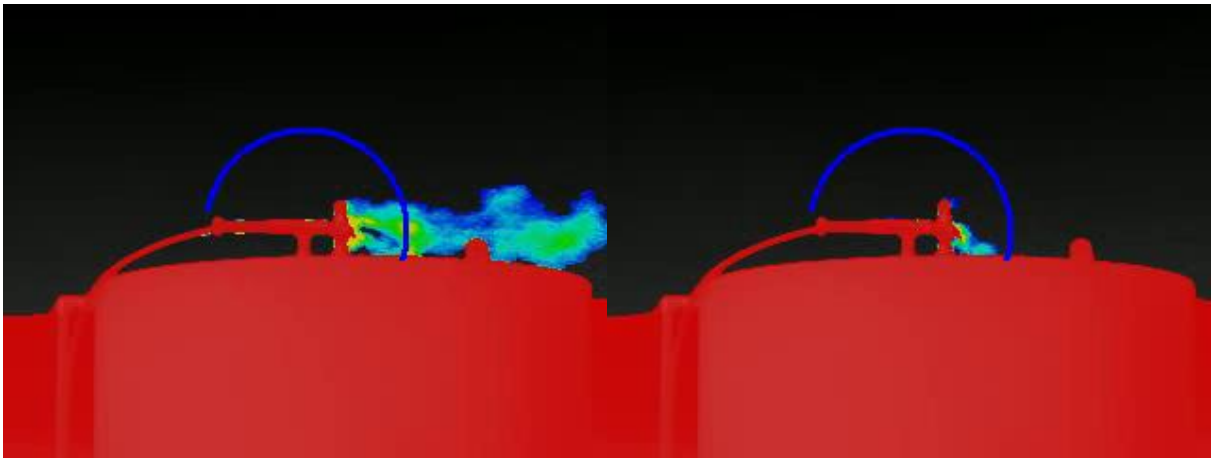

Figure 41: QL320 measurement #41 which was a downwind tank release. Snapshots showing (left) ideal wind direction and plume dispersion, and (right) challenging wind direction and plume dispersion.

3.3 Truck-based tunable-diode laser absorption spectroscopy

3.3.1 Summary of results

Figure 42 summarizes the performance of the truck-based TDLAS system. Overall, the technology had an average absolute error of 105%, with an average bias of +26%. Figure 42 also shows a potential outlier; excluding this datapoint, the average absolute error and bias of the technology were 73% and -7% respectively.

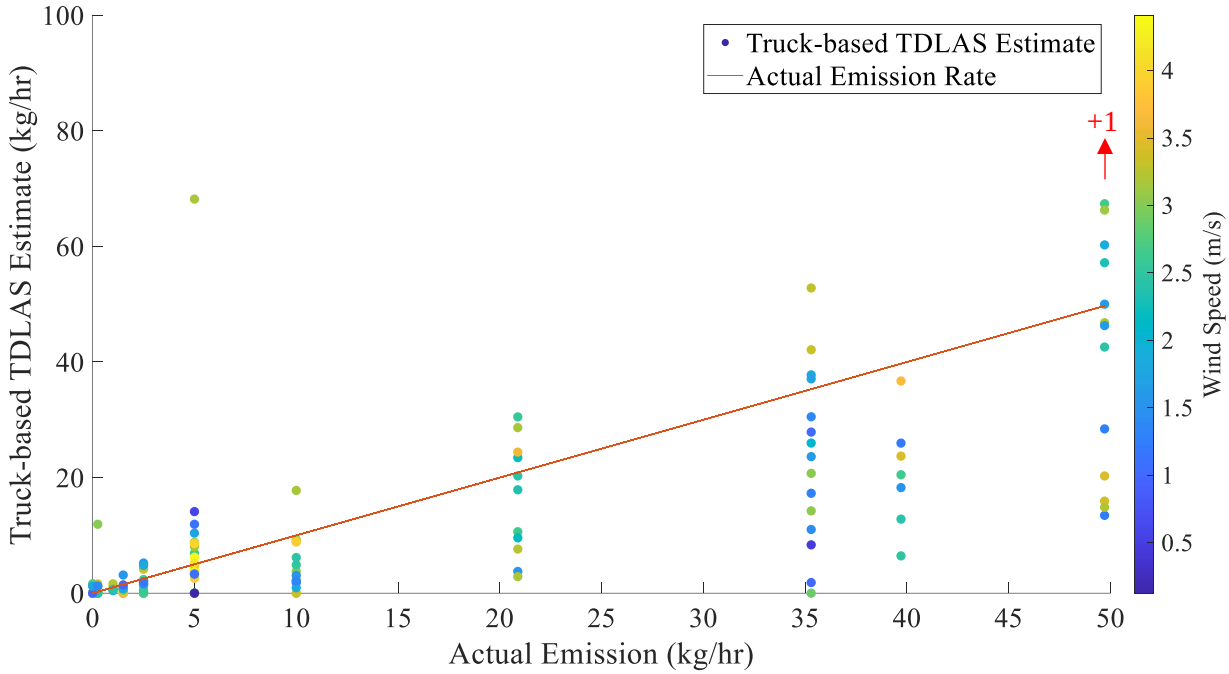

Figure 42: Summary of results for truck-based TDLAS emission estimates

3.3.2 Effect of wind speed

The truck-based results are plotted against windspeed in Figure 43. There is no clear trend between wind speed and error. The error was fairly skewed towards negative bias.

As noted in Sec. 2.2.3, the truck-based mass flow estimates are outcomes of the BLS dispersion model, which depend on wind speed but also on wind direction. During the TDLAS truck measurement, the operator reported that the plume was difficult to localize when the wind changed significantly during transects. Based on this observation, we hypothesize that the estimates inferred using the BLS algorithm should be sensitive not only to the wind speed, but variations in wind conditions during a transect.

Figure 44 plots the error of the estimates with respect to wind direction variability for the three days of TDLAS measurement. Wind direction variability is defined as the angle (in degrees) between the minimum and maximum wind directions measured over a 10 s period by the portable ultrasonic anemometer. In Figure 44, the x-axis corresponds to an average of the wind direction variability over the measurement time for each estimate, which is roughly 4 minutes depending on the length of the plume transect. At this point there is no clear trend between the estimate errors and the wind direction variability. On September 27, the errors corresponding to a wind direction variability below 35° are all lower than 50%. This could indicate that for lower wind direction variability the estimate errors are lower, however for higher angles some of the errors are also lower than 50%. This result is counterintuitive, since the advection model used to infer the release rate assumes a constant wind during the concentration measurements. Further research is needed to investigate how wind gusts, veering, and backing during a measurement may impact quantification accuracy.

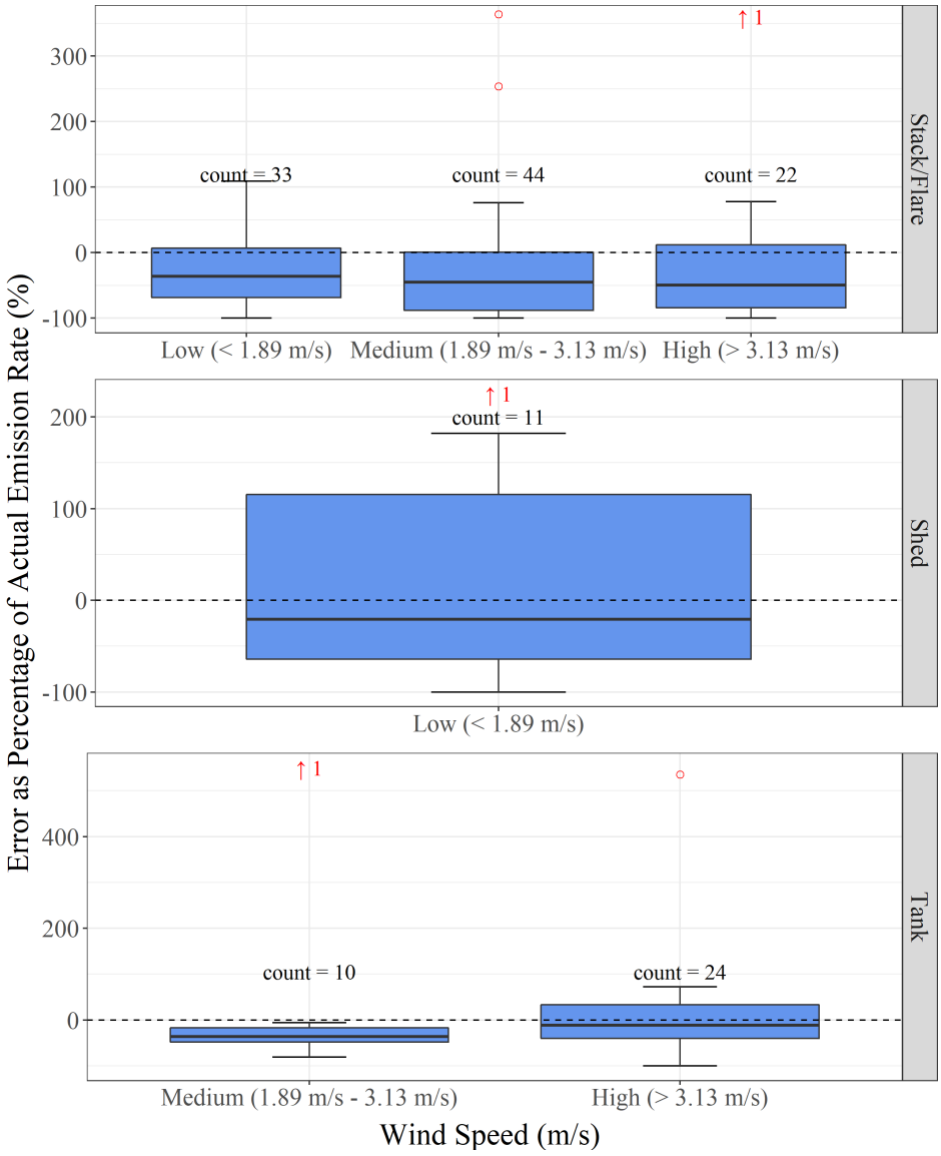

Figure 43: Truck-based TDLAS error (%) for different wind speeds

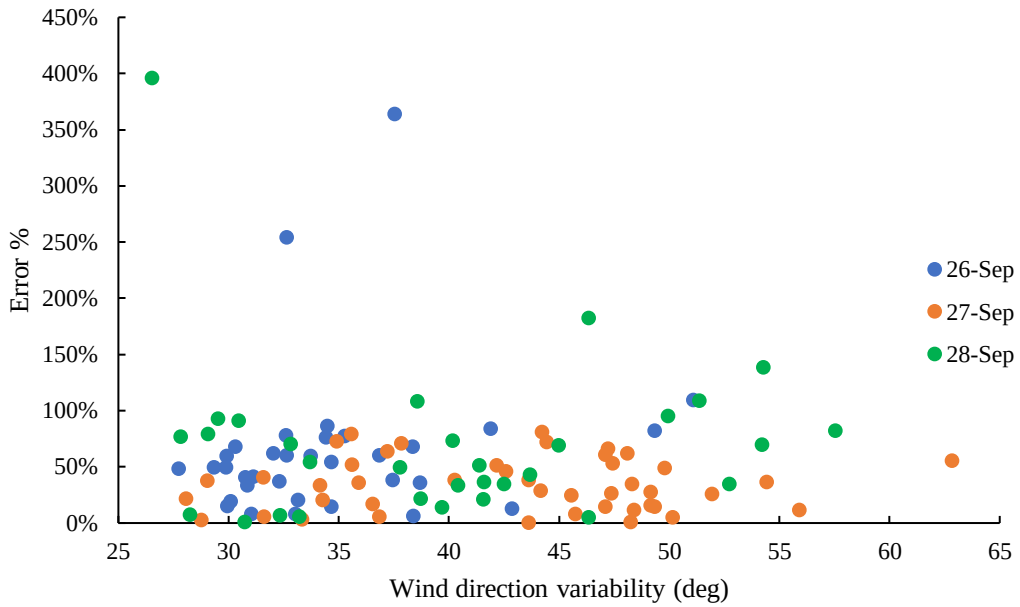

Figure 44: Truck-based TDLAS error (%) with respect to wind direction variability (deg)

3.3.3 Effect of emission rate

Figure 45 shows the errors of the truck-based TDLAS with respect to emission rate. As the emission rate decreases, the quantification error increases. Furthermore, with lower emission rates, the bias trends more negatively, indicating that the lower measurements may be operating at or near the technology's minimum detection limit (MDL). There is also a more significant effect on tank estimates for emission rate compared to windspeed. This could indicate that for these types of emissions the emission rate is a more important contributor to uncertainty than windspeed.

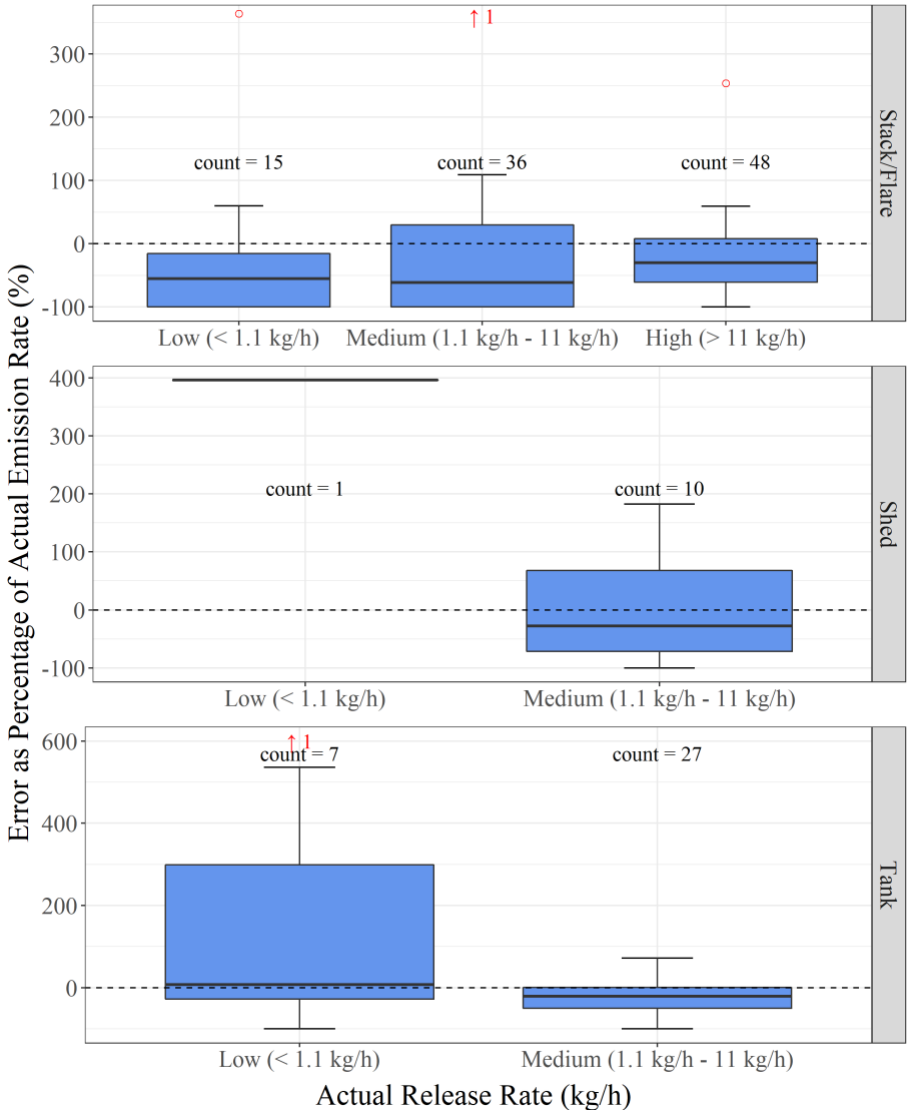

Figure 45: Truck-based TDLAS error (%) for different actual release rates.

3.3.4 Effect of release scenario

Figure 43 and Figure 45 show that quantification error is influenced significantly by the emission type; estimates of stack and flare emissions were more accurate than those of shed and tank emissions. Tank and shed emissions had considerably more surrounding infrastructure that could have interfered with downwind dispersion of the plume, in turn affecting the ability of the truck to detect the plume and the validity of the simplifications used to derive the BLS model.

3.4 Airborne NIR HS Imaging

3.4.1 Summary plots and cloud cover

Figure 46 summarizes the performance of the airborne NIR HS imaging system. The estimates have an average absolute error of 62% and a consistent positive bias of +52% for 44 emission estimates. Figure 46 shows error bars based on the uncertainty estimates provided by GHGSat for the technology.

During the second field campaign, only 2 of 46 measurement passes were reported as "missed detections", contrasting with 32 out of 80 measurements conducted during the first campaign were missed detections. This is mainly due to the difference in cloud cover between field campaigns. During the April 2022 campaign cloud shadow caused quantification issues for the technology, while on September 25 the skies were almost entirely clear of cloud. Cloud cover is a key factor that limits the availability of this technology.

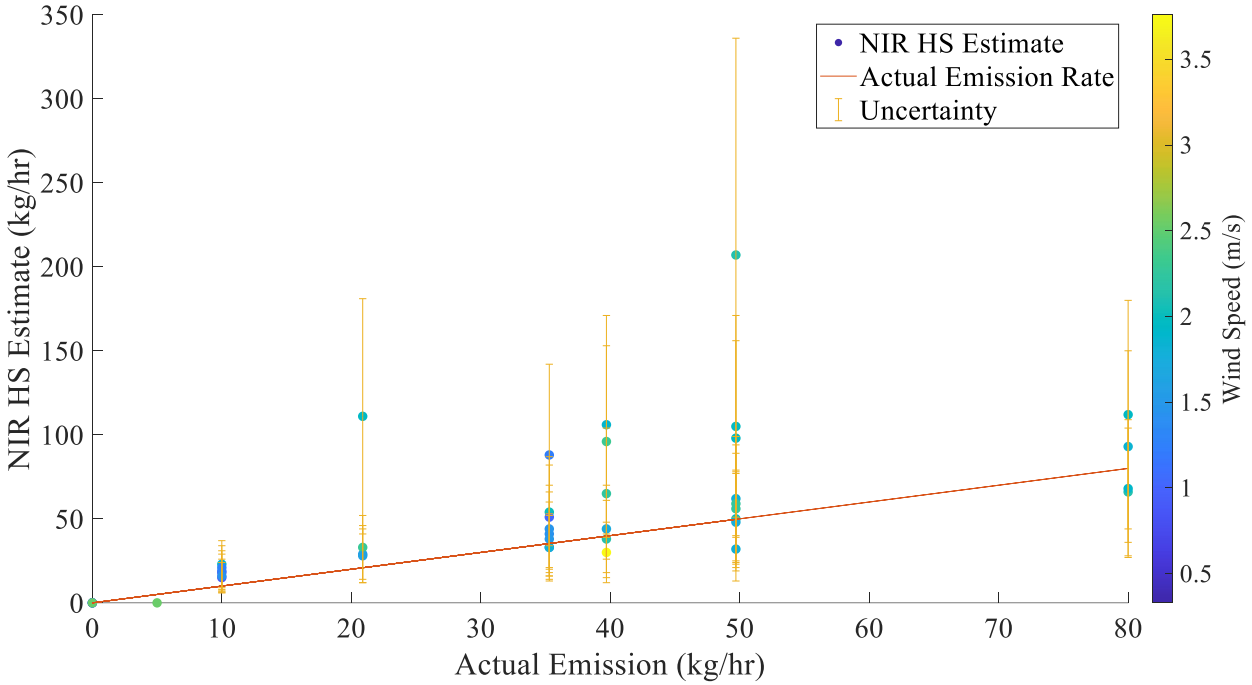

Figure 46: Summary of NIR HS imaging performance

3.4.2 Effect of wind speed

Figure 47 shows boxplots of the emission error for different windspeed measurements from the portable ultrasonic anemometer wind speed measurements. In general, error increases with wind speed, and the estimates have a positive bias. This could be for two reasons: first, increasing wind speed leads to a more disperse plume, which may result in regions of the 2D column density image that are below the detection threshold of the instrument. In this scenario one would expect the estimates to underpredict the true release rates, since areas of the plume are unaccounted for in the integration.

A second possibility is that the windspeed used to estimate the emission rate may be different than the true conditions. A key advantage of airborne systems is the ability to conduct measurements remotely, but with the drawback that a ground-based anemometry measurement is rarely available. Instead, providers must rely on wind speed models, e.g. from Meteoblue [23]. The wind speeds recorded by the provider are considerably higher than the windspeeds from the portable ultrasonic anemometer, on average reading 1.2 m/s higher. The wind speed error may be a significant contributor to uncertainty in estimates from airborne systems, and one would expect a linear

relationship based on wind speed error and emission error based on Eqs. (5) and (6). Johnson et al. observed a similar impact of wind inaccuracy in airborne TDLAS measurements [34].

Figure 48 shows a scatterplot of the absolute percent error ε versus the error in the wind speed, defined as the difference between the Meteoblue wind speed, u_{MB}, and the wind speed from the ultrasonic anemometer, u_{US}. To investigate if there is a linear relationship between wind speed error and error in the estimates, a linear regression model of the form

$$\varepsilon = \beta_0 + \beta_1 \left(u_{MB} - u_{US} \right) \tag{12}$$

was fit to the entire dataset. The resulting regression line is shown in blue in Figure 48. However, the presence of outlying points indicate that the statistical assumptions underlying the linear regression model may be violated. The two points which cause the most concern are indicated on the plot. It is unclear why these observations resulted in such high errors. Both observations occurred under relatively high wind speeds (according to the portable ultrasonic anemometer), so the high wind speeds may have contributed to the large errors. However, there were other observations taken at high wind speeds which do not have such large errors. A second linear regression model of the same form was fit to the dataset with the two outlying points removed and is shown in red. The statistical assumptions underlying the linear regression model are better satisfied in this case.

The parameter estimates and their associated standard errors are shown in Table 7. One important difference between the two models is in the magnitude of the standard errors. In the model with the outliers included, the standard errors are about twice as large as for the model without the outliers. Both models give similar estimates for β_1, the coefficient which quantifies the linear effect of wind error on absolute error. This indicates that the outliers do not have a big influence on the magnitude or direction of the linear effect.

Table 7 Parameter estimates and their standard errors for linear regression models of absolute error versus error in windspeed. Confidence interval(s) which indicate evidence of a linear effect of wind speed on absolute error are bolded.

Parameter	Estimate	Standard Error	95% Confidence Interval
Model with outliers, $\boldsymbol{\beta_0}$	24.38	28.66	(-33.9, 82.6)
Model with outliers, $\boldsymbol{\beta_1}$	36.90	20.46	(-4.7, 78.4)
Model without outliers, $\boldsymbol{\beta_0}$	12.34	13.86	(-15.9, 40.6)
Model without outliers, $\boldsymbol{\beta_1}$	32.31	9.90	(12.2, 52.5)

An important result is that the model without the outliers finds that there is significant evidence of a linear effect of wind error on absolute error, while the model with outliers finds no significant evidence of this effect. This can likely be attributed back to the size of the standard errors in the

two models. There is much greater variability in the data with the outliers included, so the linear effect cannot be estimated very precisely compared to the data with the outliers removed, leading to a wider range of plausible values for the parameter.

Finally, we investigate the strength of the linear relationship between wind error and absolute error by comparing the R^2, which measures the strength of the linear relationship between the variables. In the model with outliers included, the R^2 is 0.09, which means about 9% of the variation in the absolute error can be explained by the linear relationship with wind error. In the model with the outliers removed, the R^2 is 0.25, so 25% of the variation in absolute error is attributable to a linear relationship with wind error. Again, the differences between the models are likely due to the outliers increasing the variability in the data for the first model. Overall, we can conclude that the wind error appears to play a role in explaining the error in emission rate estimates, but the presence of extreme outliers and a relatively low R^2 suggest that there are more factors at play.

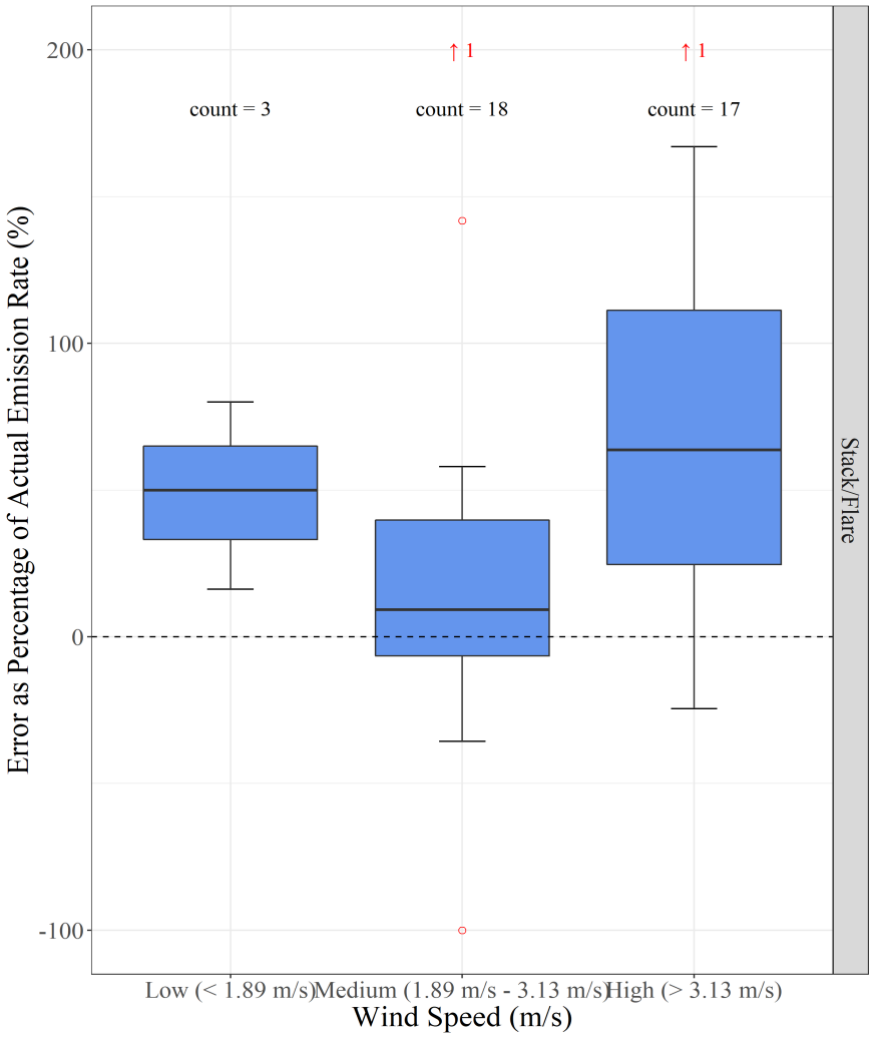

Figure 47: Airborne NIR HS imaging estimate error (%) with respect to windspeed from the portable ultrasonic anemometer.

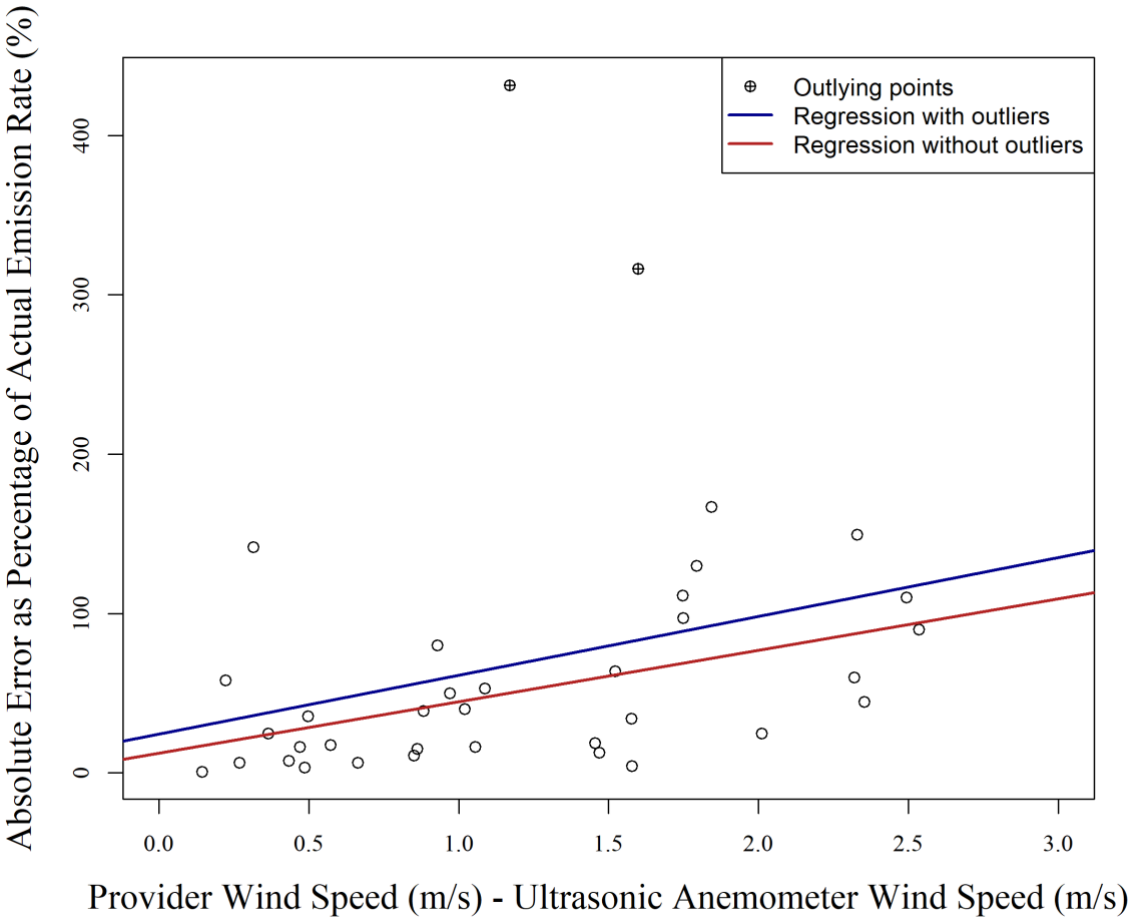

Figure 48: Airborne NIR HS imaging estimate error vs. the difference between the wind speed used by the provider and the in-situ wind speed measurements from the portable ultrasonic anemometer. Estimated linear regression lines fit with and without outlying points are overlaid.

3.4.3 Effect of emission rate

Figure 49 shows the relationship between emission rate and accuracy for estimates from the airborne NIR HS imaging system. Although the errors at high emission rates are significantly lower than at medium emission rates, far fewer releases were carried out at the medium emission rates. It possible that this result has more to do with the emission type than the actual release rate, as most of the "Medium" emission rates occurred on the short yellow stack, which had significantly more error than the tall flare stack, as discussed below.

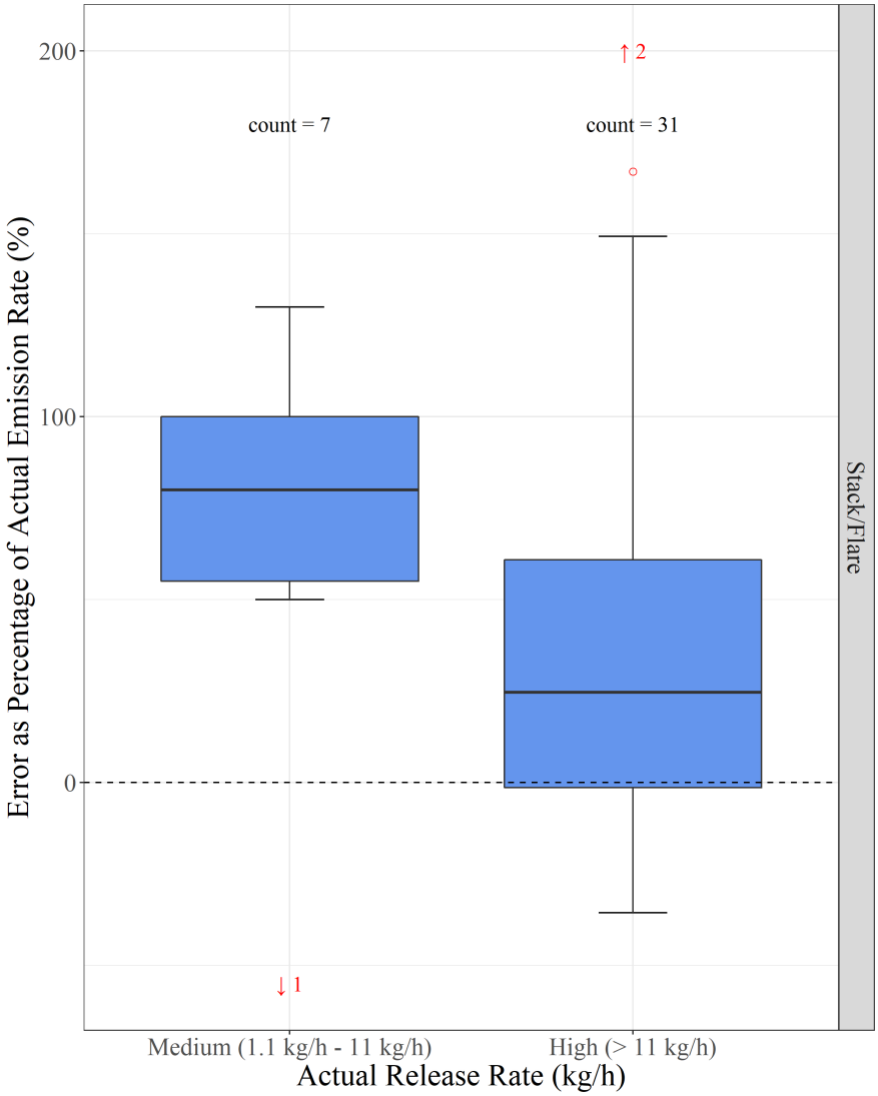

Figure 49: Airborne NIR HS error (%) for different actual release rates.

3.4.4 Effect of release scenario

Airborne NIR HS measurements were carried out on releases from the 13 m tall unlit flare and the 1.7 m short stack. These results are summarized in Table 8. Overall, the estimates on the short stack were significantly less accurate compared to those from the unlit flare. One potential reason for this is the impact of release type on how the plume disperses, with releases from the unlit flare dispersing over a wider area more quickly than for the short stack. It is possible that this led to spatial resolution issues when measuring the short stack, however more investigation is required to assess this possibility.

Table 8: Summary of airborne NIR performance vs release type.

Release Type	Average Absolute Error	Average Bias
1.7m Stack	100%	+100%
13m Flare	37%	+15%

3.5 Airborne LWIR HS imaging

3.5.1 Summary of results and data collection issues

Figure 50 summarizes emission estimates from the airborne LWIR HS system. Far fewer measurements were reported for this technology compared to the other systems. This is for two reasons: First, data from measurements carried out on October 2nd were deleted inadvertently by the provider. A second issue was caused by a tracking feature needed to focus the camera, which was set incorrectly for the majority of measurements. Consequently, only 26 estimates of 30 releases were reported on September 30th, and only two estimates of 39 releases were reported for October 1st. The average absolute error for the technology was 574% across 26 emission estimates. Figure 50 shows that this technology systematically overestimates the true emission rate.

Unfortunately, the environmental conditions for measurements were marginal on September 30th (chiefly due to poor thermal contrast between the air and the ground), while those on October 1st were nearly ideal. The technology provider shared an algorithm with the UW team that predicts the MDL based on air temperature, ground temperature, wind speed, and relative humidity. This tool is an important attribute to the cost-effectiveness of the measurement system, since it may be used to determine under which conditions measurements should be attempted, or when a survey should be aborted.

It should be remarked that this technology is the least mature of those evaluated in this project. The second field trial represents one of the first deployments of this technology, and consequently some "teething problems" are to be expected. Our understanding is that many of the issues that affected deployment have since been resolved by the technology provider.

3.5.2 Quantification technique

The primary reason for systematic overestimation of the true release rate is not inherent to the measurement, but rather lies in how the technology provider extracted an emission estimate from the wind speed and 2D column density map. Figure 51 shows an example 2D column density map, found from the LWIR data cube by inverting a spectroscopic model for each pixel.

The provider identified the highest column density (indicated on Figure 51), which was combined with a plume width and velocity to obtain an emission rate; this conceptually similar to the cross-section method, Eq. (6). However, in the cross-section method multiple plume transects are computed and averaged, so choosing only one transect that has the highest column density will bias the inferred emission rate strongly. The UW team is currently reanalyzing the column density maps using the techniques summarized in Sec. 1.2.2, and will revise the emission rate estimates accordingly.

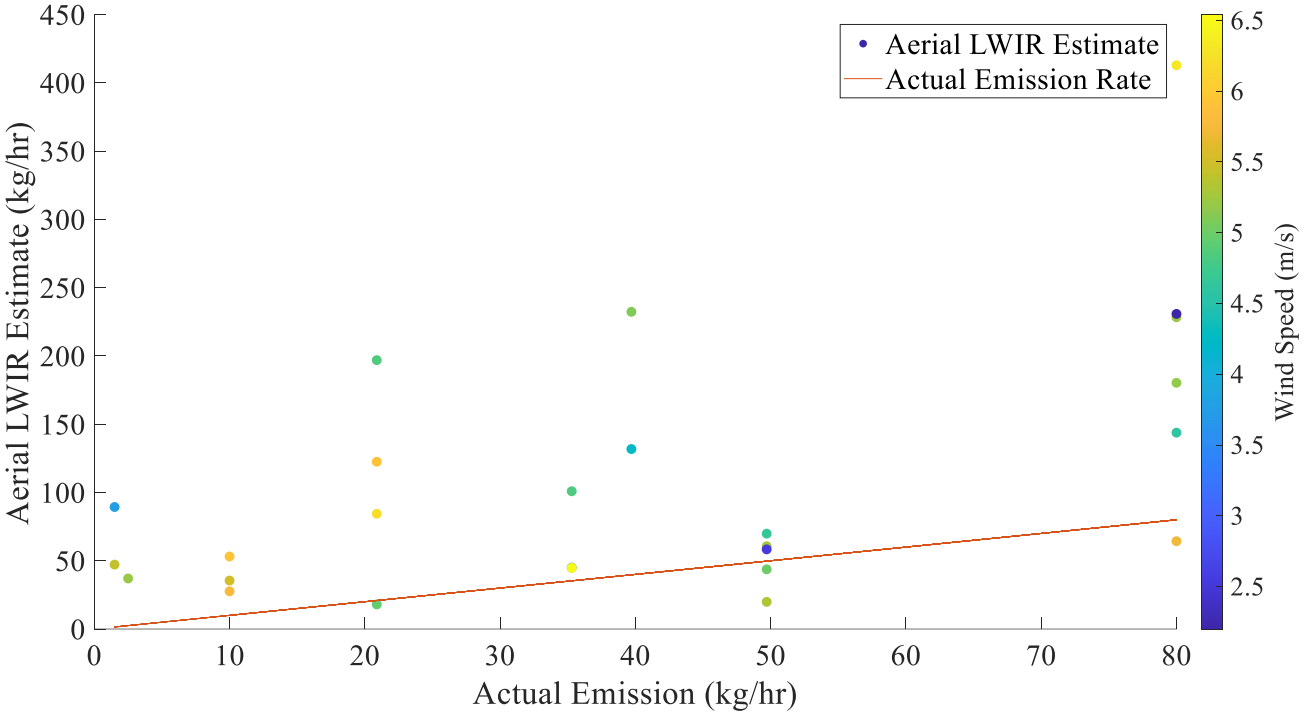

Figure 50: Summary of results for aerial LWIR hyperspectral estimates

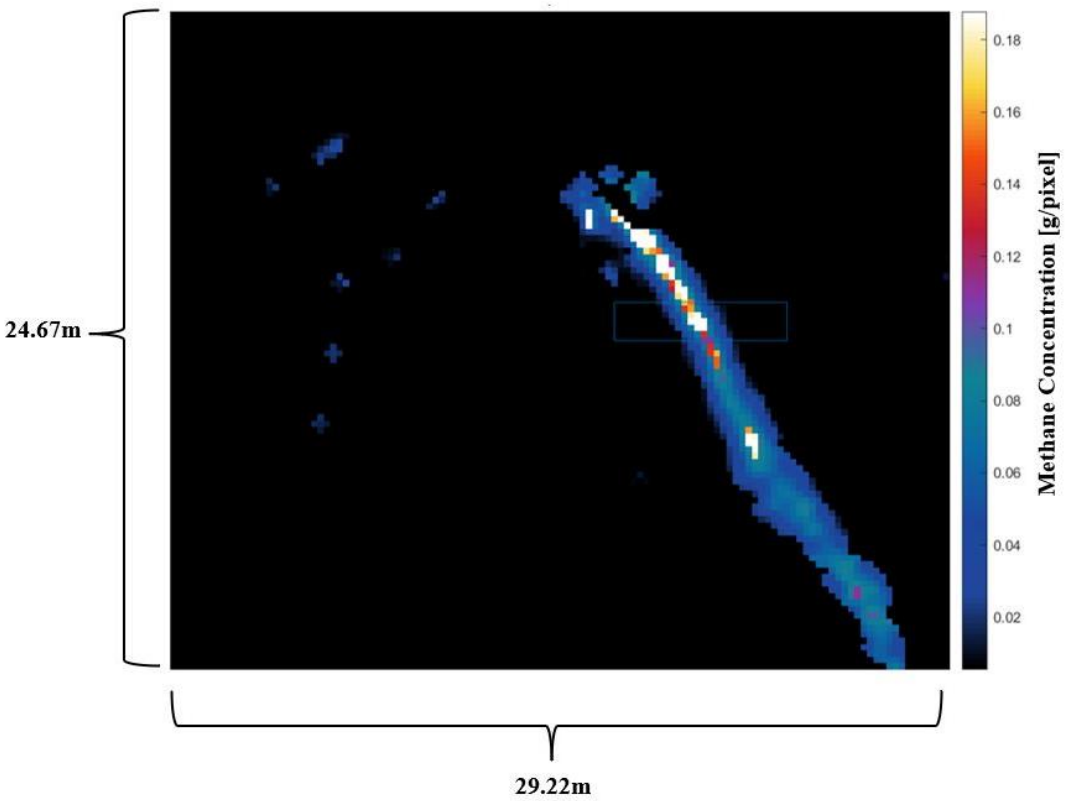

Figure 51: Example of airborne LWIR hyperspectral mass mapping for quantification.

4.0 PHASE 2A: AROFEMP MODELLING

As discussed in Section 1.3.1, Arolytics personnel used Arolytics' proprietary AroFEMP simulation code to predict the performance of three technologies identified in Phase 1 (two of which were evaluated during the field campaign) as if they were incorporated into an alternative FEMP (alt-FEMP) program. This procedure considered various scenarios to assess each technology's ability to detect and quantify methane emissions and subsequently influence leak repairs over a calendar year. The overall benefit of a given technology, in terms of the reduction in emissions (e.g., kg/year), was evaluated through a Monte Carlo simulation. Emission scenarios were sampled randomly from probability densities representative of operational conditions, and emission detection and quantification probabilities were derived from either manufacturer-specific details for a technology or previous field trials identified in Phase 1. Repeating this procedure multiple times amounted to an integration over the probability densities, with the outcome of the expected reduction in emissions.

Representative fugitive emissions probability profiles were derived from the FEMP-EA study's dataset [14]. Modelling was performed using an anonymous set of infrastructure, drawn from the Petrinex database, representing a typical Alberta upstream oil and gas producer. The criteria used to select the representative infrastructure were facility count, facility subtype distribution, and the ratio of facilities requiring triannual (3x) and annual (1x) surveys (per AER Directive 060 Table 4 [15]). A subset of 562 facilities was then chosen such that each of the criteria were equivalent to those of Petrinex's Alberta infrastructure. The FEMPs were modelled for a two-year timespan, as this is the typical length of an alt-FEMP.

The four technologies that were modelled are: airborne light detecting and ranging (LiDAR) (Bridger Photonics), airborne NIR hyperspectral imaging (GHGSat), truck mounted TDLAS (Boreal Laser), and QOGI using the FLIR GF320/QL320 system. QOGI survey time was derived from general time estimates from Canadian QOGI service providers and the QOGI detection capabilities were derived from Zimmerle et al. (2020) [16]. The detection capabilities and time information for the remaining technologies were obtained from each of the service providers.

The QOGI system was modelled as conducting the default FEMP [15] and the remaining technologies were modelled each in their own alt-FEMP. The frequency of screenings and the fraction of all facilities that received follow-up surveys were adjusted to design alt-FEMPs that were equivalent to or better than the default FEMP in fugitive emissions reductions.

The model results showed that all three alternative technologies could be used to design alt-FEMPs that are equivalent or superior to the default FEMP. These alt-FEMPs employed 2-3 screening surveys each year with OGI follow-ups being conducted at 30% of all screened facilities, selecting those with the largest emissions. The alt-FEMP design and performance details are as follows: airborne LiDAR technology, two screenings each year, 30% follow-up, 8% reduction in total fugitive emissions; airborne NIR hyperspectral imaging technology, three screenings each year, 30% follow-up, 11% reduction in total fugitive emissions; truck mounted TDLAS technology, three screenings each year, 30% follow-up, 15% reduction in total fugitive emissions. The reductions in total fugitive emissions are relative to the total fugitive emissions estimated by the model for the default FEMP.

This demonstrates that the airborne LiDAR, airborne NIR hyperspectral imaging, and truck-mounted TDLAS technologies can all be feasibly and practically employed as the screening technologies in alt-FEMPs that achieve fugitive emission reductions equivalent to a default FEMP

for a “typical” Alberta oil and gas producer. In this modelling, each of the alt-FEMPs was able to perform better than the default FEMP, indicating that the alt-FEMPs could potentially achieve fugitive emissions reductions equivalent to the default FEMP using less follow-up or fewer screenings than were modelled.

It is important to note that while this modelling was conducted for a “typical” Alberta oil and gas producer, the infrastructure of a given oil and gas producer and the properties of that infrastructure can vary considerably between producers. In addition, each alternative technology has unique capabilities which make it best suited to particular types of infrastructure and particular properties. Since the infrastructure and its properties can greatly affect the practicality and feasibility of employing an alt-FEMP and a particular alternative technology, the potential for successful implementation of an alt-FEMP is case dependent and should be evaluated for each unique scenario.

5.0 UNCERTAINTY QUANTIFICATION

Almost all of the technologies surveyed in this project provide a single "point estimate" of the emission rate, by combining a point concentration or column density estimate with an advection model. These estimates can only be interpreted correctly if their uncertainty is known. For example, oil and gas producers need to know the uncertainty of an emissions estimate to determine the most cost-effective mitigation strategy; regulators need to understand the probability that an operator is complying with emissions regulations; while environmental scientists need to understand uncertainty in emission inventories when developing policy. Accordingly, a key focus of this project is to develop techniques for quantifying the uncertainty attached to these emission estimates.

5.1 Bayesian analysis framework

Data collected during the first and second field campaigns highlights how parameters such as the true emission rate, wind speed, and emission scenario may influence the estimated emission rate. Our goal is to explain the bias (the difference between the estimated emission rate and the actual emission rate, on average) and the uncertainty (the expected variability in the estimated emission rate in repeated measurements under the same conditions) of these measurements and understand how bias and uncertainty are impacted by the parameters. We will accomplish these goals using a Bayesian statistical analysis.

Bayesian statistical analysis allows us to consider different sources of bias and uncertainty. These sources may be categorized as: (1) errors in the observed data, such as an incorrect concentration measurement (due to instrument error or noise) or inaccurate wind speed, e.g., due to using Meteoblue, or; (2) errors in the measurement model. The measurement model connects the emission rate to the observed data (concentration, background temperature, etc.); it may be based on physics, such as the Gaussian plume model, or be empirical in nature (e.g., a neural network). By necessity, the measurement model is a simplification of the true problem physics, and consequently even if there are no errors in the observed data, the modeled release rate will differ from the true release rate by a small factor.

In Bayesian analysis, the QoI and statistical model parameters are treated as random variables which follow probability density functions (PDFs); the PDFs define what is known about the parameter in question, and the PDF widths reflect the uncertainty. Let Q denote the quantity-of-interest (QoI), the actual emission rate. Let Q^m denote the estimated emission rate, $\boldsymbol{\rho}$ denote the vector of raw data (such as concentration) used to determine the estimated emission rate, and $\boldsymbol{\varphi}$ be a vector of additional observed data which may or may not be involved in determining Q^m, such as the wind speed and background temperature. We will let $\mathbf{x} = (Q^m, \boldsymbol{\rho}, \boldsymbol{\varphi})$ be the vector containing the additional data that is not the quantity of interest, Q. The data from our field trial comprises $(Q, Q^m, \boldsymbol{\rho}, \boldsymbol{\varphi})$. Finally, let $\boldsymbol{\xi}$ denote a vector of unknown model parameters which describe the bias and uncertainty of Q^m.

Our goal is to determine the probability distribution of the model parameters $\boldsymbol{\xi}$ given the field trial data. This is called the *posterior distribution*, denoted $p(\boldsymbol{\xi}|\, Q, \mathbf{x})$. Bayes' theorem describes the fundamental relationships between the probability densities of the observed data and model parameters and shows how to get the posterior distribution:

$$p\left(\boldsymbol{\xi}|Q,\mathbf{x}\right)=\frac{p\left(\boldsymbol{\xi}\right)p\left(Q|\boldsymbol{\xi},\mathbf{x}\right)}{p\left(Q\right)} \tag{13}$$

Here, $p(\xi)$ is called the *prior distribution*, which describes what is known about ξ before observing the data. The *likelihood function* $p(Q|\boldsymbol{\xi}, \mathbf{x})$ describes the probability density of the quantity of interest given the parameters and additional data, and the *evidence*,

$$p(Q) = \int_{\xi} p(\xi)\, p(Q|\xi, \mathbf{x})\, d\xi \tag{14}$$

serves to normalize the numerator in Eq. (13) so the posterior PDF satisfies the Law of Total Probability.

Another important probability density that can be obtained in a Bayesian analysis is the posterior predictive distribution,

$$p\left(Q^{\text{new}} \middle| \mathbf{x}^{\text{new}}, Q, \mathbf{x}\right) = \int_{\xi} p(\xi|Q, \mathbf{x})\, p\left(Q^{\text{new}} \middle| \xi, \mathbf{x}^{\text{new}}\right) d\xi \tag{15}$$

This procedure allows the posterior PDF of the actual emission rate for a new observation, Q^{new}, to be derived given a new observation $\mathbf{x}^{\text{new}}$ and the previously observed data, Q. That is, if a provider makes a measurement, or in other words, observes particular values $\mathbf{x}^{\text{new}} = (Q^{\text{m,new}}, \boldsymbol{\rho}^{\text{new}}, \boldsymbol{\varphi}^{\text{new}})$, the posterior predictive distribution $p(Q^{\text{new}}|\mathbf{x}^{\text{new}}, Q, \mathbf{x})$ is the probability distribution of the true emission rate given $\mathbf{x}^{\text{new}}$ and the data from the field trial. The posterior predictive distribution incorporates uncertainty in the model parameters and the variability observed in the field trial data, therefore painting a full picture of the uncertainty associated with predicting a true emission rate given a measurement $\mathbf{x}^{\text{new}}$.

5.1.1 Likelihoods

Specifying the likelihood of Q is an important step in the model. We can explore different likelihoods by specifying the mean and the variance and then using different distributions with different shapes to find what gives the best model fit. The normal distribution is a classic starting point, and can be changed to a different distribution if the fit is poor. That is, the likelihood is $Q \sim N(\mu(\mathbf{x}), \Sigma(\mathbf{x}))$. The form of the mean, $\mu(\mathbf{x})$, and the covariance matrix, $\Sigma(\mathbf{x})$, are discussed below.

Two broad approaches to specifying the mean can be used, depending on whether or not the functional form of the measurement model is available. Let $m(\boldsymbol{\rho}, \boldsymbol{\varphi})$ be the measurement model, that is, the function which a provider uses to transform the raw data and auxiliary data into the estimated emission rate Q^{m}. We have $m(\boldsymbol{\rho}, \boldsymbol{\varphi}) = Q^{\text{m}}$. If m is known, we can model the mean as

$$\mu(\mathbf{x}) = \beta_0 + \beta_1 m(\boldsymbol{\rho}, \boldsymbol{\varphi}) \tag{16}$$

where β_0 and β_1 are parameters to be estimated: β_0 is the expected actual emission rate when the measured emission rate is 0, and β_1 is the expected increase in actual emission rate for every one unit increase in the measured emission rate. Therefore, a perfectly unbiased measurement model (with no errors in the observations) would have $\beta_0 = 0$ and $\beta_1 = 1$.

The advantage of using the known measurement model is that it reflects the underlying physical processes. This will become important once errors in $\boldsymbol{\varphi}$ are included in the model (see Section 5.1.2).

On the other hand, if the measurement model is not known, the variables in $\boldsymbol{\varphi}$ are not included in the model, although they may help predict the technology's performance. In this case, these variables can be included in the linear model:

$$\mu(\mathbf{x}) = \beta_0 + \beta_1 Q^{\mathrm{m}} + \sum_{k=1}^{p} \beta_{k+1} \varphi_k, \tag{17}$$

where φ_k is the kth element in $\boldsymbol{\varphi}$. This allows $\boldsymbol{\varphi}$ to play a role in the mean of the quantity of interest and also to incorporate the effect of errors in $\boldsymbol{\varphi}$ without knowing the measurement model used by the technology provider.

From the scatterplots of the estimated versus actual emission rates, it appears that the variability increases for larger values of Q and Q^{m}. Therefore, we will scale the variance by the mean of Q. That is, we model the variance as $[\mu(\mathbf{x})]^{2\alpha}\sigma^2$ where $0 \leq \alpha \leq 1$, reflecting the fact that larger measurements tend to have more variability, and σ^2 is non-negative and quantifies the variance.

5.1.2 Errors in observations

So far, we have not considered the possibility of error in $\boldsymbol{\varphi}$. This can be incorporated into the mean models using a latent variable approach in which introduce new variables φ_k^* are used to represent the true values of these variables in the absence of error. For example, φ_k might be the wind speed reported by Meteoblue, and φ_k^* would be the wind speed at the source at the time of the measurement, which is unknown but can be modelled. The observed values of φ_k can be written as $\varphi_k = \varphi_k^* + \epsilon_k$ where φ_k^* is the error-free measurement and ϵ_k is the measurement error. Then we assume that $\epsilon_k \sim \mathrm{N}(0, \tau_k^2)$ that is, the measurement error is normally distributed around zero with unknown variance, τ_k^2.

5.1.3 Prior specification

Prior distributions must be specified for $\beta_0, \ldots, \beta_{k+1}$, α, and σ^2. If measurement error is included, priors must also be placed on τ_k^2, $k = 1, \ldots, p$. The prior distributions reflect our beliefs about these parameters before considering the observed data. For example, σ^2 is a variance parameter, so we would use a prior distribution with non-negative support.

5.1.4 Computation and Inference

Due to the complexity and generality of the models which will be fit during the Bayesian analysis, a closed form solution to Bayes' theorem will not be available. Thus, we will use Markov Chain Monte Carlo (MCMC) to simulate the posterior distributions and the posterior predictive distributions. MCMC draws values of the parameter vector $\boldsymbol{\xi} = (\beta_0, \ldots, \beta_{k+1}, \alpha, \sigma^2, \tau_1^2, \ldots \tau_p^2)$ from a distribution which eventually converges to the posterior distribution. The computation required for MCMC can be carried out using JAGS (Just Another Gibbs Sampler) [35]. Inference can be carried out using the resulting MCMC samples. Credible intervals for quantities of interest can be constructed from the posterior distribution to give regions which have a 95% probability of containing the true parameter value.

6.0 CONCLUSIONS AND FUTURE WORK

6.1 Key findings

6.1.1 Preliminary results from the second field campaign

The second field campaign focused on the performance of four technologies, operated by five providers: QOGI, truck-based TDLAS, and airborne NIR and LWIR HS imaging. In general, the truck-based TDLAS system provided the most robust emission estimates, followed by QOGI, airborne NIR HS imaging, and airborne LWIR HS imaging.

Emission estimates were sensitive to emission rates, release scenarios, and environmental conditions. In general, the QOGI systems provided the most robust estimates, followed by the airborne NIR system and the truck based TDLAS system, and finally the LWIR HS systems. The truck-based TDLAS system and QOGI were most accurate when estimating releases from the stack and unlit flare, and less accurate for emissions from structures. A detailed analysis of the QOGI data revealed how factors including measurement distance, wind speed, release rate, background cloud cover, thermal contrast, background reflection, and, potentially, operator experience may impact the emissions accuracy. In some cases, it is difficult to determine the impact of each factor conclusively since advection model is a proprietary and confidential aspect of the measurement system, and some aspects of the system involve heuristically-set parameters that may introduce bias in the estimates.

Estimates from the airborne NIR HS imaging system made during the second field campaign were considerably more accurate compared to the first field campaign, which was attributed to clearer skies during the second field campaign. The accuracy of these estimates was also affected by release height, with the releases from the unlit flare estimated more accurately than those from the stack closer to the ground. Estimation accuracy also relies on the windspeed used to convert the 2D column density map found using the spectroscopic model into an emission estimate; a statistical analysis shows a linear correlation between the accuracy and the difference between the modeled windspeed used by the provider to process the data and the windspeed measured using an ultrasonic anemometer.

Estimates obtained using the airborne LWIR HS imaging system were the least accurate, and this system had a large number of missed detections due to issues with the instrument setting and data handling on the part of the provider. Furthermore, the 2D column density maps were processed in a manner that produced a large positive bias in the estimates.

Care should be taken when comparing these technologies, since each has their own application and relies on different levels of information. For example, the truck-based TDLAS system and QOGI systems relied on knowledge of the leak location, while the airborne HS systems could be used to survey a much larger area. The truck-based TDLAS system estimate incorporates a wind measurement obtained from a peripheral ultrasonic anemometer, while the airborne HS imaging techniques are constrained to use wind speeds from less reliable sources. The QOGI systems do not require wind speed as an input, since plume advection is inferred from feature tracing between successive images.

6.1.2 AroFEMP Modelling

As described in Section 4.0, the model results revealed that alt-FEMPs equivalent or superior to the default FEMP were successfully designed for all three alternative technologies (technologies other than OGI). These alt-FEMPs employed 2-3 screening surveys each year with OGI follow-

ups being conducted at 30% of all screened facilities, selecting those with the largest emissions. This demonstrates that the airborne LiDAR, airborne NIR hyperspectral imaging, and truck-mounted TDLAS technologies can all be feasibly and practically employed as the screening technologies in alt-FEMPs that achieve fugitive emission reductions equivalent to a default FEMP for a "typical" Alberta oil and gas producer. In this modelling, each of the alt-FEMPs was able to perform better than the default FEMP, indicating that the alt-FEMPs could potentially achieve fugitive emissions reductions equivalent to the default FEMP using less follow-up or fewer screenings than were modelled.

It is important to note that while this modelling was conducted for a "typical" Alberta oil and gas producer, the infrastructure of a given oil and gas producer and the properties of that infrastructure can vary considerably between producers. In addition, each alternative technology has unique capabilities which make it best suited to particular types of infrastructure and particular properties. Since the infrastructure and its properties can greatly affect the practicality and feasibility of employing an alt-FEMP and a particular alternative technology, the potential for successful implementation of an alt-FEMP is case dependent and should be evaluated for each unique scenario.

6.2 Ongoing and future work

The following activities are currently underway, or will commence before the end of the project in December 2023.

6.2.1 Aerial LWIR HS imaging

The UW team will investigate alternative techniques including the IME method and cross-sectional flux method used for the NIR measurement quantification, described in Section 1.2.2. In view of the limited amount of data collected during the second field campaign, additional field measurements are required. These activities will be funded by the provider or through an alternative funding source.

6.2.2 Truck-based TDLAS

The provider calculated emission estimates using the backwards Lagrangian stochastic technique. The UW team will derive a second set of emission estimates using the simpler inverse gaussian modelling (IGM) analysis, as was the case from the first field trial data. The UW team will also investigate how accuracy is impacted by wind-direction variability, as well as distance from the source location. This work will help form the basis of future uncertainty analysis involving Bayesian analysis.

6.2.3 Availability of technologies

The outcomes of the first and second field campaigns highlight that quantification accuracy depends strongly on environmental factors, and, under some conditions, it may be impossible to obtain a reliable emission estimate for a given technology. The UW team will work on developing a metric to assess the availability of each technology, based on the fraction of time the technology may be considered deployable for a given location (taken to be Brooks, AB) over the calendar year. This endeavor will be based on historical climate data, manufacture-specified operating limits, data from the field campaigns, and the MDL calculator shared by the airborne LWIR HS imaging provider.

6.2.4 Uncertainty analysis

Finally, the UW team are developing a generic Bayesian framework for estimating the accuracy and bias in emission estimates. The UW team will initially focus on truck-based TDLAS, since the instrument model that connects the concentration measurements to emission rates is well defined. The analysis will consider how uncertainty in the concentration measurements, environmental parameters (e.g., wind) and approximations in the measurement model propagate into a PDF of the emission rate.

REFERENCES

[1] *Canadian Environmental Protection Act (CEPA) S.C. 1999, c. 33.*

[2] Environment and Climate Change Canada, "A healthy environment and a healthy economy: Canada's strengthened climate plan to create jobs and support people, communities, and the planet," ECCC, Ottawa, 2020.

[3] Environment and Climate Change Canada, "Review of Canada's Methane Regulations for the Upstream Oil and Gas Sector," ECCC, Ottawa, 2021.

[4] D. R. Caulton, Q. Li, E. Bou-Zeid, J. P. Fitt, L. M. Golston, D. Pan, J. Lu, H. M. Lane, B. Buchholz, X. Guo, J. McSpiritt, L. Wendt and M. A. Zondlo, "Quantifying uncertainties from mobile-laboratory-derived emissions of well pads using inverse Gaussian methods," *Atmos. Chem. Phys.*, 18 (2018) 15145.

[5] B. Kura and A. Jilla, "Feasibility of the inverse-dispersion model for quantifying drydock emissions," *Atmosphere,* 10 (2019) 328.

[6] B. Crenna, "An Introduction to WindTrax," Department of Earth and Atmospheric Science, the University of Alberta, Edmonton, 2006.

[7] C. B. Alden, S. C. Coburn, R. J. Wright, E. Baumann, K. Cossel, E. Perez, E. Hoenig, K. Prasad, I. Coddington and G. B. Reiker, "Single-blind quantification of natural gas leaks from 1 km distance using frequency combs," *Environ. Sci. Technol.,* 53 (2019) 2908.

[8] M. R. Johnson, D. R. Tyner and A. J. Szerkes, "Blinded evaluation of airborne methane source detection using Bridger Photonics LiDAR," *Remote Sens. Environ.,* 259 (2021) 112418.

[9] D. Hollenbeck, D. Zulevic and Y. Chen, "Advanced leak detection and quantification of methane emissions using sUAS," *Drones,* 5 (2021) 117.

[10] G. Durant, P.-Y. Foucher, S. Doz, X. Watremez, S. Jourdan, E. Vanneau and H. Pinot, "Test of SIMAGAZ: a LWIR cryogenic multispectral infrared camera for methane gas leak detection and quantification", *SPIE Volume 11727, Algorithms, Technologies, and Applications for Multispectral and Hyperspectral Imaging XXVII*, 2021.

[11] D. J. Varon, J. McKeever, D. Jervis, J. D. Maasakkers, S. Pandey, S. Houweling, A. I., T. Scarpelli and D. J. Jacob, "Satellite discovery of anomalously large methane point sources from oil/gas production," *Geophys. Res. Lett.*, 46 (2019) 13507.

[12] D. J. Varon, D. J. Jacob, J. McKeever, D. Jervis, B. O. A. Durak, Y. Xia and Y. Huang, "Quantifying methane point sources from fine-scale satellite observations of atmospheric methane plumes," *Atmos. Meas. Tech.,* 11 (2018) 5673.

[13] P. Tremblay, K. C. Gross, M. Chamberland, A. Villemaire and G. P. Perram, "Understanding and overcoming scene-change artifacts in imaging Fourier-transform spectroscopy of a turbulent jet engine exhaust," in *SPIE Optical Engineering and Applications*, San Diego CA, 2009.

[14] D. Risk, K. MacKay, M. Laboie and E. Bourlon, "Methane emissions data aggregation and analysis project for FEMP-EA and Canadian context: Resources, patterns, and measurement methodology performance," PTAC, Calgary, Alberta, 2019.

[15] Alberta Energy Regulator, "Directive 60: Upsteam Petroleum Industry Flaring, Incinerating, and Venting," AER, Calgary, 2022.

[16] D. Zimmerle, T. Vaughn, C. Bell, K. Bennett, P. Deshmukh and E. Thoma, "Detection limits of optical gas imaging for natural gas leak detection in realistic controlled conditions," *Environ. Sci. Technol.,* 54 (2020) 11506.

[17] B. Horn and B. G. Schunck, "Determining Optical Flow," *Artif. Intell., 17* (1981) 185.

[18] B. D. Lucas and T. Kanade, "An iterative image registration technique with an application to stereo vision," in *International Joint Conference on Artificial Intelligence*, Vancouver BC, 1981.

[19] Y. Zeng and J. Morris, Interviewees, *Virtual Meeting with Providence Photonics.* [Interview]. 19 December 2022.

[20] OpenCV, [Online]. Available: https://opencv.org/. [Accessed 25 January 2023].

[21] K. J. Daun, C. Lemieux, C. Beliveau, D. Blackmore, M. Nagorski, K.-M. Shim, P. Lapeyre, A. Wigle, J. J., K. Fritz and K. Osadetz, "Evaluation of Emission Quantification Technologies: Interim Report," University of Waterloo, Waterloo, 2022.

[22] United States Environmental Protection Agency, "Standards of performance for new, reconstructed, and modified sources and emissions guidelines for existing sources: Oil and gas sector climate review," *Fed. Reg.,* 86 (2021) 63310.

[23] Meteoblue, "History +," Meteoblue, 2023. [Online]. Available: https://www.meteoblue.com/en/historyplus.

[24] "FLIR GFx320 Specifications," FLIR, [Online]. Available: https://www.flir.com/products/gfx320/.

[25] "EyeCGas Specifications," Opgal, [Online]. Available: https://www.opgal.com/products/eyecgas/.

[26] Boreal Laser, "Instrument Data Sheet GasFinder3," 02 2016. [Online]. Available: https://boreal-laser.com/wp-content/uploads/2016/02/Instrument-Data-Sheet-GasFinder3-VB-010721.pdf. [Accessed 01 2023].

[27] A. P. Ravikumar, J. Wang, M. McGuire, C. S. Bell, D. Zimmerle and A. R. Brandt, "'Good versus good enough?' Empirical tests of methane leak detection sensitivity of a commercial infrared camera," *Environ. Sci. Technol.,* 52 (2018) 2368.

[28] Y. Zeng and J. Morris, "Detection limits of optical gas imagers as a function of temperature differential and distance," *J. Air Waste Manag. Assoc.,* 69 (2019) 351.

[29] L. Jackiw, "Verification of Quantitative Optical Gas Imaging System," Saskatchewan Research Council, 2018.

[30] Y. Zeng and J. Morris, "Calibration and Quantification Method for Gas Imaging Camera". United States of America Patent 9325915 B2, 26 April 2016.

[31] H. Abdel-Moati, J. Morris and Y. Zeng, "New Optical Gas Imaging Technology for Quantifying Fugitive Emission Rates," *Proc. International Petroleum Technology Conference*, Doha, 2015.

[32] "Top 10 Questions: Gas Leak Quantification with OGI Cameras," FLIR, 2020. [Online]. Available: https://www.flir.com/discover/instruments/gas-detection/top-10-questions-gas-leak-quantification-with-ogi-cameras/.

[33] C. Caico, L. Fragu, L. Gonzalez, C. Juéry, P. Kangas, C. Lawson, J. Negroni, P. Roberts, B. Smithers, P. Tupper and K. Vaskinen, "An evaluation of an optical gas imaging system for the quantification of fugitive hydrocarbon emissions," Concawe, Brussels, 2017.

[34] M. R. Johnson and D. R. Tyner, "Where the methane is- insights from novel airborne LiDAR measurements combined with ground survey data," *Environ. Sci. Technol.*, 55 (2021) 9773.

[35] S. Depaoli, J. P. Clifton and P. R. Cobb, "Just another Gibbs sampler (JAGS) flexible software for MCMC implementation," *J. Educ. Behav. Stat.*, 41 (2016) 628.

APPENDIX A: PHASE 1 SUMMARY

Table A.1: Summary of available methane quantification technologies

Technology	Survey Type	Detection Level	Concentration Dimension	Minimum Detection Limit (MDL)	Precision	Applicability	Limitations	Technology Readiness Level (TRL)
Ultraviolet Doppler Optical Absorption Spectroscopy	Fixed Location	Facility	Point Concentration (0D)	0.5-1 ppm-m	95%	LDAR programs (standalone or in combination with screening technologies)	Rain, snow, fog, and/or clouds reduce measurement abilities due to strong attenuation in the UV-Vis region.	9
OGI/QOGI Camera	Handheld	Component	Single Channel (1D)	0.44 m3/day	50-80%	LDAR programs (standalone or in combination with screening technologies)	Require a temperature difference between the emission plume and the local background (0.5 degrees to detect the gas; 3.0 degrees to quantify the mass flow rate). Must be between 1.5-4.6 m from the plume. Operating temperatures between -20 to +50 degrees Celsius.	7+
Dual Frequency Comb Spectroscopy	Fixed Location	Facility	Single Channel (1D)	2.10 m3/day	within 0.222 kg/hr with absolute deviation of 27%	LDAR programs (standalone or in combination with screening technologies)	Precipitation reduces signal path.	4-7

Airborne TDLAS (Bridger)	Aerial	Facility /Site	Imaging (2D)	29.22 m^3/day at 1 m/s wind 73.06 m^3/day at 3 m/s wind 21.92 m^3/day under ideal conditions	68%	Monitoring emissions from pipeline along ROW and remote/sparse arrangements of well sites. Screening technology for LDAR programs.	Standing water and snow absorb incident laser, leading to conservative emission estimates. Research is ongoing in developing a system that addresses this problem. Wind speed estimations limit accuracy of quantification (>3 m/s). A sufficient swath is required to meet the maximum efficiency of the technology. Drone applications are also less efficient than aircraft-mounted TDLAS.	9
Multispectral IR Camera	Handheld	Component	Imaging (2D)	13.211 m^3/day	1 K from -15°C to 150°C	LDAR programs (standalone or in combination with screening technologies)	Most MS cameras have warm filters, which disallows measurements of gases at near ambient temperatures. (MS cameras with cold filters are being developed.)	9

Spectrometry WAF-P (GHGSat)	Satellite	Facilities /Site	Imaging (2D)	36,529 m^3/day in 3 m/s wind speeds	13-60%	Monitoring emissions from pipeline along ROW and remote/sparse arrangements of well sites. Screening technology for LDAR programs.	Requires clear skies for observations; can revisit a site every 2 weeks.	7+
Hyperspectral IR Camera	Fixed Location	Component /Facility	Imaging (2D)	5.81 m^3/day (3.4 m distance) 10.34 m^3/day (5.9 m distance) at 4.5 m/s wind speed	up to 0.25 cm^{-1}	LDAR programs (standalone or in combination with screening technologies)	Operating temperatures between -20 and +40 degrees celsius. Sensitive to high wind speeds. Measurement distance must be within 100 m of the sources.	7+
Spectrometry TROPOMI	Satellite	Site	Imaging (2D)	153,424 m^3/day	0.60%	Monitoring emissions from pipeline along ROW and remote/sparse arrangements of well sites. Screening technology for LDAR programs.	Limited by the visibility of the atmosphere (i.e., cloud coverage). Solar zenith can also limit the ability for detection.	7+
Gas Filter Correlation Radiometer	Aerial, Satellite	Site	Single Channel (1D)	Satellite: 547.95 m3/day	Developing; theoretically within 1 ppm	Monitoring emissions from pipeline along ROW and remote/sparse arrangements of well sites. Screening technology for LDAR programs.	Requires clear skies for observations. Measurements require a high solar zenith angle.	4/7

Pellistor (Catalytic Bead)	Handheld, Fixed Location,	Component /Facility	Point Concentration (0D)	500 ppm - 5%	100%	LDAR programs (standalone or in combination with screening technologies)	Sensitive to high humidity, large temperature differentials, and environmental contaminants.	9
FTIR Spectroscopy	Vehicle, Aerial, Fixed Location	Facility	Single Channel (1D)	11.4 ppb	63-73%	Monitoring emissions from pipeline along ROW and remote/sparse arrangements of well sites. Screening technology for LDAR programs.	The survey time required for measurements is inversely proportional to the spectral resolution (distance travelled by the mirror in the interferometer).	9
Ultrasound Imaging	Handheld, Fixed Location	Component	Single Channel (1D)	8.5 g/hr	90%	LDAR programs (standalone or in combination with screening technologies)	Requires pressure drop to detect emissions.	4/7
MethaneSAT Spectrometry	Satellite	Site	Imaging (2D)	2 ppb over 1.5 km2	Satellite observations typically fall between <1-5% (not Methane SAT specific)	Monitoring emissions from pipeline along ROW and remote/sparse arrangements of well sites. Screening technology for LDAR programs.	Sensitive to low solar zenith and high wind speeds.	7+
Metal Oxide Semiconductor (MOS)	Handheld, Fixed Location	Facility /Site	Point Concentration (0D)	2-10 ppm	Within 0.36 ppm	Continuous monitoring of emissions on sites. LDAR Programs.	Sensitive to high humidity, large temperate differentials, and environmental contaminants. Exposure to large concentrations may de-sensitize the sensor irreversibly.	9

Mass-Flow Meter	Handheld, Fixed Location	Component	Point Concentration (0D)	1.4 standard liters per minute	Within 2%	LDAR programs (standalone or in combination with screening technologies)	No longer manufactured. Highly dependent on daily calibration procedures.	9
Laser Absorption Spectroscopy - Cavity Output	Fixed Location, Handheld UAVs, Vehicle	Facility	Point Concentration (0D)	30 ppb	87%	Monitoring emissions from pipeline along ROW and remote/sparse arrangements of well sites. Screening technology for LDAR programs.	Moderate interference from moisture - dried samples preferred for optimal analysis.	7+
Laser Absorption Spectroscopy - Closed Path (Multi)	Fixed Location, UAVs, Vehicle	Facility	Point Concentration (0D)	100 ppb	within 79 ppb	Monitoring emissions from pipeline along ROW and remote/sparse arrangements of well sites. Screening technology for LDAR programs.	Require specific environmental requirements for measurement.	7+
Mass Spectrometry	Handheld, Fixed Location	Component	Single Channel (1D)	1 ppb	Within 3.4%	Continuous monitoring of emissions on sites. LDAR Programs.	Requires controlled environment (i.e., vacuum system).	9
Gas Chromatography	Handheld, Fixed Location	Component	Single Channel (1D)	1 ppb	Within 3% to 6% of true conc.	Continuous monitoring of emissions on sites. LDAR Programs.	Calibration and purge required prior to use. Calibration frequency varies based on instrument.	9

Printed Nanotube Sensors	Fixed Location	Facility	Point Concentration (0D)	5 ppm	Developing - Currently focused on detection rather than actual quantificatio n	Continuous monitoring of emissions on sites. LDAR Programs.	Unknown	4/7
Laser Absorption Spectroscopy - Open Path	Fixed point, UAVs, Vehicle	Facility	Single Channel (1D)	2 ppm*m	90-97%	Monitoring emissions from pipeline along ROW and remote/sparse arragements of well sites. Screening technology for LDAR programs.	Measurement path length from 5 - 500 m. Wind limitations 2-10 m/s	7+
Etalon	Handheld, Vehicle, Fixed Location	Component	Single Channel (1D)	100 ppb	0.1 µm + 0.3 µm/m	Continuous monitoring of emissions on sites. LDAR Programs.	Highly dependent on surface reflectivity of the crystals; reflecting surfaces must be parallel and flat.	7+
Laser Absorption Spectroscopy - Closed Path (Single)	Fixed point, UAVs, Vehicle	Facility	Point Concentration (0D)	Relative to total pressure of the cell; 88 ppb	90-97%	Monitoring emissions from pipeline along ROW and remote/sparse arrangements of well sites. Screening technology for LDAR programs.	Require specific environmental requirements for measurement.	7+

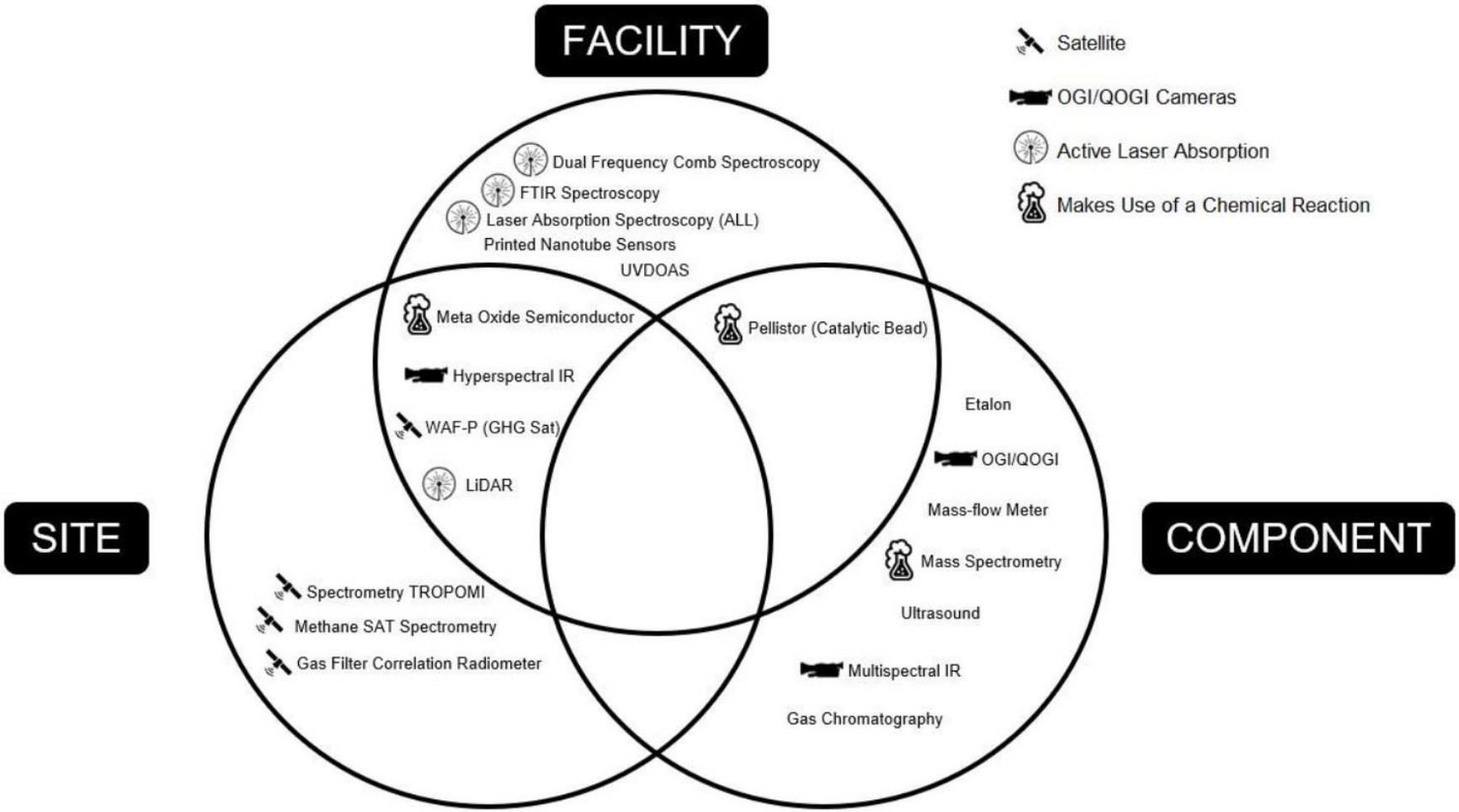
FACILITY
Satellite
OGI/QOGI Cameras
Active Laser Absorption
Makes Use of a Chemical Reaction
Dual Frequency Comb Spectroscopy
FTIR Spectroscopy
Laser Absorption Spectroscopy (ALL)
Printed Nanotube Sensors
UVDOAS
Meta Oxide Semiconductor
Pellistor (Catalytic Bead)
Hyperspectral IR
WAF-P (GHG Sat)
LiDAR
Etalon
OGI/QOGI
Mass-flow Meter
Mass Spectrometry
Ultrasound
Multispectral IR
Gas Chromatography
SITE
COMPONENT
Spectrometry TROPOMI
Methane SAT Spectrometry
Gas Filter Correlation Radiometer

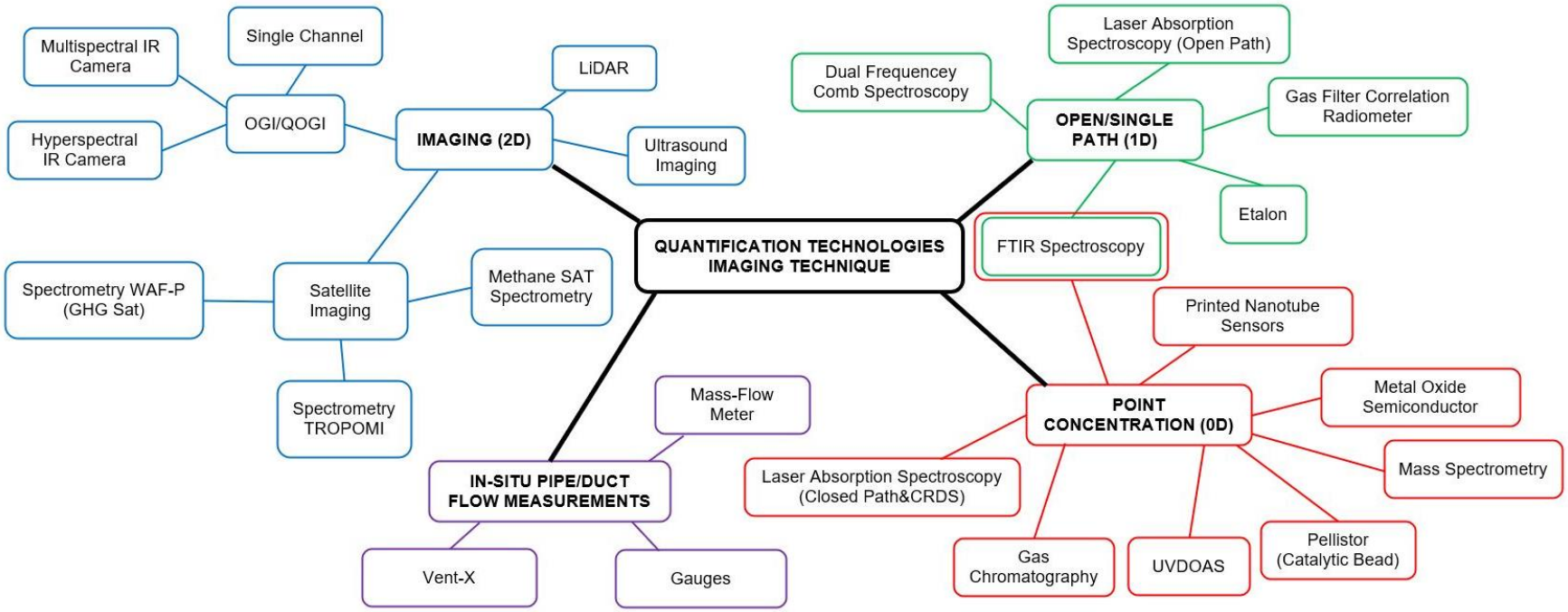
QUANTIFICATION TECHNOLOGIES IMAGING TECHNIQUE
IMAGING (2D)
Single Channel
Multispectral IR Camera
Hyperspectral IR Camera
OGI/QOGI
LiDAR
Ultrasound Imaging
Satellite Imaging
Spectrometry WAF-P (GHG Sat)
Methane SAT Spectrometry
Spectrometry TROPOMI
OPEN/SINGLE PATH (1D)
Laser Absorption Spectroscopy (Open Path)
Dual Frequencey Comb Spectroscopy
Gas Filter Correlation Radiometer
Etalon
FTIR Spectroscopy
POINT CONCENTRATION (0D)
Printed Nanotube Sensors
Metal Oxide Semiconductor
Mass Spectrometry
Laser Absorption Spectroscopy (Closed Path&CRDS)
Gas Chromatography
UVDOAS
Pellistor (Catalytic Bead)
IN-SITU PIPE/DUCT FLOW MEASUREMENTS
Mass-Flow Meter
Vent-X
Gauges

APPENDIX B: SUMMARY OF FIRST FIELD TRIAL KEY FINDINGS

Summary table of key statistics and findings from first field trial.

Technology	Average Error	Average Bias	Key Findings
Aerial NIR Hyperspectral	41%	-34%	- Reliability issues with cloud cover and turbulence - Windspeed error may cause significant systematic errors
Truck-based TDLAS (BLS)	57%	+19%	- Might be less susceptible to wind direction variability with BLS model. - Performed worse with lower emission rates - Performed worse with tanks than stacks
Truck-based TDLAS (IGM)	47%	-35%	- Systematically underestimated true rate; potentially due to coarse meteorological data and wind direction variability
AGAT Labs MWIR QOGI	67%	-46%	- Struggled with high flowrates causing underestimation; potentially due to limitations of hardware/software for estimating plume velocity at high flowrates
FLIR GF320 QOGI	55%	-26%	- Increased wind and flowrates caused underestimation due to GF320 framerate - Tank measurements less accurate than stack measurements; perhaps due to increased measurement distance

APPENDIX C: FLOW CONTROLLER DATA LOGGING EXAMPLE

Excerpt of flow controller data log from September 27th, 2023, between 11:21AM and 11:23AM.

Time (Local)	Flowrate (m^3/day)	Pressure (kPa)	Temperature (^oC)	Setpoint (m^3/day)	Volume Flow
2022-09-27T11:21:00.463	34.1	411.6	24.69	34	8.3
2022-09-27T11:21:01.501	34.1	411.7	24.7	34	8.3
2022-09-27T11:21:02.554	34.1	411.6	24.7	34	8.3
2022-09-27T11:21:03.592	34.2	411.6	24.71	34	8.3
2022-09-27T11:21:04.629	36.2	411.4	24.71	34	8.9
2022-09-27T11:21:05.667	35.4	411.3	24.72	34	8.8
2022-09-27T11:21:06.704	34.3	411.3	24.72	34	8.4
2022-09-27T11:21:07.742	34.1	411.4	24.73	34	8.4
2022-09-27T11:21:08.781	34	411.4	24.73	34	8.3
2022-09-27T11:21:09.833	34	411.5	24.73	34	8.3
2022-09-27T11:21:10.887	34	411.5	24.74	34	8.3
2022-09-27T11:21:11.940	34	411.6	24.75	34	8.3
2022-09-27T11:21:12.978	34	411.7	24.75	34	8.3
2022-09-27T11:21:14.031	34	411.7	24.75	34	8.3
2022-09-27T11:21:15.069	33.9	411.8	24.76	34	8.3
2022-09-27T11:21:16.138	33.9	411.9	24.76	34	8.3
2022-09-27T11:21:17.176	33.9	411.9	24.77	34	8.3
2022-09-27T11:21:18.245	33.9	412	24.77	34	8.3
2022-09-27T11:21:19.283	33.9	412.1	24.78	34	8.3
2022-09-27T11:21:20.352	33.9	412.1	24.78	34	8.3
2022-09-27T11:21:21.390	33.9	412.2	24.78	34	8.3
2022-09-27T11:21:22.460	33.9	412.3	24.79	34	8.3
2022-09-27T11:21:23.497	33.9	412.3	24.79	34	8.3
2022-09-27T11:21:24.551	33.9	412.4	24.8	34	8.3
2022-09-27T11:21:25.604	33.9	412.5	24.8	34	8.3
2022-09-27T11:21:26.690	33.9	412.5	24.8	34	8.3
2022-09-27T11:21:27.727	33.9	412.6	24.81	34	8.3
2022-09-27T11:21:28.765	44.9	411.9	24.81	51	11
2022-09-27T11:21:29.803	51.1	410.3	24.81	51	12.6
2022-09-27T11:21:30.913	51.7	409.9	24.81	51	12.8
2022-09-27T11:21:31.974	51.9	410.2	24.82	51	12.8
2022-09-27T11:21:33.011	51.9	410.5	24.82	51	12.8
2022-09-27T11:21:34.065	51.9	410.8	24.82	51	12.8
2022-09-27T11:21:35.118	51.9	411.1	24.83	51	12.8
2022-09-27T11:21:36.163	51.7	411.5	24.83	51	12.7
2022-09-27T11:21:37.241	51.9	411.8	24.83	51	12.7

2022-09-27T11:21:38.295	51.3	412.2	24.83	51	12.6
2022-09-27T11:21:39.332	51.1	412.6	24.83	51	12.5
2022-09-27T11:21:40.370	51	413	24.83	51	12.5
2022-09-27T11:21:41.455	51	413.5	24.83	51	12.5
2022-09-27T11:21:42.493	51	413.8	24.83	51	12.5
2022-09-27T11:21:43.578	50.8	414.2	24.82	51	12.5
2022-09-27T11:21:44.632	51	414.5	24.82	51	12.5
2022-09-27T11:21:45.718	51	414.8	24.82	51	12.5
2022-09-27T11:21:46.755	51	415.1	24.82	51	12.4
2022-09-27T11:21:47.840	50.8	415.4	24.82	51	12.4
2022-09-27T11:21:48.888	51	415.6	24.82	51	12.4
2022-09-27T11:21:49.963	51	415.8	24.82	51	12.4
2022-09-27T11:21:51.017	51	415.9	24.82	51	12.4
2022-09-27T11:21:52.087	51	416.1	24.82	51	12.4
2022-09-27T11:21:53.124	51	416.2	24.82	51	12.4
2022-09-27T11:21:54.177	51	416.4	24.82	51	12.4
2022-09-27T11:21:55.231	51	416.5	24.82	51	12.4
2022-09-27T11:21:56.269	51	416.6	24.82	51	12.4
2022-09-27T11:21:57.322	51	416.7	24.82	51	12.4
2022-09-27T11:21:58.360	51	416.7	24.82	51	12.4
2022-09-27T11:21:59.402	51	416.8	24.82	51	12.4
2022-09-27T11:22:00.458	50.8	416.9	24.82	51	12.4
2022-09-27T11:22:01.537	50.8	416.9	24.82	51	12.4
2022-09-27T11:22:02.590	51	417	24.82	51	12.4
2022-09-27T11:22:03.659	51	417	24.82	51	12.4
2022-09-27T11:22:04.697	51	417	24.82	51	12.4
2022-09-27T11:22:05.775	50.8	417	24.82	51	12.4
2022-09-27T11:22:06.804	50.8	417.1	24.82	51	12.4
2022-09-27T11:22:07.889	50.8	417.1	24.82	51	12.4
2022-09-27T11:22:08.927	51	417.1	24.82	51	12.4
2022-09-27T11:22:09.997	50.8	417.1	24.82	51	12.4
2022-09-27T11:22:11.034	50.8	417.1	24.82	51	12.4
2022-09-27T11:22:12.120	50.8	417.1	24.82	51	12.4
2022-09-27T11:22:13.173	50.8	417.1	24.83	51	12.4
2022-09-27T11:22:14.211	51	417.2	24.83	51	12.4
2022-09-27T11:22:15.248	51	417.2	24.83	51	12.4
2022-09-27T11:22:16.286	51	417.2	24.83	51	12.4
2022-09-27T11:22:17.324	51	417.2	24.83	51	12.4
2022-09-27T11:22:18.398	51	417.2	24.83	51	12.4
2022-09-27T11:22:19.431	51	417.2	24.83	51	12.4
2022-09-27T11:22:20.484	51	417.2	24.83	51	12.4

2022-09-27T11:22:21.549	50.8	417.2	24.83	51	12.4
2022-09-27T11:22:22.607	51	417.2	24.84	51	12.4
2022-09-27T11:22:23.645	51	417.1	24.84	51	12.4
2022-09-27T11:22:24.730	51	417.1	24.84	51	12.4
2022-09-27T11:22:25.768	51	417.1	24.84	51	12.4
2022-09-27T11:22:26.853	51	417.1	24.84	51	12.4
2022-09-27T11:22:27.907	50.8	417.1	24.85	51	12.4
2022-09-27T11:22:28.968	51	417.1	24.85	51	12.4
2022-09-27T11:22:30.014	50.8	417.1	24.85	51	12.4
2022-09-27T11:22:31.068	50.8	417.1	24.85	51	12.4
2022-09-27T11:22:32.129	51	417.1	24.85	51	12.4
2022-09-27T11:22:33.179	51	417.1	24.86	51	12.4
2022-09-27T11:22:34.229	51	417.1	24.86	51	12.4
2022-09-27T11:22:35.266	51	417.1	24.86	51	12.4
2022-09-27T11:22:36.335	51	417.1	24.86	51	12.4
2022-09-27T11:22:37.373	51	417	24.87	51	12.4
2022-09-27T11:22:38.411	51	417	24.87	51	12.4
2022-09-27T11:22:39.464	51	417	24.87	51	12.4
2022-09-27T11:22:40.502	51	417	24.87	51	12.4
2022-09-27T11:22:41.555	51	417	24.88	51	12.4
2022-09-27T11:22:42.609	51	417	24.88	51	12.4
2022-09-27T11:22:43.662	51	417	24.88	51	12.4
2022-09-27T11:22:44.700	51	416.9	24.89	51	12.4
2022-09-27T11:22:45.769	51	416.9	24.89	51	12.4
2022-09-27T11:22:46.814	51	416.9	24.89	51	12.4
2022-09-27T11:22:47.861	51	416.9	24.89	51	12.4
2022-09-27T11:22:48.898	51	416.9	24.9	51	12.4
2022-09-27T11:22:49.936	51	416.9	24.9	51	12.4
2022-09-27T11:22:50.974	51	416.8	24.9	51	12.4
2022-09-27T11:22:52.011	51	416.8	24.91	51	12.4
2022-09-27T11:22:53.048	51	416.8	24.91	51	12.4
2022-09-27T11:22:54.118	51	416.8	24.92	51	12.4
2022-09-27T11:22:55.155	51	416.7	24.92	51	12.4
2022-09-27T11:22:56.193	51	416.7	24.92	51	12.4
2022-09-27T11:22:57.231	51.1	416.7	24.92	51	12.4
2022-09-27T11:22:58.284	51.1	416.7	24.93	51	12.4
2022-09-27T11:22:59.338	51.1	416.7	24.93	51	12.4
2022-09-27T11:23:00.391	51	416.6	24.93	51	12.4

APPENDIX D: FIELD TRIAL NOTEBOOK

Release Type	Time Start	Release Rate (m^3/day)	Wind Speed (m/s)	Wind Direction	Pressure (kPa)	Temp (°C) from mass-flow controller
SEPTEMBER 25TH						
Large stack	10:00	0	1	SW	N/A	N/A
Large stack	10:20	340	1.5	S	207.9	21.29
Large stack	10:36	1200	1	SW	380.6	22.71
Large stack	10:51	1690	1.5	WSW	380.9	17.28
Large stack	11:07	710	1.5	W	410.2	12.52
Large stack	11:20	1350	1.5	W	389.2	19.66
Large stack	11:29	2720	1.5	W	317.7	16.6
Short stack 1.7m	11:38	2720	2.5	W	315.9	4.88
Short stack 1.7m	11:51	0	1	W	0	0
Short stack 1.7m	11:54	710	2.5	W	406.8	14.01
Short stack 1.7m	12:03	1200	2.5	WNW	387.6	21.14
Short stack 1.7m	12:20	340	2.5	NW	421	23.58
Short stack 1.7m	12:38	0	1	WSW	0	0
Short stack 1.7m	12:44	1690	1.5	W	290.5	30.18
Short stack 1.7m	13:08	1350	2.5	SW	356.4	19.26
Large stack	13:12	0	1.5	SW	N/A	N/A
Large stack	13:22	1350	1.5	SSW	338.3	28.6
Large stack	13:31	170	2.5	SW	421.5	28.52
Large stack	13:39	1200	3	SW	337.5	30.66
SEPTEMBER 26TH						
1.7m Stack	09:31	170	0	NA	307	21.41
1.7m Stack	10:02	51	0	NA	285	26.62
1.7m Stack	10:23	710	1	SW	282.4	25.81
1.7m Stack	10:52	8.5	0	NA	228	28.77

1.7m Stack	11:05	0	1	SW	0	0
1.7m Stack	11:21	51	1.5	E	243.8	30.2
1.7m Stack	11:31	710	1.5	SSE	227.5	32.18
1.7m Stack	11:42	8.5	1.5	E	377.2	30.53
1.7m Stack	11:53	51	1.6	SE	320.7	31.8
1.7m Stack	12:04	710	1.5	SE	262.7	32.98
1.7m Stack	12:12	8.5	2	SE	347	31.57
1.7m Stack	12:24	0	1.4	S	0	0
1.7m Stack	12:33	710	2	S	334.9	33.03
1.7m Stack	12:52	710	2	S	334.9	33.03
1.7m Stack	12:59	51	1.5	SE	427.6	33.9
1.7m Stack	13:18	8.5	2.5	S	409.7	34.72
Flare stack	13:39	1690	3.5	S	397.7	33.35
Flare stack	14:09	710	2.5	SW	435.4	25.31
Flare stack	14:23	1200	3.5	SW	423.6	31.28
Flare stack	14:37	1350	3	SW	413.7	30.15
Flare stack	14:50	340	3	SW	420.7	30.57
Small stack (3 piece - 4.84m)	15:06	0	3	SW	0	0
Small stack (3 piece - 4.84m)	15:10	170	3	SW	397.2	32.65
Small stack (3 piece - 4.84m)	15:31	1690	2	SSW	234.5	34.83
Small stack (3 piece - 4.84m)	15:42	710	2	S	407.8	29.4
Small stack (3 piece - 4.84m)	15:51	1200	2.5	S	380.9	30.99
Small stack (3 piece - 4.84m)	16:02	1350	1.4	S	377.8	30.37
Small stack (3 piece - 4.84m)	16:13	340	2	S	420.7	29.34
Small stack (3 piece - 4.84m)	16:24	0	2.6	SSW	445.6	31.92

Small stack (3 piece - 4.84m)	16:32	8.5	1.7	S	432.031.8	31.8
Small stack (3 piece - 4.84m)	16:40	85	2.5	S	412.5	32.31
Small stack (3 piece - 4.84m)	16:50	51	2	S	420.5	32.19
SEPTEMBER 27TH						
Green tank	09:28	170	2.5	SSE	446.2	12.65
	09:58	85	2.8	SSE	414.5	12.68
	10:09	0	2	SSE	428.8	14.5
	10:19	340	2.6	SSE	411.1	15.03
	10:31	8.5	2.4	SSE	425	15.91
	10:35	51	2.4	SSE	417	16.53
	10:48	34	2.2	SSE	417.5	17.18
Green tank reversed hose orientation	11:08	34	1.8		412	21.14
	11:21	51	1.9	S	410.1	24.83
	11:29	8.5	2.8	S	423.6	26.46
	11:38	340	2.1	S	410.4	27.77
	11:50	0	2.2	S	429.4	28.49
	11:58	85	3	S	414.2	29.95
	12:08	170	1.5	S	416	31.65
Short stack, 1.7 height	14:23	1690	1.5	SW	384.4	39.64
	14:36	34	2.5	SW	428	35.5
	14:44	710	2.5	W	423.5	37.7
	14:51	8.5	3	W	430.4	38.2
	14:58	0	3	W	0	0
	15:08	1200	2.5	W	413.5	39.59
	15:14	51	3	W	430	39.04
	15:20	170	1.4	W	421.3	38.89
	15:26	85	3	WSW	424.5	39.63

	15:32	340	1.2	W	427.7	39.52
	15:40	1350	1.5	WSW	402.4	40.03
	15:50	51	1.4	W	453.2	37.29
	15:59	8.5	1.5	W	442.9	39.05
	16:06	0	3.1	W	437.8	39.17
	16:13	710	3.2		420.6	38.26
	16:21	51	2.5	WSW	430.8	37.55
	16:29	8.5	3.1	W	431	38.08
	16:36	710	1.5	SW	421.3	38.05
	16:44	51	0	NA	429.5	38.25
	16:50	8.5	1.2	N	428	38.78
	17:00	710	1.7	W	424.4	38.25
SEPTEMBER 28TH						
1.7m stack	09:23	1350	1.7	S	338.6	16.92
	09:32	1200	0	NA	383.3	18.56
	09:47	1690	1.7	SSW	358.9	19.12
	09:57	1200	0	NA	386.3	16.03
	10:07	1690	1.2	SE	306.7	17.01
	10:15	1350	1.6	S	384.1	16.86
	10:29	1690	1.2	SW	393.2	22.93
	10:39	1350	0.6	SW	361.8	23.2
	10:47	1200	1.1	SE	381.6	23.21
Tall 3-piece stack	11:06	1200	1.4	SW	421.1	29.2
	11:23	340	1.8	S	438.1	27.44
	11:28	0	0.8	SE	538.7	29.19
	11:36	85	1	S	460.7	30.77
	11:45	170	1.7	SSW	447.9	32.76
	11:51	1690	1.5	SW	385.5	34.97
Medium 2-piece stack	13:17	1200	0.9	S	409.1	38.51
	13:36	340	2.4	SE	431.3	34.68

	13:43	0	2.7	SE	466.2	35.71
	13:51	85	1.5	SW	430.9	35.43
	13:58	170	2	SW	437.1	36.17
	14:05	1690	2.2	SW	384.5	37.12
Vent from shack, tape on pipe	15:24	85	N/A	N/A	437.1	31.5
	15:30	51	N/A	N/A	436.5	31.77
	15:36	170	N/A	N/A	436	32.1
	15:44	0	N/A	N/A	440.3	32.92
	15:50	340	N/A	N/A	429.9	32.92
	15:57	8.5	N/A	N/A	437	32.77
Vent from shack, tape off	16:06	340	N/A	N/A	429.3	32.77
	16:14	170	N/A	N/A	432.5	33.59
	16:20	51	N/A	N/A	432	33.4
	16:25	85	N/A	N/A	433.5	33.53
SEPTEMBER 30TH						
Tall Flare Stack	12:55	340	2.3	NNW	431.2	27.38
	13:28	710	5.2	NW	436.4	31.92
	13:43	1200	6.5	NW	422.3	29.1
	13:48	1690	3.8	NW	396.7	26.47
	13:54	2720	3.3	NW	449.7	20.57
	14:00	1200	1	NNW	421.5	16.9
	14:02	1690	1.8	NW	406.9	18.32
	14:04	0	N/A	N/A	N/A	N/A
1.7m Stack	14:09	170	3.1	NNW	434.6	25.49
	14:17	1690	1.9	NNW	422.1	23.48
	14:23	340	3	N	452.9	27.6
	14:30	8.5	3.4	NNW	493.6	28.17
	14:35	0	N/A	N/A	N/A	N/A
	14:41	1200	3.3	N	441.2	28.72
	14:47	85	2	NW	461.1	28.83

	15:04	51	5	N	464.2	29.69
Flare stack	15:36	170	2.5	NNW	465.6	28.94
	15:44	0	4.3	NNW	92.9	27.31
	15:47	8.5	4.1	NNW	469	28.59
	15:54	85	3.7	NNW	458.4	29.48
	16:00	51	4	NNW	462.4	30.33
Short stack	16:10	51	3.6	NNW	465.6	28.96
	16:16	710	2.9	NW	445.3	26.14
	16:23	2720	3.4	NNW	360.7	22.14
	17:15	1350	3	NNW	419.7	21.12
	17:19	340	2	NW	436	20.58
	17:23	2720	3	NW	350.9	19.42
	17:27	51	2.5	NNW	457.1	17.17
	17:32	710	3.4	NNW	438.9	17.11
	17:37	170	2.5	NNW	450.6	17.47
OCTOBER 1ST						
Flare stack	10:25:00	170	2.5	NE	439.1	24.98
Flare stack	10:35:40	8.5	2.5	NE	422	23.93
Flare stack	10:44:00	1200	2.5	NE	325.6	24.27
Flare stack	10:49:30	340	1.6	NE	391.1	23.3
Flare stack	10:55:40	51	2.2	NE	417.3	23.7
Flare stack	11:02:10	85	2.5	NE	406.5	24.17
Flare stack	11:08:35	0	1.8	NE	-	-
Flare stack	11:15:40	710	2.1	ENE	410.7	26.39
Flare stack	11:23:00	2720	2	ENE	314.6	25.24
Flare stack	11:30:10	1690	2.1	ENE	384.7	17.11
1.4m stack	11:39:40	1690	1.2	E	405.6	19.8
1.4m stack	11:46:20	2720	0.5	E	335.2	18.59
1.4m stack	11:52:30	710	0.1	ESE	414.5	18.07
1.4m stack	11:58:00	0	1.4	ENE	-	-

1.4m stack	12:03:50	85	0	N/A	427.6	22.9
1.4m stack	12:09:20	51	1	NE	421.5	26.61
1.4m stack	12:16:15	340	1	NE	427	30.13
1.4m stack	12:21:50	1200	2.4	NNE	408.2	31.21
1.4m stack	12:28:10	8.5	0	N/A	465.7	30.87
1.4m stack	12:33:30	170	2.1	ENE		31.86
Tank (with wind)	14:20	170	1.5	NE	434.5	34.23
Tank (with wind)	14:31:15	85	2.2	E	424	34.93
Tank (with wind)	14:40:00	0	2	ESE	-	-
Tank (with wind)	14:47:30	340	2.6	E	425.6	34.86
Tank (with wind)	14:55:40	8.5	1.9	ENE	429.6	34.84
Tank (with wind)	15:02:05	51	0.8	NE	432	34.57
Tank (with wind)	15:08:35	34	2.3	E	427.1	34.93
flare stack	16:04	170	2.6	E	439.6	26.32
flare stack	16:15:55	8.5	3.3	ESE	431.7	25.38
flare stack	16:23:30	1200	2.6	SE	405.6	23.44
flare stack	16:28:15	340	2.6	SE	430.3	23.25
flare stack	16:34:00	51	2.4	SE	427.7	23.2
1.4 m stack	16:39:40	0				
1.4 m stack	16:41:35	340	2.0	SE	431.6	22.94
1.4 m stack	16:47:35	2720	2.1	SE	305.2	22.01
1.4 m stack	16:53:20	85	1.6	SE	431.4	19.77
1.4 m stack	16:59:10	1200	1.9	SE	412.1	20.23

APPENDIX E: SUPPLEMENTAL INFORMATION